ANELASTIC RELAXATION AND PHASE TRANSFORMATIONS IN DOPED BINARY OXIDES

A Dissertation

by

PEIPEI GAO

Submitted to the Office of Graduate and Professional Studies of
Texas A&M University
in partial fulfillment of the requirements for the degree of

DOCTOR OF PHILOSOPHY

Chair of Committee,	Miladin Radovic
Committee Members,	Cagin Tahir
	Raymundo Arroyave
	Haiyan Wang
Head of Department,	Andreas A. Polycarpou

August 2016

Major Subject: Mechanical Engineering

ABSTRACT

Doped binary oxides (DBOs) with fluorite structures, such as doped ceria (CeO_2) or zirconia (ZrO_2), are widely used in different electrochemical devices such as solid oxide fuel cells, oxygen sensors, and gas separation membranes due to their high ionic conductivity. Mechanical and electrochemical properties of DBOs and their eventual coupling are of crucial importance for their use in different electrochemical devices commonly operating under harsh environments including high temperature, mechanical stress, electrical field, and reducing/oxidizing environments, etc. In this study, we report on the temperature-dependent mechanical and electro-mechanical properties of common electrolyte materials such as yttria stabilized zirconia (YSZ), scandia-ceria stabilized zirconia (SCSZ), and gadolinia doped ceria (GDC).

The mechanical properties were studied using resonant ultrasound spectroscopy (RUS), dynamic mechanical analysis (DMA) and cyclic compression testing (CCT). In addition, in-situ neutron diffraction at elevated temperatures was used to study structural changes under applied mechanical loads in the case of YSZ. It was found that the elastic moduli change with temperature in a non-linear manner, where the large decrease in elastic moduli with temperature and large mechanical loss (or mechanical damping) occur in different temperature ranges (~ 100 – 500 °C) for stabilized zirconia ceramics with different dopants and compositions. In addition, a slight deviation from the linear change of elastic moduli with temperature and a much smaller mechanical damping was observed in the temperature range of 100 – 300 °C for doped ceria ceramics, when

compared to stabilized zirconias. Furthermore, stress-strain hysteresis loops (pseudoelastic behavior) were observed in YSZ and SCSZ under sinusoidal compressive loading at different temperatures. It is shown in this study that the non-linear changes of elastic modulus with temperature and stress-strain hysteresis can be attributed to the following mechanisms: (i) stress-induced reorientation of oxygen vacancy complexes in all materials and (ii) reversible phase transformations in SCSZ.

In addition, electro-mechanical coupling in stabilized zirconias with centrosymmetric cubic (fluorite) structure was studied. It was found for the first time that both YSZ and SCSZ undergo spontaneous polarization under sinusoidal stress, suggesting their piezoelectric behavior. Stress-induced polarization was observed in YSZ in the 210 – 570 °C temperature range while in SCSZ it occurs between 200 °C and 300 °C. These results suggest that the reorientation of oxygen vacancy complexes may be the reason for electro-mechanical coupling. Although the magnitude of polarization in 8YSZ was found to be smaller than that in traditional piezoelectric materials such as PZT, it is still significant especially because it was measured at temperatures significantly higher than Curie temperature in common piezoelectric materials such as PZT.

DEDICATION

To my parents, little sister and all my loving family.

ACKNOWLEDGEMENTS

I would like to express my deepest gratitude and respect to my advisor, Dr. Miladin Radovic, who constantly and convincingly conveyed a great enthusiasm in my research over the last four years. I was greatly impressed by his ideas and consistent hard work. Without his guidance and persistent help this dissertation would not have been possible.

My great appreciation also goes to my committee members Dr. Cagin Tahir, Dr. Raymundo Arroyave and Dr. Haiyan Wang for serving in my committee and for their helpful suggestions.

I truly appreciate all help from collaborators from other research institutes. I want to thank Dr. Goran Brankovic and Dr. Zorica Brankovic, University of Belgrade, for their guidance during electro-mechanical testing. Thanks go to Dr. Nina Orlovskaya and Dr. Zhilin Xie, University of Central Florida, for their help preparing samples. I express my sincere gratitude to Dr. An Ke, Dr. Dunji Yu, Dr. Andrew Payzant and Dr. Yan Chen, Oak Ridge National Laboratory, for their help with carrying out in-situ neutron diffraction experiments and their guidance during data analysis process. I'd like to acknowledgement Dr. Edgar Lara-Curzio, Rosa Trejo and Christine Goudy, Oak Ridge National Laboratory, for helping me with DMA, TMA and high temperature XRD testing.

My special thanks go to Amy Bolon who joined me in this project at the end of 2012. Ever since then, we have worked together, discussed our research results and hung

out together at baseball games. I appreciate her company and excellent contributions to this project.

I would like to thank all my friends and colleagues in the research group, Junwei Xing, Liangfa Hu, Rogelio Benitez, Huili Gao, Matthew Westwick, Yexiao Chen, Dr. Maricela Lizcano, who made my stay and studies more enjoyable. Additionally, I want to thank Berna Akgenc for her collaboration and excellent computational simulations that are based on the results of my thesis research. My gratitude also goes to faculty and staff in the Materials Science and Engineering Department and the Mechanical Engineering Department for making my study and life at Texas A&M University a great experience.

I want to extend my appreciation to the U.S. National Science Foundation (CAREER Award: DMR-1057155), which provided the funding throughout my Ph.D. research.

Last but not least, many thanks to my family for their encouragement, trust, understanding and patience with all my work these years. Their solid support made me always strong to pursue new challenges and face all difficulties with a smile.

NOMENCLATURE

3Y-PSZ	3 mol% Yttria Partial Stabilized Zirconia
8YSZ	8 mol% Yttria Stabilized Zirconia
10GDC	$Gd_{0.1}Ce_{0.9}O_{0.95}$
10YSZ	10 mol% Yttria Stabilized Zirconia
20GDC	$Gd_{0.2}Ce_{0.8}O_{0.90}$
A	Area
Al_2O_3	Aluminum Oxide
BTO	Barium Titanate ($BaTiO_3$)
CeO_2	Cerium Oxide (Ceria)
DMA	Dynamic Mechanical Analysis
DBO	Doped Binary Oxides
CCT	Cyclic Compression Test
E	Elastic Modulus
E'	Storage Modulus
E''	Loss Modulus
E^{RT}	Elastic Modulus at Room Temperature
f	Frequency
FWHM	Full Width at Half Maximum
G	Shear Modulus
Gd_2O_3	Gadolinium Oxide (Gadolinia)

GDC	Gadolinia Doped Ceria
H_c	Conductivity Enthalpy
H_a	Association Enthalpy
H_m	Migration Enthalpy
HT-XRD	High temperature X-ray diffraction
MTS	Materials Test System
OM	Optical Microscopy
P	Polarization
PSZ	Partially Stabilized Zirconia
PZT	Lead Zirconate Titanate ($Pb(Zr_xTi_{1-x})O_3$)
Q	Charge
Q^{-1}	Mechanical Damping (Loss Modulus Coefficient), E''/E'
RUS	Resonant Ultrasound Spectroscopy
Sc_2O_3	Scandium Oxide (Scandia)
SCSZ	10 mol% Scandia, 1 mol% Ceria Stabilized Zirconia
SSZ	10 mol% Scandia Stabilized Zirconia
SEM	Scanning Electron Microscopy
tanδ	Mechanical Damping (Loss Modulus Coefficient), E''/E'
T_c	Currie Temperature
TMA	Thermal Mechanical Analysis
W_d	Energy Dissipation per Unit Volume per Load-unload Cycle
XRD	X-ray Diffraction

Y_2O_3	Yttrium Oxide (Yttria)
Y-PSZ	Yttria Partially Stabilized Zirconia
YSZ	Yttria Stabilized Zirconia
ZrO_2	Zirconium Oxide (Zirconia)
Δ	Relaxation Strength
ΔStress	Stress Amplitude
ΔV	Voltage Amplitude
ε	Strain
σ	Stress
η	Loss Modulus Coefficient (Mechanical Damping), E'/E''
τ	Relaxation Time

TABLE OF CONTENTS

Page

LIST OF FIGURES

Page

LIST OF TABLES

Page

1. INTRODUCTION

1.1 Background

1.1.1 Fluorite Doped Binary Oxides

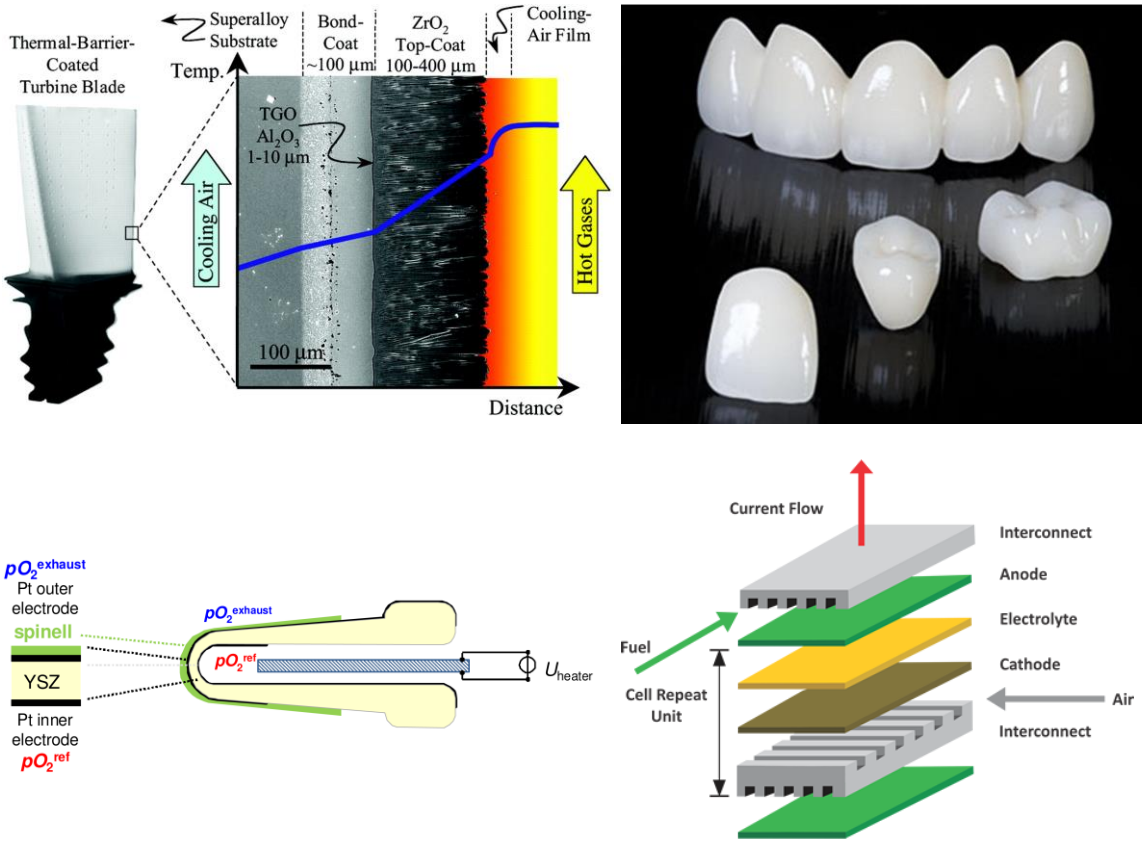

Figure 1.1. Common applications of zirconia and zirconia-based ceramics (a) the thermal barrier coating for gas-turbine engine [1], (b) dental crown [2], (c) oxygen sensor [3] and (d) solid oxide fuel cell (SOFC) [4].

In the last decades, doped binary oxides (DBOs) have been one of the most important ceramic materials for different applications such as zirconia-based ceramics. Zirconia (ZrO_2) and zirconia-based ceramics show high strength, toughness, hardness,

high melting point, low thermal conductivity and large thermal shock resistance. Therefore, they are used in a number of the applications such as the thermal barrier coatings of gas turbines (Figure 1.1a), ceramic blades, dental crowns (Figure 1.1b), cutting tools, etc. [5-7]. Pure zirconia has monoclinic crystal structure below 1170 °C, cubic structure above 2680 °C and tetragonal structure in between [8]. A volume contraction (around 5 %) occurs during phase transformation from monoclinic and tetragonal, usually leading to the mechanical failure during heating [9]. One of the most effective methods to avoid this problem is to partially or fully stabilize tetragonal or cubic structure from high temperature to room temperature by doping with cubic oxides such as CaO, Y_2O_3, MgO and CeO_2 [10-12]. If the concentration of dopants is not enough to completely stabilize cubic at room temperature, partially stabilized zirconias (PSZs) are formed [13]. PSZs commonly contain a mixture of two or more phases such as cubic, tetragonal and monoclinic.

Although PSZs are used in structural applications because of their good fracture toughness, fully stabilized fluorite (cubic) zirconias are mostly used in electrochemical devices due to their high ionic conductivities [14, 15]. Doping with some aliovalent oxides not only stabilizes the cubic structure, but also introduces oxygen vacancies to maintain the charge neutrality. The directional migrations of those oxygen vacancies at high temperatures under an applied electrical field leads to good ionic conductivity in stabilized zirconias [16-18]. Therefore, stabilized zirconias are used as electrolytes in oxygen sensors (Figure 1.1c), gas separation membranes and SOFCs (Figure 1.1d).

1.1.2 Application of Doped Zirconia and Ceria Ceramics as Electrolyte Materials in Solid Oxide Fuel Cells

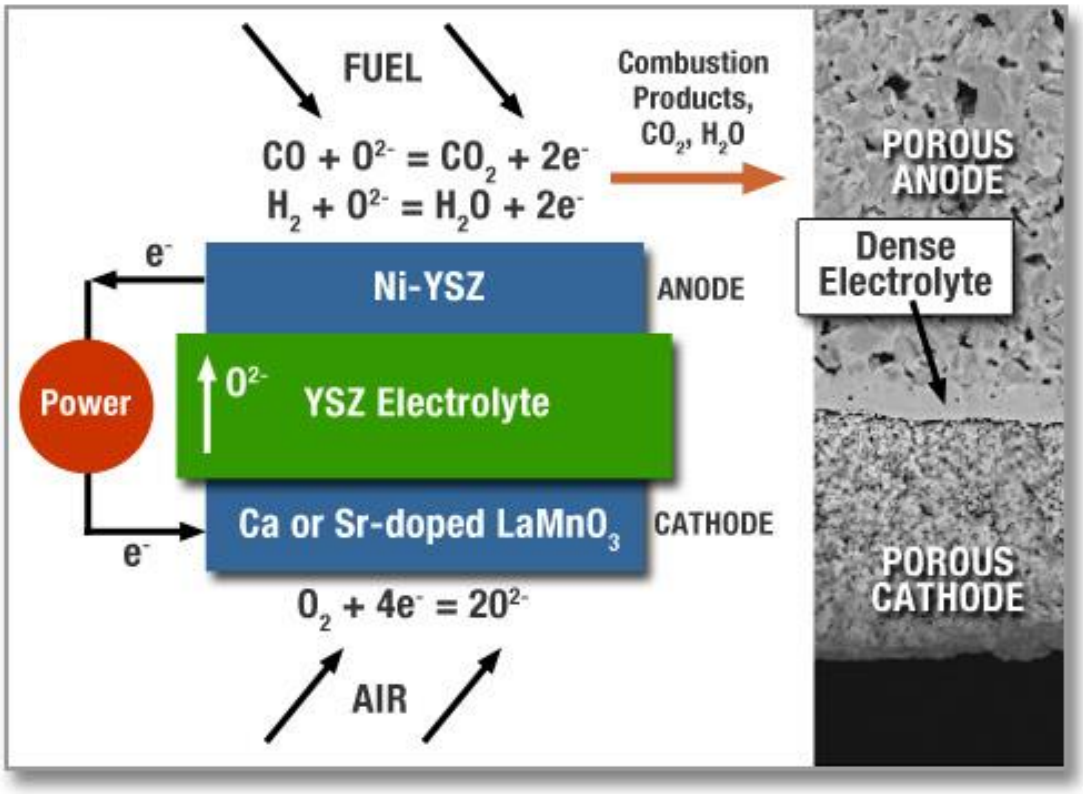

Figure 1.2. The principle of solid oxide fuel cell (SOFC) operation [19].

SOFCs, as highly efficient electrochemical energy conversion devices, are an essential component of the future clean energy economy. The advantages of SOFCs over other energy conversion devices include high efficiency, multi-fuel capability, modularity, and the low emission of pollutants. SOFCs are ceramic fuel cells in which an oxide ion conducting solid electrolyte is sandwiched between the anode and cathode

[20, 21]. The schematic of SOFC is shown in Figure 1.2. Solid electrolytes are usually made from the fast ionic conductors, FICs, where the main requirement for an electrolyte material is very high ionic conductivity and low electronic conductivity. Oxides with fluorite structure (zirconia based or ceria based) are the classical and most widely used FICs nowadays. Doping with aliovalent oxides in the ZrO_2 or CeO_2 host lattice induces a large number of vacancies on the oxygen sublattice [22], that in turn results in high ionic conductivity.

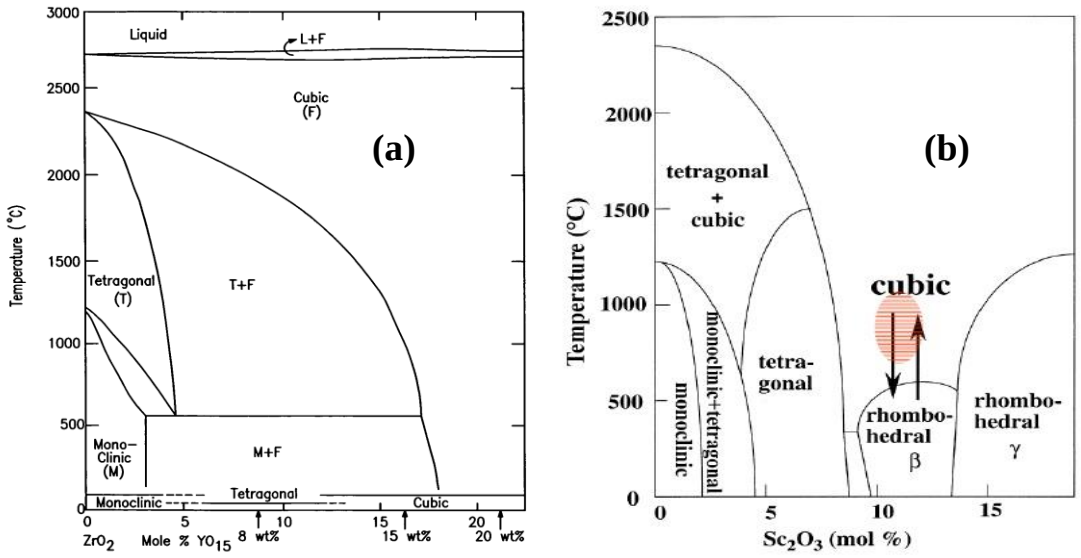

Figure 1.3. (a) Phase diagram of $YO_{1.5}$ doped ZrO_2 (b) phase diagram of Sc_2O_3 doped ZrO_2.

Considering conductivity, reliability and cost, yttria stabilized zirconia (YSZ) and scandia, stabilized zirconia (SSZ) are two kinds of stabilized zirconias that have been widely studied and commercialized in recent years [15, 23]. When the ZrO_2 is

doped with a certain concentration of yttira (Y_2O_3: YSZ) or scandia (Sc_2O_3: SSZ) the tetragonal, rhombohedral or cubic phase is stabilized depending on the dopant concentration shown in the phase diagrams (Figure 1.3a [24] and Figure 1.3b [25]).

In partially stabilized zirconia (Y-PSZ) with low Y_2O_3 concentration (3 mol% $<Y_2O_3<$ 8 mol%), the structure is mainly tetragonal. 3 mol% Y_2O_3 partially stabilized zirconia (3Y-PSZ) is a typical representative of Y-PSZs in which significant improvements of fracture toughness are achieved due to stress induced martensitic-like transformation of the tetragonal metastable phase into a monoclinic state at the crack tip [26]. This material is used in applications where high toughness and crack resistance is of prime interest, such as thermal barrier coatings in gas turbines or dental crowns. With higher dopant concentrations (Y_2O_3>8 mol%), YSZ forms a metastable cubic structure at room temperature [27]. Above around 600 °C, the concentration of free oxygen vacancies and ionic conductivity reach a maximum value with 8 – 10 mol% Y_2O_3 (0.1 S/cm at 1000 °C and 0.03 S/cm at 800 °C) [16, 28].

Similar to YSZ, SSZ reaches a maximum conductivity and fluorite structure above 600 °C when doped with 10 – 12 mol% Sc_2O_3 (SSZ). However, SSZ shows cubic to rhombohedral phase transformation accompanied by marked decrease in ionic conductivity during cooling below 600 °C [29-32]. In addition, the long term operation of SSZ in the 700 – 1000 °C temperature range results in the formation of a tetragonal phase [33]. In order to further stabilize the cubic structure of SSZ at room temperature and minimize the possibility of an undesirable phase transition from cubic to rhombohedral or tetragonal, the addition of small amount of CeO_2 [31], Al_2O_3 [34, 35],

Gd_2O_3 [32], or that of Bi_2O_3 [36] have been suggested. In a study by Wang et al. [37], an addition of 1 – 10 mol% CeO_2 to 10 mol% Sc_2O_3 stabilized zirconia (SCSZ) has been shown to fully stabilize cubic structure at room temperature. However, it has been reported that 1 mol% CeO_2, 10 mol% Sc_2O_3 stabilized ZrO_2 (SCSZ) exhibited higher electrical conductivity (0.084 S/cm at 800 °C) than its counterparts having higher amounts of CeO_2 dopant [38].

Unlike stabilized zirconias, phase stability is not a concern in doped cerias since pure ceria has a stable cubic structure even at room temperature. However, pure ceria shows relatively low ionic conductivity. Considerable increase in ionic conductivity of ceria has been reported as a result of doping with lower valent oxides such as Yb_2O_3, Y_2O_3, Dy_2O_3, Gd_2O_3, Sm_2O_3, Nd_2O_3 or La_2O_3 [39, 40]. Gd doped ceria (GDC) show relatively high ionic conductivity and high stability, usually with 10 – 20 mol% $GdO_{1.5}$ dopant concentrations.

The biggest problem facing doped ceria ceramics for their application as electrolyte material in SOFCs is that the anode side comes in direct contact with the lower oxygen partial pressure atmosphere in which Ce^{4+} reduces to Ce^{3+}. This reduction leads to increased electronic conduction in GDC electrolyte and, therefore, lower cell potential and lower efficiency. The reduction not only causes electrochemical degradation, but also results in significant chemical expansion [39], generation of chemical stresses and eventually mechanical cracking. Thus, ceria based electrolytes are mostly used in the 600 – 800 °C temperature range and/or with a thin coated layer of YSZ at the anode side to protect it from the extended reduction [41, 42].

1.1.3 Defect Complexes

The doping of aliovalent oxides results in the formation of oxygen vacancies, to balance the charge difference between the doped cation (R^{3+}) and host cation (M^{4+}), as shown in Equation 1 using Kroger-Vink nomenclature [17, 43-45].

$$R_2O_3 \xrightarrow{MO_2} 2R'_M + V_O^{\bullet\bullet} + 3O_O^x \quad \text{(1.1)}$$

Oxygen vacancies most freely move in dilute solutions at high temperatures (above 600 °C) leading to a high ionic conductivity. However, at low temperatures (below 600 °C), oxygen vacancies become trapped by immobile opposite charged cations even in dilute solutions partially due to the strong Columbic attraction between them, but mainly because this clustering minimizes the lattice strain energy [15]. One simple type of complexes is formed between oxygen vacancy and dopant cation, i.e. $(R'_M V_O^{\bullet\bullet})^{\bullet}$ [10, 46-49]. Another simple type of complexes was found in a number of studies in 8YSZ [50-54] using EXAFS to study the local structure of oxygen vacancies as vacancies preferentially around Zr^{4+}, namely $(Zr_{Zr}^x V_O^{\bullet\bullet})^{\bullet\bullet}$.

When increasing the concentration of dopants, more complex dipoles, e.g. $(2R'_M V_O^{\cdot\cdot})^x$, may appear in the lattice [10, 55]. Meanwhile, with higher dopant concentrations or longer aging time, oxygen vacancies tend to form aggregated clusters (or local-domains), such as $Zr_3Y_4O_{12}$ (rhombohedral structure with space group $R\bar{3}$) [56], fluorite-derivative structure (delta phase) [57] and other similar structures (pyrochlore, bixbyite, zirconolite) [57]. With increasing the concentration of dopants and aging time, the number and size of aggregates increase [48, 58]. This process is energetically favorable as it minimizes strain energy caused by the difference between

ionic radius of dopant (R^{3+}) and host (M^{4+}) ions, usually referred to as the local ordering of oxygen vacancy clusters in the literature [57, 58]. Kondoh et al. [58, 59] indicated that the short range ordering of oxygen vacancies lead to a decrease of ionic conductivity in YSZ with a higher dopant concentration (> 8 mol%) or longer service time.

1.1.4 Anelastic Relaxation and Dielectric Relaxation

It has been proposed [10, 57, 60, 61] that the defect complexes in doped binary oxides could orient with both applied stress and electric field. Wachtman's eight-position model [62] in Figure 1.4a shows that oxygen vacancies have the same possibility to occupy the eight equivalent first-neighbor positions (labeled as '1's in Figure 1.4a) around either a dopant cation (used as an example in Figure 1.4) or host cation. However, the eight positions could be biased if applying an electrical or stress field, as those complexes form elastic and electrical dipoles. Nowick et al. [60, 63] was the first who proposed that the anelastic relaxation or dielectric relaxation of the simple elasto-electric dipoles, $(R'_M V_O^{\bullet\bullet})^{\bullet}$ can take place under electric filed or applied stress, dissipating energy during application of cyclic loading or electric field. If we look at (110) plane and the $(R'_M V_O^{\bullet\bullet})^{\bullet}$ dipole as an example (Figure 1.4b), the dopant-vacancy association with partial separation of charges (electric dipole) can reorient under the electrical field in a [111] direction by the thermally activated hopping of the vacancy around the dopant cation as illustrated in Figure 1.4c. This reorientation process results in dielectric relaxation at temperatures below 600 °C [64-67]. Similarly, when stress is applied, for example in a [111] direction on a (110) plane as it is illustrated in Figure

1.4d, the oxygen vacancy can also jump to the preferential positions to minimize the lattice strain energy. The latter is commonly referred as anelastic relaxation. As it is discussed in previous studies [10, 55, 58, 68, 69], this process results in frequency dependent, thermally activated anelastic relaxation peaks in mechanical loss spectra.

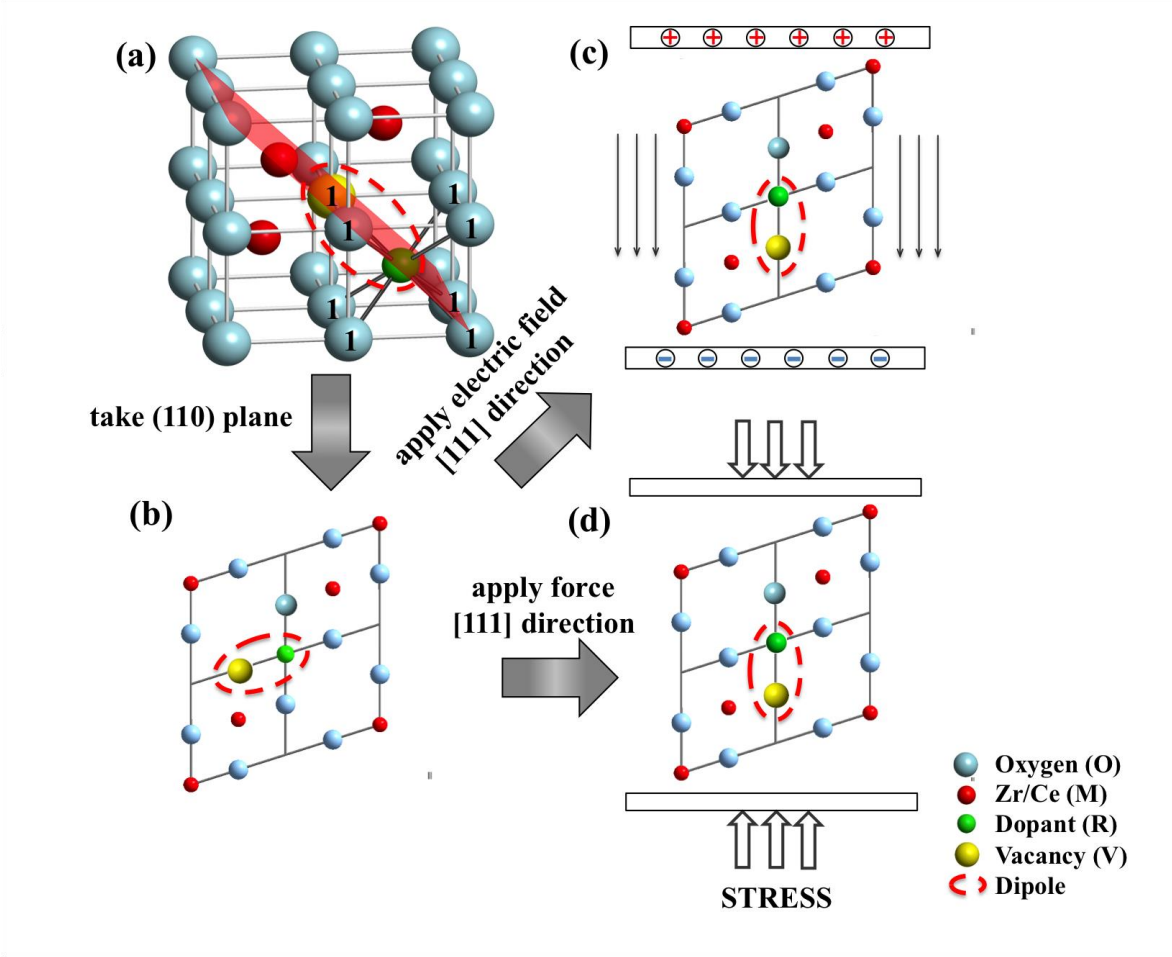

Figure 1.4. (a) Schematic of fluorite structure of MO_2 (ZrO_2/CeO_2) with dopant (R_2O_3) and eight equivalent nearest neighbor positions (labeled as '1's) around dopant ion for hopping of oxygen vacancy (b) (110) plane from fluorite structure (c) dielectric relaxation of electric dipole $(R'_M V_O^{\bullet\bullet})^{\bullet}$ on the (110) plane under the [111] direction electric field; (d) anelastic relaxation of elastic dipole $(R'_M V_O^{\bullet\bullet})^{\bullet}$ on the (110) plane under the [111] direction compressive force.

Several different experimental techniques were used to study anelastic relaxation in YSZ. Weller et al. [10] first studied anelastic relaxation of cubic YSZ using inverted torsion pendulum in the low frequency range and flexural oscillation in the high frequency range. Two relaxation peaks were observed for both single crystal and polycrystalline YSZ samples. Two damping peaks in single crystal 3 mol% – 24 mol% YSZ were attributed to the anelastic relaxation of two types of elastic dipoles, namely $(Y'_{Zr}V_O^{\bullet\bullet})^{\bullet}$ and $(2Y'_{Zr}V_O^{\bullet\bullet})^{x}$ [10, 70], similar to what was previously observed in Y_2O_3 doped CeO_2 by Nowick and coworkers using flexural resonant vibration method [71]. For 10 mol% YSZ, activation energies of 1.3 eV for the first relaxation peak and approximately 2 eV for the second peak were determined from the mechanical spectroscopy results [70]. In polycrystalline 8YSZ samples, Weller et al. [68] found that the activation energy of 1.4 ± 0.2 eV for the first relaxation peak is close to that observed in single crystals, and concluded that this relaxation is also caused by reorientation of $(Y'_{Zr}V_O^{\bullet\bullet})^{\bullet}$ dipoles. However, activation energy of 2.7 ± 0.2 eV for the second relaxation peak in polycrystalline samples was higher than that determined for single crystals samples, and therefore Weller et al. [68] suggested that this relaxation peak may be the result of local ordering of oxygen vacancies. Kondoh et al. [58, 72] used inverted torsion pendulum method to compare anelastic relaxation in 8YSZ after 1000 hours aging to that of as processed 10YSZ and 8YSZ. They showed that the intensity of the mechanical damping (loss) associated with the second relaxation peak is much lower in both 10YSZ

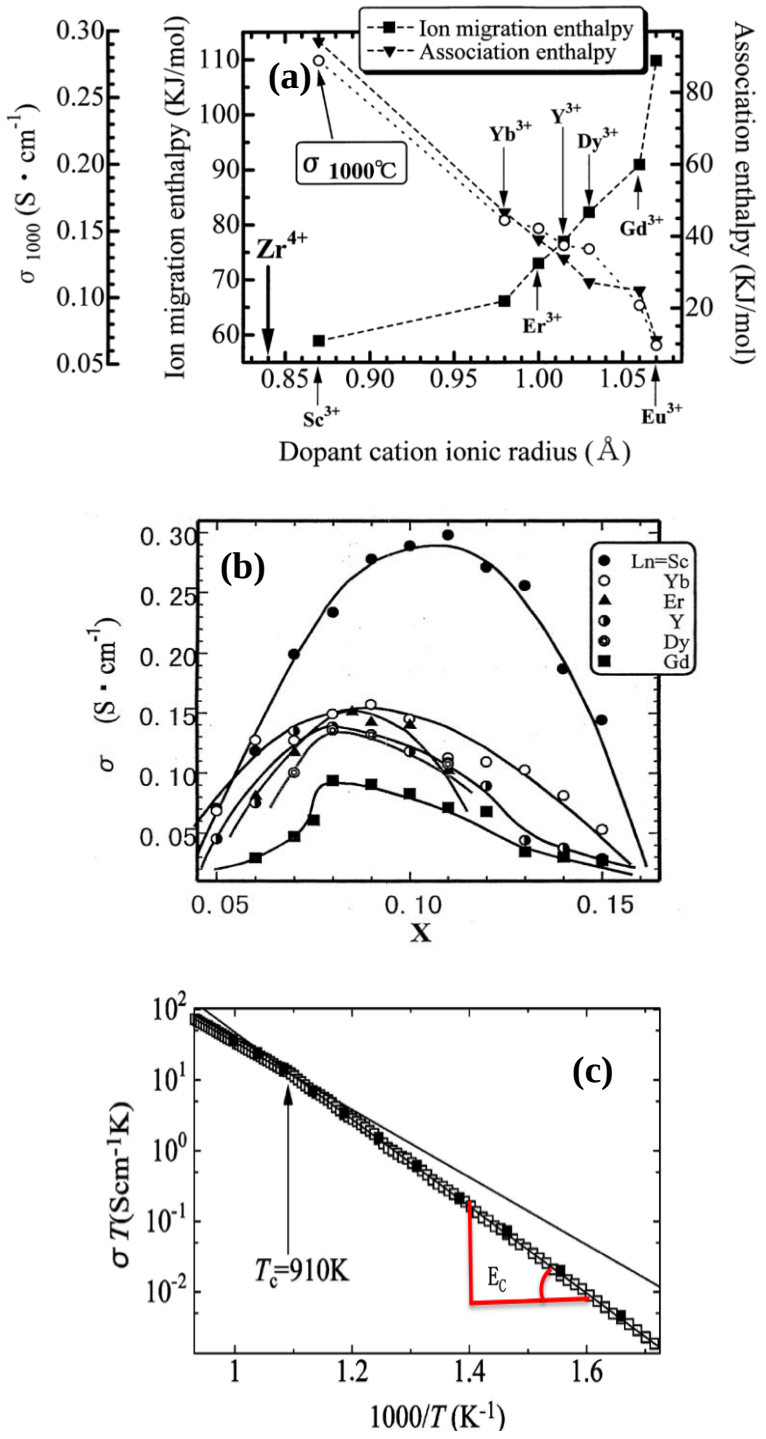

Figure 1.5. (a) Ionic conductivity, ion migration enthalpy and association enthalpy versus dopant ion radius curves [16] (b) Composition dependence of the electrical conductivity at 1000 °C for $(ZrO_2)_{1-x}(Ln_2O_3)_x$ [16] (c) the Arrhenius plots of DC conductivity (null) and AC conductivity (solid) in 8 mol% YSZ [17].

and aged 8YSZ when compared to the as-processed 8YSZ and also concluded that local ordering of oxygen vacancies contributes to the second mechanical damping peak in polycrystalline samples. Kushi et al. [55] studied the changes of anelastic relaxation with increasing temperature using internal friction meters (JE, JG, EG-HT or EGII-HT, Nihon Technoplus Co. Ltd). They also detected two anelastic relaxation peaks and attributed them to the relaxation of oxygen vacancies [67, 73].

To our best knowledge, only two studies reported on anelastic relaxation in scandia doped zirconias. Weller et al. [74] tested ZrO_2 doped with 10 mol% Sc_2O_3 (SSZ) at 2.1 Hz and 9.8 Hz and concluded that an internal friction peak around 227 °C can be attributed to anelastic relaxation of dipoles, while the other one at 477 °C was caused by phase transition from rhombohedral to cubic. Kushi et al. [55] indicated that both internal friction peaks in SCSZ were most likely due to phase transformations.

1.1.5 Electrical Properties of Doped Binary Oxides

As indicated previously, the directional migration of free oxygen vacancies leads to high ionic conductivity in DBOs at high temperatures (above around 600 °C). At low temperatures, oxygen vacancies are trapped by immobile oppositely charged cations leading to low ionic conductivity, so the operating temperatures for SOFCs are high. To maximize the ionic conductivity, DBOs are mainly engineered by optimizing the type and concentration of dopants [75]. Arachi et al. [16] have systematically studied the influence of difference aliovalent dopants including Sc_2O_3, Yb_2O_3, Er_2O_3, Y_2O_3, Dy_2O_3 and Gd_2O_3 on the transport properties of stabilized zirconias (Figure 1.5a). The total

activation enthalpy for ionic conductivity in Figure 1.5c, H_c, depends strongly on the radius of dopant since, at lower temperature $H_c=H_a+H_m$, where H_a is the vacancy-cation association enthalpy and H_m is the migration enthalpy for oxygen vacancies shown in Figure 1.5a. At higher temperatures (600 – 1000 °C), the association enthalpy reduces to almost zero. In addition, migration enthalpy increases as the difference between the ionic radii of dopant and host ion increase. This finding was crucial for the development of zirconia based solid-state ionics with high ionic conductivities. Among the dopants that can fully stabilize the cubic structure in zirconia, the highest ionic conductivity is achieved when the radius of doped cation (Sc^{3+}: 87 pm; Yb^{3+}: 98 pm; Er^{3+}: 100 pm; Y^{3+}: 101.9 pm; Dy^{3+}: 103 pm; Gd^{3+}: 114.3 pm) is closest to the ionic radius of host cation (Zr^{4+}: 84 pm). Therefore, Y_2O_3 doped ZrO_2 (YSZ) and Sc_2O_3 doped ZrO_2 (SSZ) are most common zirconia-based electrolyte materials for SOFCs considering their relatively high ionic conductivities, stabilities, etc.

The concentration of dopants also influences the ionic conductivities of DBOs. With the increasing concentration of dopant, the ionic conductivities of doped zirconias are governed by two competing factors: (a) the increasing concentration of charge carriers (e.g. oxygen vacancies) leading to higher conductivity; and (b) the formation of local complexes that trap free oxygen vacancies leading to the decrease in mobility of oxygen vacancies, and thus decrease in the ionic conductivity of doped zirconias with increasing dopant concentration [16]. In YSZ and SSZ, maximum ionic conductivities were obtained by the dopant concentrations of 8 mol% Y_2O_3 [76] and 10 – 12 mol% Sc_2O_3 [31, 76] shown in Figure 1.5b, respectively.

Similarly, as in doped zirconias, the ionic conductivity of cerias depends on the type and concentration of dopant and a decreasing trend in conductivity is observed after reaching a certain amount of dopant concentration. Among the different dopants that have been studied so far, the ionic radii of Sm^{3+} and Gd^{3+} are the closest to that of Ce^{4+} [77, 78]. Therefore, Sm_2O_3 and Gd_2O_3 doped ceria show the highest ionic conductivity, usually with a concentration of 10 – 20 mol% $RO_{1.5}$ (R: Sm/Gd) [79]. Moreover, in a study by Yahiro et al [80], ionic conductivity was examined as a function of varied oxygen partial pressure for a series of rare earth doped ceria, and those doped with Sm_2O_3 and Gd_2O_3 doped ceria were found to be "the least reducible systems". However, the application of Sm_2O_3 doped ceria (SDC) as an electrolyte material is limited to temperatures below 600 °C because its efficiency as ionic conductor is reduced due to high electronic leakage above that temperatures [40]. Nevertheless, the highest ionic conductivity is attributed to Gd_2O_3, which is the best-known dopant for ceria based electrolyte material for intermediate temperature solid oxide fuel cells [81, 82].

1.1.6 Thermal and Mechanical Properties of Doped Binary Oxides

The reliability of SOFC stack is a complex function of the electrochemical, mechanical, thermal, and micro-structural properties of its components. The mechanical stress in SOFC components, which in many cases limits their lifetime, is related to several factors including the fuel cell geometry, temperature distribution, thermal

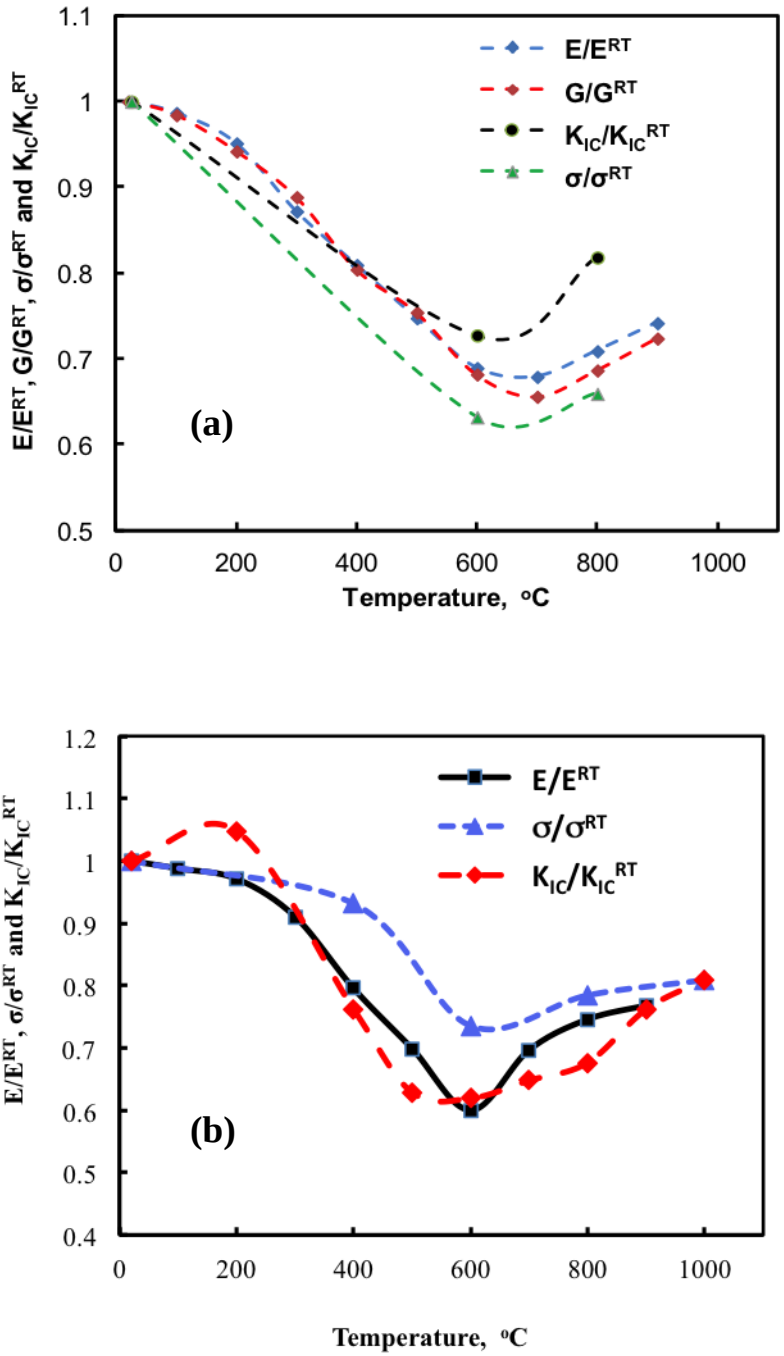

Figure 1.6. (a) The relative change of Young's modulus, E, shear modulus, G, fracture toughness, K_{IC}, and biaxial strength, σ, of 8YSZ as a function of temperature [83]. (b) the relative change of elastic modulus, E, fracture toughness, K_{IC}, and four-point bending strength, σ, of SCSZ doped zirconia as a function of temperature [84]. Superscript RT refers to room temperature value.

cycling, external loads and the properties of the constitutive materials [85-95]. Residual stresses are generated during processing because of the mismatch in the thermo-elastic properties and shrinkage during the co-sintering of SOFC's components [96-98]. Considering the electrolyte as one of the main constituents of the SOFC stack, it should have minimum thermal expansion mismatch when compared to other cell components to reduce thermal and residual stresses that depend directly on the coefficients of thermal expansion and elastic moduli of SOFC materials.

Not only electrical properties, but also thermal and mechanical properties influence the durability and stability of DBOs and even the whole devices. For example, the reliability of SOFC stack is a complex function of the electrochemical, mechanical, thermal, and micro-structural properties of its components. The mechanical stress in SOFC components, which in many cases limits their lifetime, is related to several factors including the fuel cell geometry, temperature distribution, thermal cycling, external loads and the properties of the constitutive materials [85-95]. Residual stresses are generated during processing because of the mismatch in the thermo-elastic properties and shrinkage during co-sintering of SOFC's components [96-98]. Considering the electrolyte as one of the main constituents of the SOFC stack, it should have a minimum thermal expansion mismatch when compared to other cell components to reduce thermal and residual stresses that depend directly on microstructure, the coefficients of thermal expansion (CTE) and the elastic moduli of SOFC materials.

The thermal expansions of DBOs were studied by several researchers [18, 99-103]. Both YSZ and GDC show slightly nonlinear thermal expansion change and a

gradual increase of CTE with increasing temperature [18, 100]. Both YSZ and GDC show slightly nonlinear thermal expansion change and a gradual increase of CTE with increasing temperature [18, 100]. Gibson et al. [18] carried out the neutron diffraction studies of YSZ and observed a small slope change on the lattice parameter (a) vs. temperature plots around 600 – 700 °C and proposed that this can be attributed to the short range order-disorder of oxygen vacancy-cation clusters. Most recently, Marrocchelli and Bishop et al. [103, 104] reviewed thermal expansion mechanisms in non-stoichiometric doped zirconias and cerias, and concluded that chemical and thermal expansions contribute to the overall expansion in both oxides. The chemical expansion is attributed to two competing processes, which are the formation of vacancies causing a lattice contraction and the cation radius change during reduction leading to a lattice expansion. This change of cation radius is more dominant in doped cerias from Ce^{4+} to Ce^{3+} in reducing environment or high temperatures (above 500 °C) than in doped zirconias.

The changes of the mechanical properties of electrolyte materials with temperature are non-linear and show some abnormal trends when compared to conventional oxide ceramics such as Al_2O_3. Radovic et al. [83, 105] previously observed that the elastic moduli, biaxial strength and fracture toughness of 8YSZ showed a nonlinear change with the temperature, having minimum values around 600 °C shown in Figure 1.6a. Orlovskaya et al. [84] observed a similar trends in the changes of the Young's modulus, four-point bending strength and fracture toughness of SCSZ with temperature shown in Figure 1.6b. Different mechanisms were proposed in the literature

to explain intensive decrease and the nonlinear change of mechanical properties in doped zirconias below and around 600 °C. Lakki et al. [68] observed two mechanical loss maxima and a significant drop of dynamical torsional modulus with temperature in their mechanical spectroscopy studies of fully stabilized YSZ. They proposed that anelastic relaxation due to the local ordering of oxygen vacancies contributes to the appearance of first and second mechanical loss peaks. Nowick and Ohta et al. [60, 73, 106] also explained anelastic relaxation in doped cerias and zirconias by the stress induced reorientation of elastic dipoles via the hopping of oxygen vacancies around the dopant in oxygen vacancy-dopant clusters that forms below 600 °C. Kushi et al. [55] demonstrated that the deviation of elastic modulus from the linear decrease with temperature coincides with large internal friction peaks at the same temperature ranges. However, they suggested that the main reason for the observed elastic anomaly might be some kind of the phase transformations in both SCSZ and YSZ.

1.1.7 Electro-mechanical Coupling in Doped Binary Oxides

Based on the proposed models for the reorientation of electro-mechanical dipoles under electric field or applied stresses in Figure 1.4, one would expect that the reorientation of those dipoles under applied stress would result in the simultaneous spontaneous separation of charges, i.e. the polarization of material under applied stress. However, as to our best knowledge this has not been demonstrated in the open literature.

Several researchers [106, 107] studied the relationship between anelastic relaxation and dielectric relaxation. Previous simulation models and experimental results

show the relaxation time of the anelastic relaxation is two times of that in the dielectric relaxation [107, 108], as expected. Also, the activation energies for the anelastic and dielectric relaxation processes are found to be very similar [106, 107]. For example in 8YSZ, Komine et al. [17, 109] reported that this dielectric relaxation is thermally activated with activation energy of around 1.2 eV in single crystal YSZ. Two relaxation peaks are usually observed in the mechanical loss spectra of 8YSZ: one at lower temperatures with the activation energy of 1.28 eV, which is similar to the activation energy of dielectric relaxation and is attributed to the anelastic relaxation of $(R'_M V_O^{\bullet\bullet})^{\bullet}$ dipoles, and one at higher temperatures with activation energies of 2.7 ± 0.2 eV [68, 69].

The mechanical properties and electro-mechanical coupling of YSZ, SCSZ and GDC were studied in this work since, at present, they are common electrolyte materials with a simple fluorite crystal structure. In addition, their transport properties and structural stability are relatively well known, which is helpful in understanding their mechanical behavior and electro-mechanical coupling.

1.2 Problem Statement

Stabilized zirconias and doped cerias with high ionic conductivity are currently essential materials for highly-efficient and environmentally-friendly energy technologies, including solid oxide fuel cells (SOFCs), oxygen sensors, thermal barrier coatings, batteries, etc. [20, 22, 110-113]. The ionic conductivities of DBOs are tailored by controlling the concentration of oxygen vacancies through the doping of aliovalent cations [14, 22, 75]. In most of the applications, these oxides are exposed to electrical

fields, high temperatures, mechanical stresses, and various oxygen partial pressure that strongly influence the point defects and their interactions [114].

Significant progress has been achieved in understanding the type, chemistry and structure of point defects in DBOs that are crucial for their transport properties [5, 14, 16, 22, 115]. However, the number of studies addressing the effects of point defects on the mechanical properties is surprisingly small, although those properties are crucial for the reliability and durability of many electro-chemical energy conversion devices that work under harsh environment, especially for SOFCs. However, an intense (40% – 60%) drop in the elastic moduli of stabilized zirconias from room temperature to around 600 °C severely threatens the stability of SOFCs.

The applications of DBOs are various as illustrated in the previous section, but they can be further extended. Traditional piezoelectric materials with perovskite structure such as $BaTiO_3$ (BTO) and $Pb(Zr_xTi_{1-x})O_3$ (PZT) are widely used in variety of commercial products as stress sensors, actuators, power source, sonic and ultrasonic single generators, high voltage transformers [116-119]. However, their application is limited up to around a half of Curie temperature, i.e. to around 150 °C in PZT [116]. The temperature limit cannot be pushed due to a phase transformation to a cubic non-piezoelectric phase with a centrosymmetric structure. Therefore, most of the traditional piezoelectric materials known today are used below 200 °C. A lot of research efforts have been focused on finding high temperature piezoelectric materials in last two decades [118, 120-123]. Since our results presented in the next two sections, that the stress reorientation of electro-elastic dipoles consisting of clustered vacancies and

cations lead to anelastic relaxation in DBOs, the possibility of electrical and mechanical coupling in DBOs caught our attention.

1.3 Research Objectives

The main research objective of this study is to fundamentally understand the effect of defect complexes and phase transformations on the mechanical behaviors of, and electro-mechanical coupling in, DBOs. The specific research objectives can be summarized as follows:

1. Experimentally study the effect of types, concentrations and associations of point defects and phase transformations on the mechanical properties of commercial, technologically important DBOs at elevated temperatures including thermal expansion, elastic moduli and mechanical damping;
2. Investigate how structural changes contribute to the appearance of stress-strain hysteresis loops (pseudoelastic behavior) in 8YSZ and SCSZ;
3. Study the coupling of electrical and mechanical responses in 8YSZ and SCSZ and explore the effect of point defects or their associations on their electro-mechanical behaviors.

1.4 Dissertation Organization

This dissertation includes 6 sections. Section 2 discusses microstructure, phase stability and the abnormal changes of thermal expansion and elastic moduli at elevated temperatures in electrolyte materials for high and intermediate temperature SOFCs. In

Section 3, the effects of phase transformations and anelastic relaxation on the mechanical behavior of YSZ and SCSZ at elevated temperatures were studied by dynamic mechanical analyzer (DMA). Sections 4 and 5 illustrate the interesting stress-strain hysteretic (pseudoelastic) behavior and electro-mechanical coupling in YSZ and SCSZ. Finally, Section 6 includes a brief summary of major findings and offers suggestions on future work.

2. THE THERMAL EXPANSION AND ELASTIC MODULI OF DOPED BINARY OXIDES AT ELEVATED TEMPERATURES

2.1 Summary

The development of thermal stresses in solid oxide fuel cells (SOFC), and thus their structural stability and reliability, depend directly on the thermal expansion and elastic moduli of the constituent materials. Therefore, it is important to study these properties of SOFC materials. In this section, the thermal expansion and elastic properties of common electrolyte materials, namely yttria stabilized zirconia (YSZ), scandia and ceria stabilized zirconia (SCSZ) and gadolinia doped ceria (GDC), are reported. High temperature X-ray diffraction (HT-XRD) was used to show that the cubic structure of YSZ and GDC sample is stable throughout the temperature range of 25 – 800 °C. However, SCSZ undergoes a partial cubic to rhombohedral phase transition around 300 °C but transferred completely back to cubic phase around 500 °C upon heating. The coefficient of thermal expansion (CTE) of electrolyte materials was measured using thermo-mechanical analyzer (TMA). It was found that the CTE of SCSZ is almost identical to that of YSZ, but lower than that of GDC. Elastic properties (Young's and shear moduli) were determined in the 25 – 900 °C temperature range using resonant ultrasound spectroscopy (RUS). Young's and shear moduli of GDC decrease almost linearly with temperature, with an exception of the small anomaly between 100 °C and 300 °C. However, the variation of elastic moduli with temperature was found to be highly non-linear for YSZ and SCSZ with minimum values measured around 600 °C.

The deviation from the linear decrease of elastic moduli with increasing temperature is related to the relaxation of oxygen vacancy complexes and phase transformations.

2.2 Introduction

ZrO_2 stabilized with Y_2O_3 (YSZ) has been the most important electrolyte material since the inception of SOFCs [21, 22]. Pure ZrO_2 shows a monoclinic structure below 1170 °C, tetragonal structure in the temperature range of 1170 – 2370 °C and cubic structure above 2370 °C [8]. The doping of ZrO_2 with Y_2O_3, where the amount of Y_2O_3 usually ranges from 8 mol% (8YSZ) to 10 mol% (10YSZ), not only generates one mole of oxygen vacancies per mole of dopants, but also stabilizes the high temperature cubic phase (fluorite structure) at room temperature. Below 600 °C, oxygen vacancies and dopants tend to form complexes or clusters, such as $(Y'_{Zr}V_O^{\bullet\bullet})^{\bullet}$ [10, 46-49], $(Zr_{Zr}^{x}V_O^{\bullet\bullet})^{\bullet\bullet}$ [51-53, 124], $(2Y'_{Zr}V_O^{\bullet\bullet})^{x}$ [10, 60], and cause local ordering [56-58] that hinders ionic diffusivity of YSZ. However, above ~600 °C, oxygen vacancies become free and disassociate from clusters resulting in high ionic conductivity [16, 17, 58]. Therefore, to ensure the required ionic conductivity of the electrolyte, SOFCs need to be operated at relatively high temperatures (800 – 1000 °C) where oxygen vacancies are dissociated from the clusters and become highly mobile. The latter limits the application in YSZ only to high-temperature SOFCs (HT-SOFCs) [76, 125]. The high operation temperature on the other hand causes the accelerated degradation of materials in SOFCs and high stresses due to thermal expansion mismatch between constituent materials resulting in lower reliability and durability [126-128]. Therefore, intermediate temperature SOFCs

(IT-SOFCs) have drawn attention of researchers and engineers in the recent years [37-40, 79].

10 mol% Sc_2O_3, 1 mol% CeO_2 stabilized ZrO_2 (SCSZ) and $Gd_xCe_{1-x}O_{2-0.5x}$ (x is between 0.1 and 0.2) have been largely studied as potential electrolyte materials for IT-SOFC because of their higher ionic conductivities in the 600 – 800 °C temperature range when compared to YSZ [16, 39, 79]. For example, it has been reported that SCSZ has the ionic conductivity of 0.084 S/cm at 800 °C, which is significantly higher than the conductivity of 0.03 S/cm measured in 8YSZ at the same temperature [28]. However, SCSZ undergoes partial phase transformation from cubic to rhombohedral and completely back to cubic during heating in the 300 – 500 °C temperature range [129], which consequently bring undesired residual stress in SOFC stacks.

As to GDC, although it provide much higher ionic conductivity than that of YSZ and SCSZ, it is prone to a partial reduction of Ce^{4+} to Ce^{3+} at lower oxygen partial pressure on the anode side, especially at high temperatures (above 600 °C) [40]. This reduction in GDC leads to the increased electronic conductivity as well as chemical expansion contributing to the lower cell potentials and reduced efficiency. The chemical expansion of GDC electrolyte also results in the chemical stresses and eventual cracking of GDC electrolyte layers in IT-SOFCS [39, 130, 131]. As a solution, GDC for IT-SOFC were coated with a thin layer of YSZ at the anode side to protect it from the extended reduction [41, 42].

On the other hand, mechanical and thermal properties of doped binary oxides, in addition to their transport properties are crucial for durability and reliability of SOFCs.

In a previous study, Radovic et al. [83] showed that the elastic modulus and fracture toughness of 8YSZ shows an obvious nonlinear change vs. temperature with a minimum value around 600 °C, i.e. roughly at the same temperature at which the maximum in anelastic relaxation was observed. Orlovskaya et al. [84] found the minimum values of elastic modulus and fracture toughness in SCSZ at approximately 500 °C, which is close to the operation temperature of this electrolyte material in SOFCs. The abnormal changes of mechanical behavior in SCSZ were attributed to the phase transformations from cubic to rhombohedral and then back to cubic in the temperature range of 300 – 500 °C. Nowick et al. [60] and Weller et al. [10, 70] observed large mechanical damping peaks (internal friction peaks) in both doped cerias and zirconias below 600 °C. Kushi et al. [55] showed that the drastic drops of elastic moduli occur in the same temperature range where mechanical damping peaks were observed in both YSZ and SCSZ.

A detailed study of the variation of thermo-mechanical properties of common electrolyte materials for HT-SOFCs and IT-SOFCs as a function of temperature are presented in this section. In the present work we have investigated the coefficient of thermal expansion in the 25 – 800 °C/900 °C temperature range using HT-XRD and TMA, and elastic moduli by a custom built high temperature RUS. The results presented in this work are not only important for designing more mechanically and structurally robust SOFCs, but also for a better understanding of mechanisms that lead to the non-linear changes of elastic moduli with temperature in common FICs having fluorite structure.

2.3 Materials and Experimental Methods

The electrolyte materials used in this study include 8 mol% Y_2O_3 stabilized ZrO_2 (8YSZ) and 10 mol% Y_2O_3 stabilized ZrO_2 (10YSZ) as conventional electrolytes for HT-SOFC, as well as 10 mol% Sc_2O_3 + 1 mol% CeO_2 stabilized ZrO_2 (SCSZ), $Gd_{0.1}Ce_{0.9}O_{0.95}$ (10GDC) and $Gd_{0.2}Ce_{0.8}O_{0.9}$ (20GDC) for IT-SOFC. Commercial 8YSZ (TOSOH Corp., Japan), 10YSZ (TOSOH Corp., Japan), SCSZ (Daiichi Kigenso Kagaku Kogyo Co. Ltd., Japan), 10GDC (Fuel Cell Materials, OH) and 20GDC (Fuel Cell Materials, OH) powders were uniaxially cold pressed at 20 MPa for 4 minutes in a half inch or one inch diameter steel die. The green pellets were sintered in ambient air at 1500 °C for 2 hours with a heating and cooling rate of 5 °C/min. All examined samples were fabricated in the form of rods or discs. Samples were cut to 4 x 4 x 8 mm^3 rectangular bars for TMA test and 10 mm diameter and 2 mm thick discs for HT-RUS test.

The relative density of all samples was measured to be higher than 97% after sintering using alcohol immersion method and the Archimedes' principle according to ASTM Standard C20-00 [132]. The sintered samples were crushed to powders and characterized with high temperature X-ray diffraction (HT-XRD; X'Pert Pro X-ray Diffraction System, PANalytical, Westborough, MA) with Cu Kα radiation (wavelength=1.542 Å) at 45 kV and 40 mA. The two-theta range varied from 20° to 80° with a step size of 0.02° and a step time of 1 s. Heating and cooling rates were 5 °C/min and soaking time at the desired temperature was 20 minutes before scanning. Phase compositions were analyzed utilizing the Inorganic Crystal Structure Database (ICSD)

and MDI Jade software. To study the grain size after sintering, samples were mechanically polished to a mirror finish using SiC sandpapers with different grits, and then using different size diamond suspensions (from 9 μm to 0.1 μm). Well-polished samples went through thermal etching at 1400 °C for half an hour. The grain size of samples were observed and measured with digital optical microscope (Keyence VH-Z100) and field emission scanning electron microscope (FE-SEM; Quanta 600 FEG, FEI, Oregon, USA). Average grain sizes were calculated by measuring the size of 200 grains.

Coefficients of thermal expansion (CTE) of the examined materials were determined using Q400 series thermomechanical analyzer, TMA (TA Instruments, IL, USA). The 4 x 4 x 8 mm^3 sample cut from sintered discs was placed between the stage and glass probe. The displacement of the probe that corresponds to the expansion of the sample along longest direction was monitored during heating and cooling. A standard Al_2O_3 sample was used to calibrate the equipment before tests. The tests were performed in a standard mode in which the force was held with a constant stress at 0.1 N during the test. Each sample was subjected to three consecutive heating-cooling thermal cycles. Each thermal cycle included a heating process from the room temperature to 900 °C with a heating rate of 5 °C/min, followed by a cooling process to room temperature at a rate of 5 °C/min, as given by the ASTM E831 standard [133]. The height changes (in μm) of the sample with temperature during three heating and cooling cycles were monitored and recorded. The weight of the sample was measured before and after every test to ensure that there was no change related to the oxidation or reduction of the sample.

The Young's and shear moduli of the materials used in the present study were determined using a custom made high-temperature resonant ultrasound spectroscopy (HT-RUS) that utilizes commercially available RUS (Magnaflux Quasar, Albuquerque, NM) system. RUS is a high-precision dynamic technique which is used to determine the elastic moduli and energy dissipation (mechanical damping) of the materials by measuring the vibrational spectrum of the samples with well-defined geometry, usually in the shape of parallelepipeds or cylinder [134, 135]. The details of the experimental set up for resonant ultrasound spectroscopy can be found elsewhere [134, 136, 137]. The sample in the form of a disc was supported by three piezoelectric transducers. One transducer (transmitting transducer) generates an elastic wave of constant amplitude but of varying frequency (covering a large number of vibrational eigenmodes of the sample). The resonance response of the excited sample is detected by the other two transducers (receiving transducers). In order to study the variation of elastic moduli and energy dissipation as a function of temperature, the commercially available setup for RUS at room temperature was further modified for high temperature measurements in which large sapphire or SiC extension rods were used to transmit ultrasound waves. This arrangement was designed to hold the specimen on the tip of the extension rods at the desired temperature in the furnace while keeping the transducers unaffected by high temperature. The sample was heated at a ramping rate of 10 °C/min and resonance spectra were collected at an interval of 100 °C up to 900 °C after an isothermal hold of 20 minutes.

Depending on the density and stiffness of the material, measurements were done in the 20 – 500 kHz frequency range to cover the first 40 eigenfrequencies. The RUS spectra cannot be de-convoluted directly to deduce the elastic constants. Starting from the known sample dimensions, density, and a set of "guessed" elastic constants—namely C_{11} and C_{44} for an isotropic solid, the elastic moduli were determined from collected RUS spectra using a multidimensional algorithm (Magnaflux Quasar, Albuquerque, NM) that minimizes the root-mean-square (RMS) error between the measured and calculated resonant peaks. Energy dissipation (Q^{-1}) is obtained by the Full Width at Half Maximum (FWHM) of the resonant peaks.

2.4 Results and Discussion

2.4.1 Structural Characterization

It is well established by now that the grain size could affect the phase stability and ionic conductivity in doped cerias and zirconias [138, 139]. For example, possible phase transformation could be of concern in the zirconia-based fluorite solid ionic conductors since fluorite structure is a metastable structure at low temperatures. As discussed before by many researchers [33, 57], phase transformation from cubic to tetragonal or other structures may take place in 8YSZ leading to the poor ionic conductivity [140, 141]. Zevalkink et al. [138] also showed that SCSZ goes through phase transformations from cubic to rhombohedral around 300 °C, and then back to cubic around 500 °C. More recently, Yarmolenko et al. [129] observed that the grain size of SCSZ influences the fraction of transformed rhombohedral phase. As it was discussed

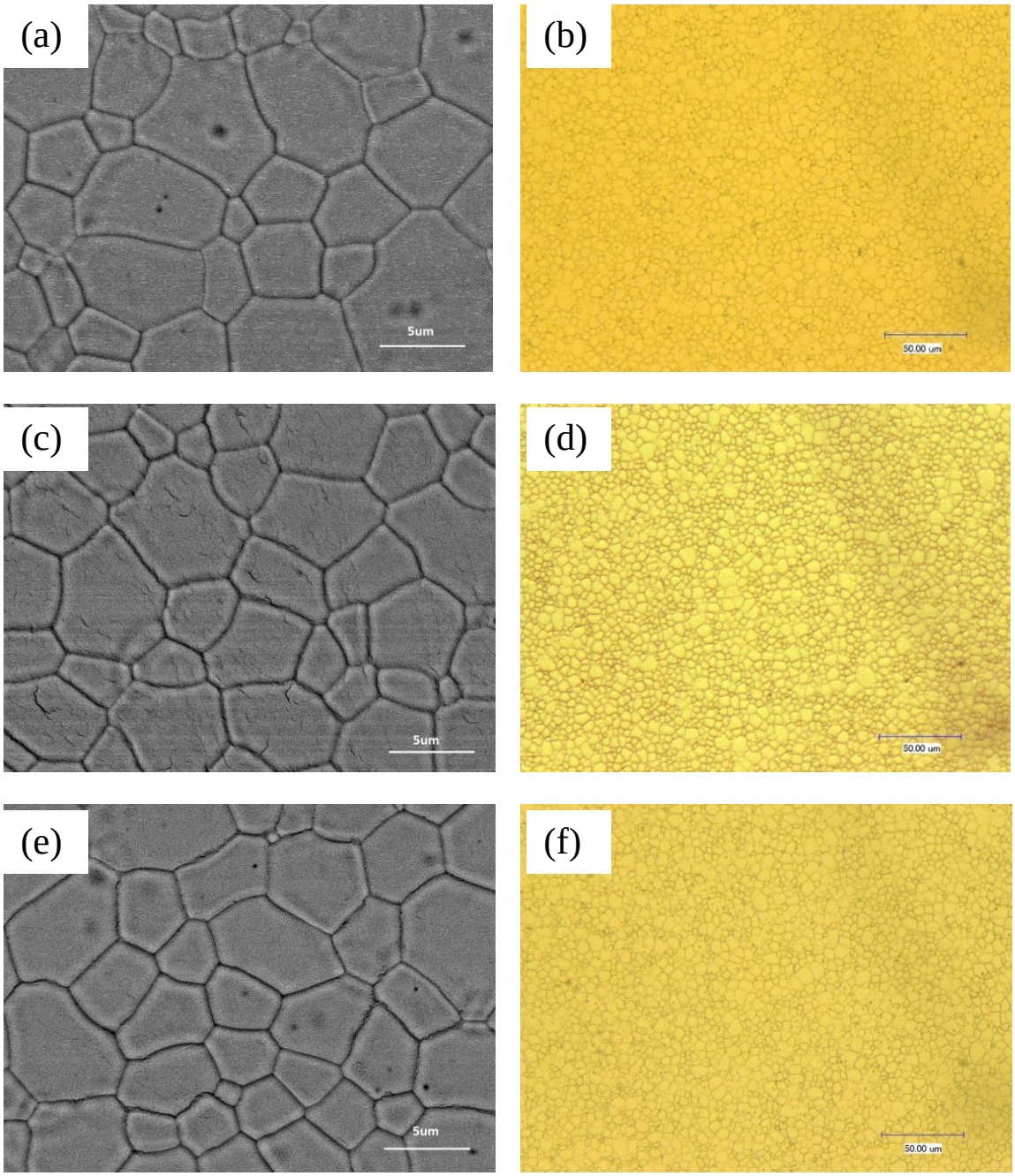

Figure 2.1. The SEM images of (a) 8YSZ, (c) SCSZ, (e) 20GDC and the optical microscopy images of (b) 8YSZ, (d) SCSZ, (f) 20GDC after thermal etching.

before by many researchers [139, 142, 143], the transport properties of GDC and YSZ also largely depend on grain sizes.

To eliminate the possible influence of different grain sizes on thermal properties, elastic properties and phase compositions, all samples of different materials in this study were processed targeting comparable grain sizes. SEM (Figure 2.1a, c, e) and optical microscopy (Figure 2.1b, d, f) were used to determine the grain sizes in well-polished samples after thermal etching. The average grain sizes of 8YSZ, 10YSZ, SCSZ, 10GDC, and 20GDC and were found to be 4.93±1.60 μm, 5.02±1.62 μm, 4.85±1.40 μm, 5.17±1.53 μm, and 5.24±1.48 μm, Table 2.1. In other words, grain sizes in all samples were comparable and around 5 μm.

Table 2.1. Grain sizes and coefficients of thermal expansions obtained from XRD and TMA results for different SOFC electrolyte materials.

Sample	Grain size	CTE from XRD (30 to 800 °C)	Average CTE form TMA (30 to 900 °C)
	μm	/°C	/°C
8YSZ	4.93±1.60	10.51×10^{-6}	10.31×10^{-6}
10YSZ	5.02±1.62	10.56×10^{-6}	10.38×10^{-6}
SCSZ	4.85±1.40	10.33×10^{-6}	10.52×10^{-6}
10GDC	5.17±1.53	12.00×10^{-6}	12.09×10^{-6}
20GDC	5.24±1.48	12.22×10^{-6}	12.22×10^{-6}

Figure 2.2 shows the HT-XRD results for 8YSZ, SCSZ and 20GDC. 8YSZ (Figure 2.2a) and 20GDC (Figure 2.2d) XRD patterns from room temperature to 800 °C indicate that only fluorite structure is present in both samples during heating. However, in SCSZ, a partial phase transformation from cubic to rhombohedral and back to cubic

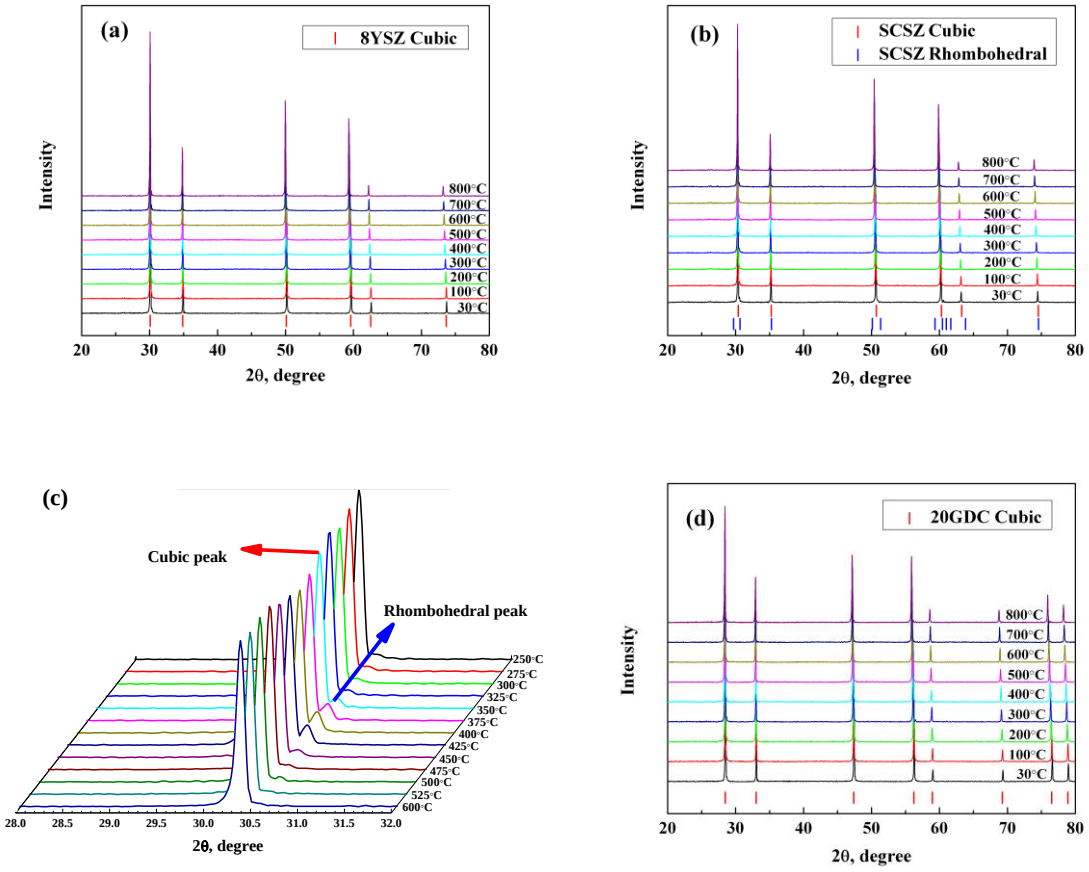

Figure 2.2. The high temperature XRD result of (a) 8YSZ, (b) SCSZ, (c) magnified results for SCSZ in the 28° – 32° 2θ range and (d) 20GDC.

was observed in the temperature range of 300 – 500 °C during heating (Figure 2.2b and 2.2c). The results of XRD with smaller temperature steps in Figure 2.2c show that the rhombohedral peaks appear in SCSZ around 300 °C, and then they gradually disappear until 500 °C. The lattice parameters of 8YSZ, 10YSZ, SCSZ, 10GDC and 20GDC

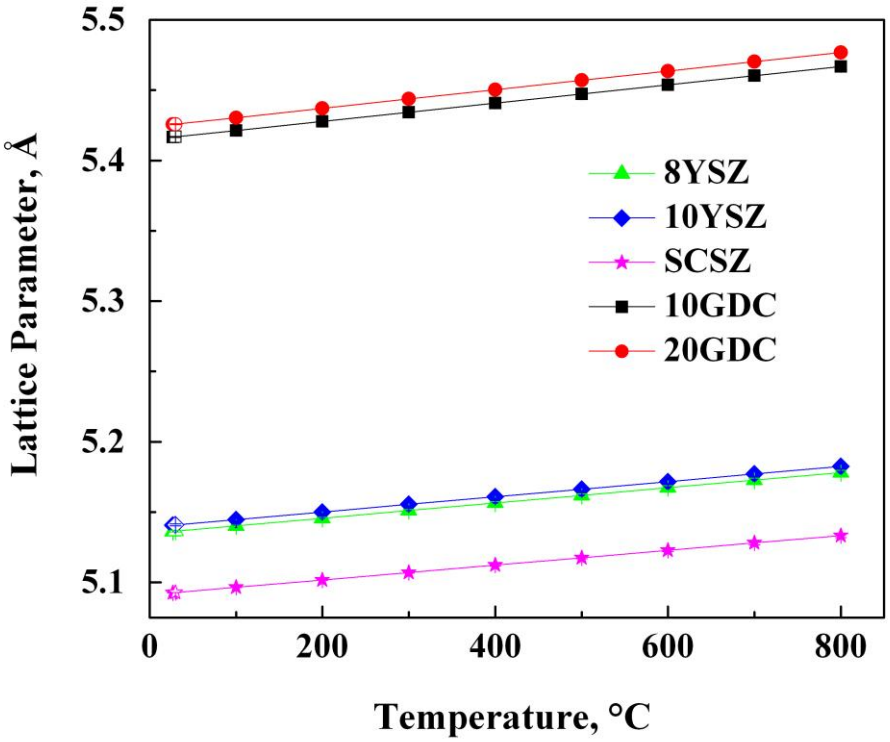

Figure 2.3. The lattice parameter changes of 8YSZ, 10YSZ, SCSZ, 10GDC and 20GDC vs. temperature. The open symbols represent lattice parameters at 30 °C obtained after heating process.

increase almost linearly with the temperature as shown in Figure 2.3. The figure also shows that the lattice parameter values remain unchanged after a heating-cooling cycle as compared to the room temperature lattice parameters of as processed samples. Thermal expansion coefficient from 30 to 800 °C calculated from HT-XRD results (Table 2.1) are 10.51×10^{-6}/°C, 10.56×10^{-6} /°C, 10.33×10^{-6} /°C, 12.00×10^{-6} /°C, and 12.22×10^{-6} /°C, and for 8YSZ, 10YSZ, SCSZ, 10GDC and 20GDC, respectively. Note here that the lattice parameter changes with temperature presented for SCSZ in Figure

2.3 and the corresponding coefficients of thermal expansions reported above are only for the cubic (fluorite) phase in SCSZ.

2.4.2 Thermal Expansion

Figure 2.4 shows results obtained from thermomechanical analysis (TMA) of 8YSZ, 10YSZ, SCSZ, 10GDC and 20GDC samples. Thermal expansion ($\Delta L/L_0$) vs. temperature plots in Figure 2.4a, 2.4c and 2.4e show almost a linear increase of $\Delta L/L_0$ with temperature in the 25 – 900 °C temperature range, with a similar trend to that was observed in the case of lattice parameter changes in Figure 2.3. All samples were tested in three heating-cooling cycles and since the overlaps between curves obtained in all heating-cooling cycles were good, only results from the first heating and cooling cycle are presented for each material. The slopes of the straight lines fitting of data in Figure 2.4a, 2.4c and 2.4e give the average coefficients of thermal expansion (CTE) of 10.31×10^{-6} /°C, 10.38×10^{-6} /°C, 10.52×10^{-6} /°C, 12.09×10^{-6} /°C, and 12.22×10^{-6} /°C for 8YSZ, 10YSZ, SCSZ, 10GDC and 20GDC, respectively, Table 2.1. It is worth pointing out that the CTE of GDCs is higher than that of examined YSZs and SCSZ. Those values are in good agreement with coefficients of thermal expansion determined using HT-XRD results, as it is shown in Table 1. The results from three heating and cooling cycles are in excellent agreement with the CTE values reported elsewhere for YSZ [99, 102, 144, 145], SCSZ [140] and GDC [101, 146].

Instantaneous thermal expansions at any temperature in the 25 – 900 °C temperature range was also calculated from the thermal expansion vs. temperature curve

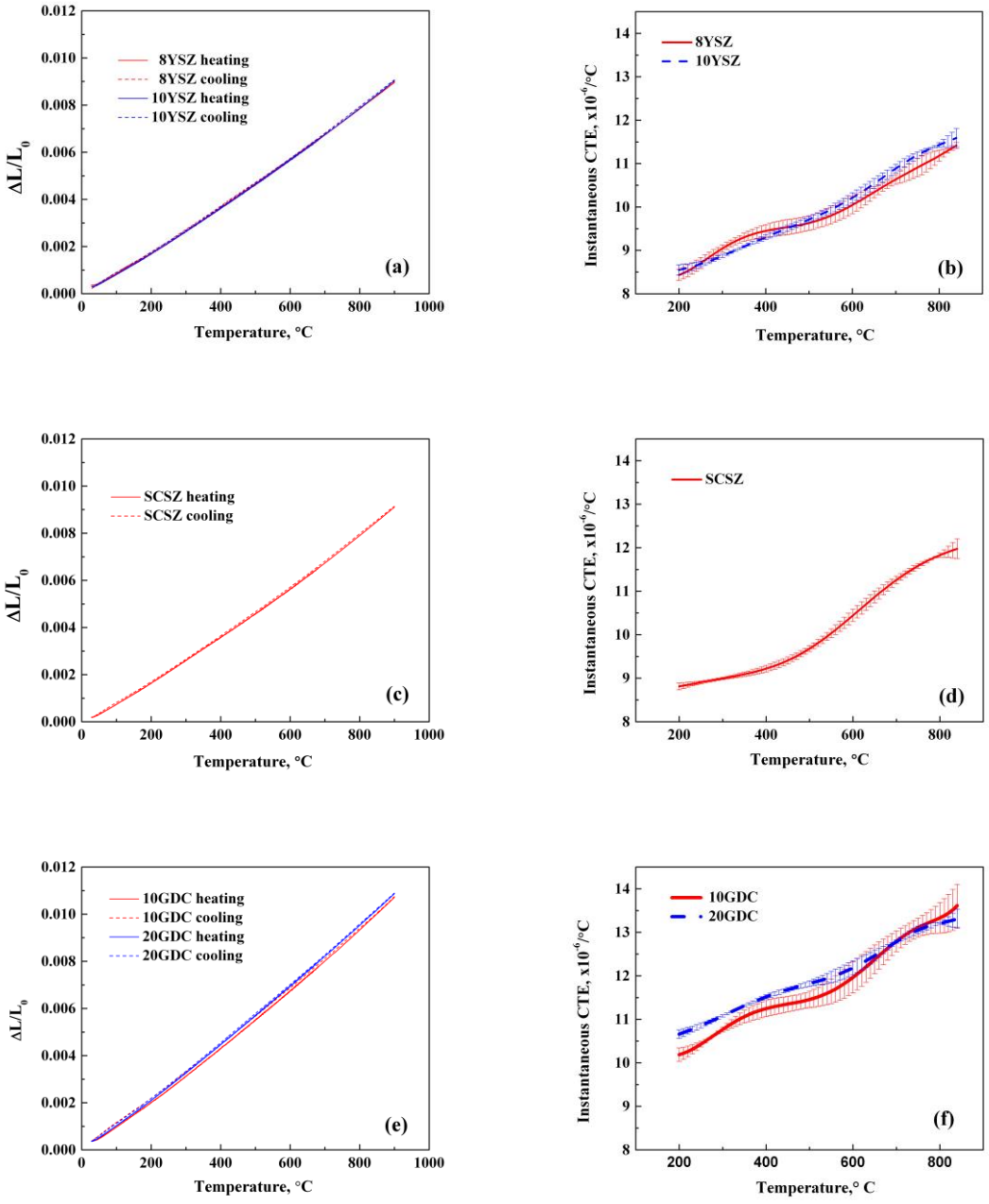

Figure 2.4. The thermal expansion vs. temperature of (a) 8YSZ and 10YSZ, (c) SCSZ, (e) 10GDC and 20GDC, and instantaneous CTE vs. temperature plots for (b) 8YSZ and 10YSZ, (d) SCSZ, (f) 10GDC and 20GDC. Error bars in (b), (d) and (f) represent standard deviations from measurements in three heating and three cooling cycles.

as $\mathrm{CTE} = \frac{1}{L_0}\frac{dL}{dT}$, where, L_0, L and T are the original length of sample at room temperature, length and temperature, respectively. Therefore, the instantaneous CTE was determined as a slope of the tangent on thermal expansion vs. temperature curve at each particular temperature. Figure 2.4b, 2.4d and 2.4f show the average value of instantaneous CTEs from three heating and cooling cycles. The magnitudes of instantaneous CTEs increase slightly with increasing temperature for all examined samples.

Instantaneous CTE vs. temperature plots for 8YSZ and 10YSZ in Figure 2.4b clearly show a monotonic increase of CTE with increasing temperature. The saddle point around 600 °C followed by the increasing slope of instantaneous CTE vs. temperature curve may be attributed to an order-disorder transition in 8YSZ. Previous neutron diffraction results suggested that the order-disorder transition is a results of the dissociation of vacancy-cation complexes or clusters in 8 mol% YSZ in the 600 – 700 °C temperature range could result in a slight change of the slope of lattice parameter vs. temperature curve around that temperature [18].

The change of instantaneous CTE with increasing temperature in SCSZ (Figure 2.4d) is similar to that in YSZ. However, the obvious change of the slope around 500 °C in SCSZ may be attributed to the phase transformations. As it was shown in the XRD results (Figure 2.2b and Figure 2.2c), complex phase transformations take place in SCSZ between 300 °C and 500 °C. Yarmolenko et al. [140] has shown that the cubic phase SCSZ (10.6×10^{-6} °C^{-1}) has significantly higher CTE than rhombohedral phase (8.6×10^{-6}

$°C^{-1}$). This may contribute to the relative slower slope increase in the temperature below 500 °C and the sudden increase of instantaneous slope at the temperature around 500 °C observed in Figure 2.4d. As in the case of YSZ, the increase in the slope of instantaneous CTE vs. temperature curve above 600 °C in SCSZ may also be attributed to the order-disorder transition. Although more work is needed to fully understand the underlying mechanisms for the observed changes in instantaneous CTE with temperature in SCSZ, we conclude at this point that those changes should be most likely associated with the local ordering of defect complexes and phase transformations.

In the case of GDC, a noticeable increase in the instantaneous CTE above 600 °C in Figure 2.4f coincides more with the onset of intensive oxygen vacancy formation and corresponding chemical expansion in GDC [39, 130, 146]. Although the increase of oxygen vacancies leads to the contraction of lattice, the loss of oxygen atoms lead to the reduction of Ce^{4+} (ionic radius: 0.97 Å) to Ce^{3+} (ionic radius: 1.143 Å), which can also largely contribute to the increase of instantaneous CTE probably together with the order-disorder transition [147].

2.4.3 Elastic Moduli

The results of RUS in the 30 – 900 °C temperature range for YSZ, SCSZ and GDC are summarized in Figures 2.5 – 2.8. Before discussing the changes of Young's and shear moduli with temperature in those typical electrolyte materials, it is worth mentioning that resonant spectra obtained by RUS show some interesting anomalies. For example, selected but typical resonant peaks for 20GDC (Figure 2.5a) and 8YSZ (Figure

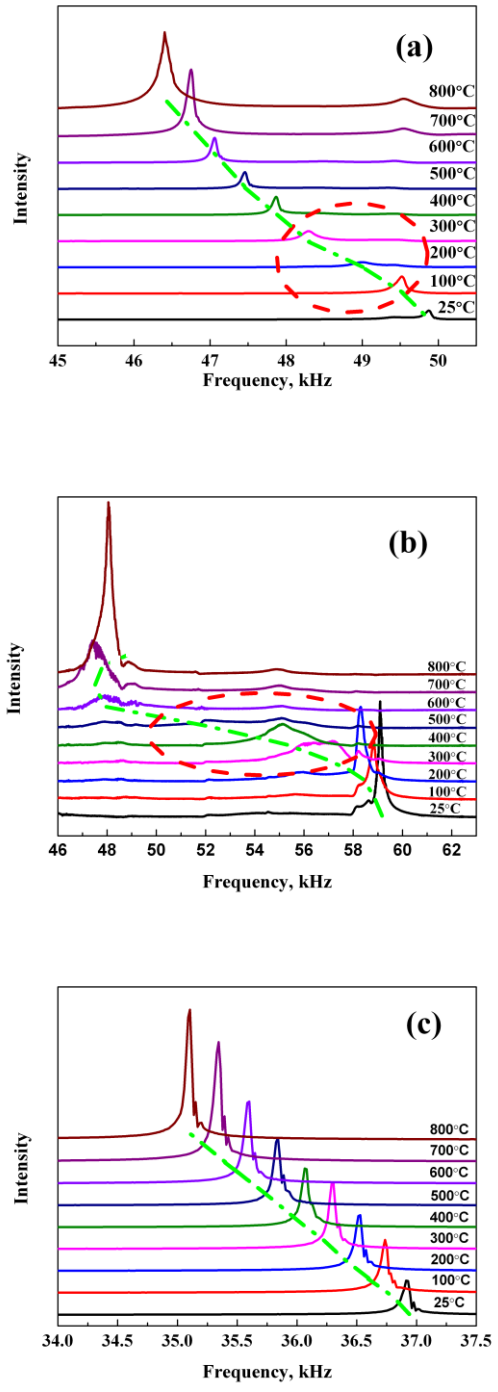

Figure 2.5. The typical but selected RUS resonant peaks at different temperatures for (a) 20GDC, (b) 8YSZ and (c) Al_2O_3.

2.5b) show not only a shift of resonant peaks to the lower frequencies with increasing temperature (labeled with green dash lines in Figure 2.5) as the result of a decrease in elastic moduli, but also a broadening and significant decrease in their intensity in certain temperature ranges. However, other typical oxides, such as Al_2O_3 shown in Figure 2.5c do not show any significant broadening of resonant peaks in the entire temperature range. The broadening of the resonant peak is observed in doped cerias and zirconias in the 100 – 400 °C and 300 – 700 °C temperature ranges, respectively. As the full width at half maxima (FWHM) of the resonant peaks represent ultrasonic attenuation, the broadening of the resonant peaks can be attributed to the attenuation increase of ultrasonic wave (or mechanical loss). The attenuation indicates that the energy of the ultrasonic waves is dissipated more in a certain temperature ranges in examined doped binary oxides.

Figures 2.6 shows the change of Young's and shear moduli with temperature for 8YSZ, 10YSZ, SCSZ, 10GDC and 20GDC. For comparison, the elastic moduli of Al_2O_3 are also plotted as a function of temperature in Figure 2.6. While the Young's and shear moduli of Al_2O_3 decrease linearly with increasing temperature, the change with temperature deviates from the linear trend for all examined electrolyte materials. 10GDC and 20GDC show slight deviations from the linear decrease of elastic moduli with temperatures between 100 °C and 400 °C (Figure 2.6). The changes of elastic moduli of 8YSZ, 10YSZ and SCSZ with temperature deviate even more from the linear trend with minimum values of elastic moduli around 600 °C. Above 600 °C, the elastic moduli were even found to increase slightly with increasing temperature in all doped zirconias. The

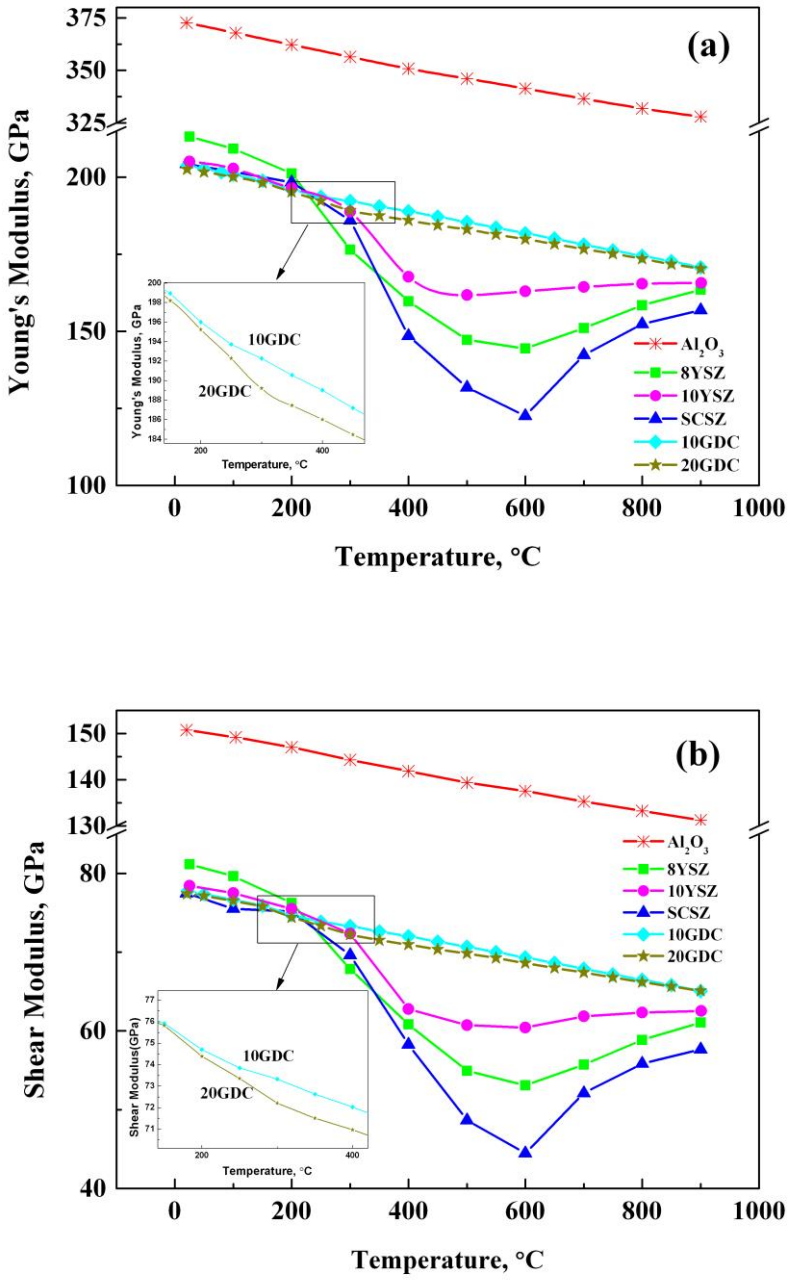

Figure 2.6. (a) The Young's modulus and (b) shear modulus of Al_2O_3, 8YSZ, 10YSZ, SCSZ, 10GDC and 20GDC determined by RUS.

drops in elastic moduli are quite significant from room temperature to approximately 600 °C, i.e. they are 32.3 %, 20.5 % and 40.0 % in the Young's modulus and 34.6 %, 23.0 % and 42.6 % in the shear modulus of 8YSZ, 10YSZ and SCSZ, respectively. Figure 2.7 compares normalized Young's moduli (i.e. Young's moduli at any temperature divided by Young's moduli at room temperature) that were obtained in this study using RUS for 8YSZ, 10YSZ and SCSZ to those measured using dynamic mechanical analysis (DMA) (see Section 3 for more details) [69]. Although the changes of normalized elastic moduli with temperature in Figure 2.7 were determined using two different dynamic methods, they show quite similar trends. However, the minimum values of elastic moduli determined by RUS are shifted towards higher temperatures when compared to the results from DMA. The reason for the observed shift of elastic modulus minima to higher temperatures in RUS lies in the fact that this drop in elastic moduli is frequency dependent, i.e. it appears at higher temperatures as the measurements were carried out at higher frequencies, as it is discussed in more details later in Section 3 [69]. The RUS measurements in this study were performed in the 20 – 500 kHz range, which is significantly higher than the frequency range of 0.1 – 100 Hz that was used in DMA tests in Section 3 [69].

Figure 2.8 shows mechanical loss (Q^{-1} or tan δ) obtained from the FWHM of resonant peaks (such as those in Figure 2.5). RUS allows not only a simultaneous measurement of more than one elastic constant but also a determination of ultrasonic attenuation (Q^{-1}) as a direct manifestation of irreversible energy absorption by various physical processes. Q^{-1} can be determined from the RUS spectra assuming: Q^{-1}_k =

$\Delta\omega_k/\omega_{ko}$, where ω_{ko} is the frequency associated with k_{th} eigenmode, and $\Delta\omega_k$ is the FWHM of that mode. Large mechanical damping peaks appear in the 100 – 300 °C temperature range for 10GDC and 20GDC, 200 – 700 °C for 8YSZ, 200 – 600 °C for

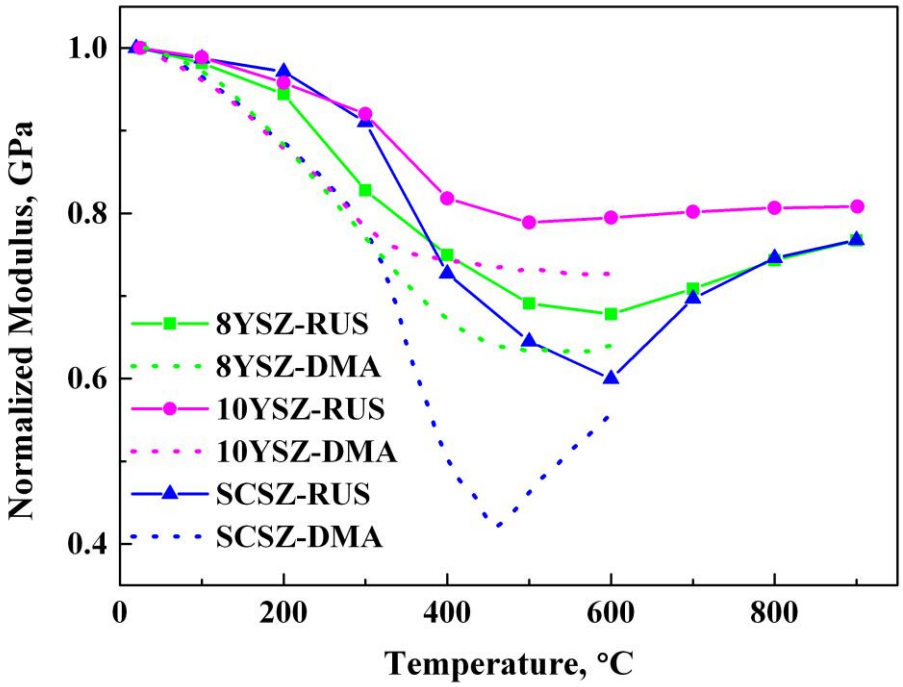

Figure 2.7. The comparison of the normalized Young's modulus of 8YSZ, 10YSZ and SCSZ obtained by RUS and DMA.

10YSZ and 200 – 700 °C for SCSZ, in which is the same temperature range in which a noticeable deviation from the linear decrease of elastic modulus with temperature was observed (Figure 2.6). This suggests that the drop in elastic moduli and increase in mechanical damping are linked phenomena affected by the same physical mechanism(s).

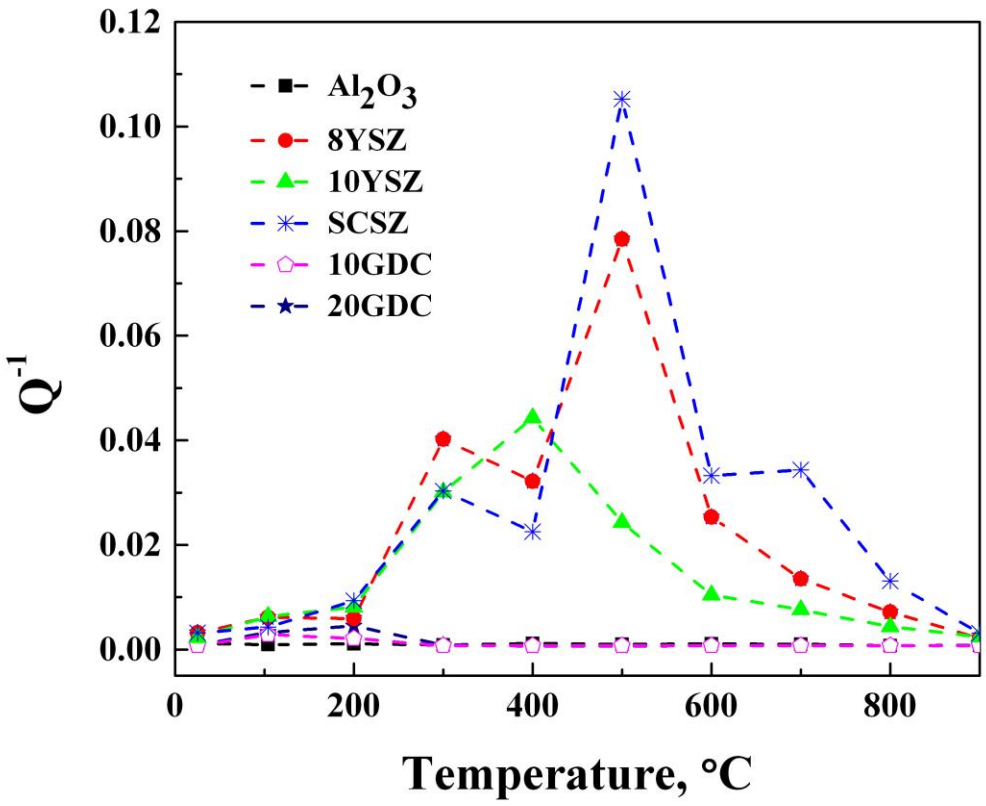

Figure 2.8. The comparison of mechanical damping in 8YSZ, 10YSZ, 10GDC and 20GDC by RUS. The mechanical damping of Al_2O_3 is also shown for comparison.

In addition, stabilized zirconias show much larger mechanical loss peaks than doped cerias, and consequently a much higher drop in elastic moduli with temperature. It is worth noting that mechanical damping peaks for 8YSZ are larger than that of 10YSZ, but smaller than SCSZ. The similar damping peaks were obtained using DMA in 8YSZ, 10YSZ and SCSZ in Section 3 [69], but with maximum values at significantly lower temperatures (approximately 200 °C lower) than those reported here, because those tests were carried out at much lower frequencies. To further elucidate the possible

mechanisms that result in this unusual changes of elastic moduli and high mechanical damping in 8YSZ and 10YSZ, the results in Figure 2.5 – 2.8 were further analyzed and compared to the results obtained using DMA in Section 3 [69].

Previous studies have shown that the elastic moduli of single crystal and polycrystalline zirconia doped with yttria [55, 148, 149], scandia [55], and calcia [27] non-linearly decrease with temperature with a significant drop in moduli at temperatures that corresponds to the maximum of mechanical damping (i.e. mechanical loss or internal friction) which can be expressed as $Q^{-1} \approx \tan \delta = E''/E'$, where δ is loss angle, and E' and E'' are the real and imaginary part of elastic modulus, respectively. As will be discussed in more detail in Section 3 [69], the drop of elastic moduli as well as the peaks in the mechanical loss (Q^{-1}) spectra can be attributed to the anelastic relaxation of elastic (and dielectric) dipoles by the hopping of the oxygen vacancies around cations and/or local ordering of oxygen vacancies. At lower temperatures, mechanical loss is most likely associated with the anelastic relaxation of simple dipoles such as $(Y'_{Zr}V_O^{\bullet\bullet})^{\bullet}$, while at higher temperatures it may be caused by the anelastic relaxation of more complex clusters such as $(2Y'_{Zr}V_O^{\bullet\bullet})^{x}$ [10, 148], and/or local ordering of oxygen vacancies [58, 68].

Phase transformations were also proposed in some studies [55, 150, 151] as other possible mechanisms that can lead to the non-linear change of elastic moduli and observed mechanical damping peaks. As it is discussed by Navrotsky [57], the cubic structure has a large possibility to transform to a locally fluorite-derivative structure (delta phase) or other similar structures (pyrochlore, bixbyite, zirconolite) in some doped

binary oxides. However, our high temperature XRD results showed that the cubic crystal structure is stable in 8YSZ (Figure 2.2a) and 10YSZ (not shown here) in the entire temperature range. Gibson et al. [18] also did not observe any first order phase transformations in 8YSZ using neutron diffraction between 150 and 1000 °C, while Cai et al. [152] reported that cubic structure is entirely stable in 10YSZ in the temperature ranges of -233 – 1197 °C tested using high temperature Raman spectroscopy. Finally, the absence of any abrupt changes in the coefficients of thermal expansion and the fact that the temperature at which maximum attenuation occurs is frequency dependent almost exclusively rule out any long-range first order phase transformations in YSZ samples.

Similar to YSZ, the anelastic relaxation of dipoles such as $(Sc'_{Zr}V_O^{\bullet\bullet})^{\bullet}$ and $(2Sc'_{Zr}V_O^{\bullet\bullet})^{x}$, and possibly local ordering of oxygen vacancies may also be responsible for the intense decrease of elastic moduli and the increase of mechanical damping that was observed in SCSZ. However, unlike in YSZ, two phase transformations in SCSZ were detected between 300 °C and 500 °C by high temperature XRD in this (Figure 2.2b and 2.2c) and several other studies [37, 129]. In addition, the phase transformations could be assisted by external applied stress or residual stress [153]. The drop in elastic moduli is more significant and the mechanical damping is larger (Figure 2.8) in SCSZ than in YSZ between 300 °C and 500 °C suggesting that those phase transformations in SCSZ might have a huge influence on its elastic moduli and mechanical damping.

The room temperature Young's modulus of 10GDC (2.1 % Porosity—204 GPa) and 20GDC (2.7 % Porosity—202 GPa) used in the present study are slightly lower than

those reported in literature (212 GPa) for almost fully dense samples [154]. Unlike in the case of YSZ and SCSZ, the elastic moduli of 10GDC and 20GDC decrease almost linearly with temperature, with only slight deviation from the linear trend between 100 °C and 400 °C. However, as in the case of doped zirconias, an increase in mechanical damping was also observed, although the magnitude of the mechanical damping was significantly lower in GDCs than in doped zirconias. As it was proposed earlier by Nowick and his collaborators [60, 71] who carried out the torsional pendulum studies of several doped cerias, mechanical damping in this temperature range can be attributed to the anelastic relaxation of elastic dipoles such as $(Gd'_{Ce}V_O^{\bullet\bullet})^{\bullet}$ and $(2Gd'_{Ce}V_O^{\bullet\bullet})^{x}$. The low magnitude of mechanical damping and temperature range in GDCs is not surprising if we take into account the results of previous experimental and computational studies [10, 39, 71, 155, 156] that clearly show that the association energies of oxygen vacancy-cation are much lower in GDCs than YSZs, which in turn also contribute to the superb ionic conductivity of GDCs at much lower temperatures when compared to YSZs. Consequently, the deviation from the linear change of elastic moduli with temperature and mechanical damping peak appear at approximately 100 °C higher temperatures in 20GDC than in 10GDC since more complex clusters, such as $(2Gd'_{Ce}V_O^{\bullet\bullet})^{x}$ dipoles, and/or more local orderings are formed in the former with a higher association energy [70, 71].

2.5 Conclusions

In the present work, we report on the changes of coefficients of thermal expansion and elastic moduli in the 25 – 900 °C temperature range for 8 mol% Y_2O_3 stabilized ZrO_2 (8YSZ) and 10 mol% Y_2O_3 stabilized ZrO_2 (10YSZ) as conventional electrolytes for high temperature SOFC, as well as 10 mol% Sc_2O_3, 1 mol% CeO_2 stabilized ZrO_2 (SCSZ), $Gd_{0.1}Ce_{0.9}O_{1.95}$ (10GDC) and $Gd_{0.2}Ce_{0.8}O_{1.9}$ (20GDC) for intermediate temperature SOFC, all having the microstructure consisting of ~5 μm grains. It was found that the fluorite structure was stable from 30 °C to 800 °C in 8YSZ, 10YSZ, 10GDC and 20GDC using high temperature X-ray diffraction. In SCSZ, a partial phase transformation from cubic to rhombohedral, and then back to cubic were observed in the temperature range of 300 – 500 °C.

The thermal expansion of the examined electrolyte materials was determined using high temperature XRD and TMA, while Young's (E) and shear moduli (G) as well as ultrasonic attenuation (Q^{-1}) were determined using RUS. The coefficient of thermal expansion (CTE) of SCSZ was found to be almost identical to that of YSZ, but lower than that of GDC. The deviations in CTE changes with temperature around 600 °C could be an indication of order-disorder transitions in these electrolyte materials, i.e. 8YSZ, 10YSZ, SCSZ, 10GDC and 20GDC. In addition, phase transformations, which take place between 300 °C and 500 °C in SCSZ, might have effect on its CTE. A large increase in the instantaneous CTE of GDC above 600 °C is most likely the results of chemical expansion.

The variation of elastic moduli with temperature was found to be highly non-linear for YSZs and SCSZ with the minimum magnitudes of Young's and shear moduli at about 600 °C. It was found that for those stabilized zirconias, the temperature showing the minimum value of elastic moduli vs. temperature curves corresponds to the temperature of maximum mechanical loss due to phase transformations in SCSZ, the most likely anelastic relaxation of dipoles and probably the local ordering of oxygen vacancies in all zirconias. However, in GDCs where activation energies for the reorientation of vacancy-dopant complexes is much lower than in YSZ and SCSZ, the deviations from the linearity of elastic moduli with temperature appear at much lower temperatures (200 – 400 °C) with smaller mechanical loss peaks, when compared to doped zirconia ceramics.

3. THE EFFECT OF PHASE TRANSFORMATIONS AND ANELASTIC RELAXATION ON MECHANICAL BEHAVIORS IN STABILIZED ZIRCONIAS*

3.1 Summary

Elastic properties of polycrystalline stabilized zirconias, namely Yttria Stabilized Zirconia (YSZ) and Scandia, Ceria Stabilized Zirconia (SCSZ), were studied by Dynamic Mechanical Analyzer (DMA) in air. Changes of storage modulus E', loss modulus E'' and mechanical damping (tanδ or Q^{-1}) with temperature were simultaneously monitored at various frequencies. In 8 mol% (8YSZ) and 10 mol% (10YSZ) Yttria Stabilized Zirconia, a drop in storage modulus of ~37% was observed in the 30 °C to 400 °C temperature range, together with two frequency dependent damping peaks. While the first tanδ peak can be attributed to the anelastic relaxation of $(Y'_{Zr}V_O^{\bullet\bullet})^{\bullet}$ elastic (and dielectric) dipoles, the second one is probably the result of local ordering of oxygen vacancies and/or relaxation of $(2Y'_{Zr}V_O^{\bullet\bullet})^{x}$ dipoles. For cubic SCSZ, four damping peaks were observed in the similar temperature regime accompanied by significant nonlinear drop in the (E′). The first tanδ is attributed to anealstic relaxation of $(Sc'_{Zr}V_O^{\bullet\bullet})^{\bullet}$. It was also found that stress induced phase transformation from cubic to rhombohedral structure is the reason for the frequency dependent third peak in the tanδ spectra while the fourth frequency independent peak was found to be the result of the first order phase transformation from rhombohedral to cubic structure.

---

* Reprinted with permission from "Dynamic Mechanical Analysis of Phase Transformations and Anelastic Relaxation in Stabilized Zirconias" by P.Gao, E. Lara-Cruzio, R. Trejo, and M. Radovic, 2015. *Journal of the Electrochemical Society*, 162, F14-F22, Copyright [2015] by Journal of the Electrochemical Society.

3.2 Introduction

Stabilized zirconias are conventional and commercially available electrolyte materials for Solid Oxide Fuel Cells (SOFCs) with high ionic conductivity and good stability at elevated operating temperatures. To reach high ionic conductivity, doped zirconias as well as other binary oxides, are mainly engineered by optimizing the concentration of oxygen vacancies as the main charge carriers in this class of solid state ionics [75]. The common way to manipulate carrier concentration is by controlling the quantity of doped aliovalent impurities, whose addition also introduce oxygen vacancies to maintain charge neutrality as shown in Equation 3.1 using Kroger-Vink nomenclature [45]

$$R_2O_3 \xrightarrow{ZrO_2} 2R'_{Zr} + V_O^{\bullet\bullet} + 3O_O^x \quad \text{(3.1)}$$

where R represents the doping aliovalent cation, commonly Y^{3+} or Sc^{3+} in ZrO_2.

Doping with 8 – 10 mol% Y_2O_3 or 10 mol% Sc_2O_3, 1 mol% CeO_2 in host ZrO_2 lattice results not only in high ionic conductivity but also in the stabilization of the high-temperature fluorite structure down to room temperature. Y_2O_3 stabilized ZrO_2 (YSZ) and Sc_2O_3, CeO_2 stabilized ZrO_2 (SCSZ) have been subjected to numerous investigations of their chemical stability, transport and electrochemical properties [22, 43, 56, 113]. At high temperatures (above 600 °C), the directional migration of free oxygen vacancies generated by doping leads to good ionic conductivity in doped zirconias [17, 43]. However, at lower temperatures, oxygen vacancies are trapped by aliovalent dopants whose radius is larger than that of the Zr^{4+} host, mainly to minimize the lattice strain, and probably also due to electrostatic attractive force between

oppositely charged dopants and oxygen vacancies [15, 18, 22]. In dilute solutions, a predominately simple type of complexes $(R'_{Zr}V_O^{\bullet\bullet})^{\bullet}$ forms as a result of dopant-oxygen vacancy association, as illustrated in Figure 3.1. $(R'_{Zr}V_O^{\bullet\bullet})^{\bullet}$ complexes are also electric dipoles with associated partial separation of effective charges between dopant and oxygen vacancy [71]. Upon applying an external electric field, these electrical dipoles reorient with electrical field by oxygen vacancies hopping around dopants. This reversible, temperature, time and frequency dependent process of dielectric dipoles reorientation as a dielectric relaxation mechanism was first proposed by Breckenridge et al. [61]. Komine et al. [17] found that the activation energy for this type of dielectric relaxation in 8YSZ single crystal is around 1.22 eV below 600 °C, using impedance analysis in the 40 Hz – 10 MHz frequency and 227 – 827 °C temperature range. With increasing dopant concentration, other more complex oxygen vacancy-dopant complexes, such as $(2R'_{Zr}V_O^{\bullet\bullet})^{x}$, and/or local ordering of oxygen vacancies generated by doping may appear [106, 157]. Dielectric relaxation mechanisms in doped zirconias and other binary oxides has been under study and discussion for a long period of time, as they are related closely to transport properties that are critical for solid state ionic electrolyte materials [17, 158-160].

However, it has been proposed that not only electric field, but also external stress can realign $(R'_{Zr}V_O^{\bullet\bullet})^{\bullet}$ complexes to minimize lattice strain. Therefore, $(R'_{Zr}V_O^{\bullet\bullet})^{\bullet}$ complexes represent at the same time, not only electrical dipoles, but also elastic dipoles. Wachtman et al. [62] used an eight-position model to explain the relaxation process by oxygen vacancy hopping around the dopant, Figure 3.1. Eight nearest neighbor oxygen

positions around the dopant have the same possibility of being occupied by the oxygen vacancy initially. However, under applied stress, the hopping of the oxygen vacancy around the dopant to one of the eight positions becomes preferential as it minimizes total strain energy of the lattice. This process is usually referred to as anelastic relaxation and results in the increased mechanical loss (damping) or internal friction. Nowick et al. [60] and Weller et al. [63] concluded that this type of anelastic relaxation is related to lower trigonal symmetry of defects compared with the host lattice.

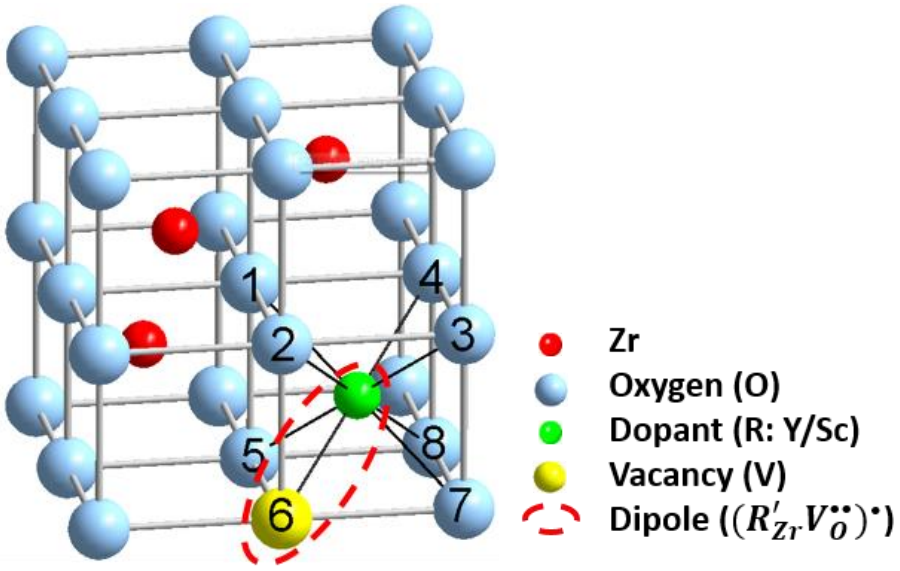

Figure 3.1. Schematic of ZrO_2 fluorite structure with dopant (R: Y/Sc) and eight equivalent nearest neighbor positions around the oxygen vacancy.

Several different experimental techniques were used to study anelastic relaxation in YSZ. To our best knowledge, only two studies reported on anelastic relaxation in scandia doped zirconias. And significantly smaller number of studies have been published on the effects of anelastic relaxation and phase transformations on other physical and mechanical properties of doped zirconias, although those properties are also vital for the structural stability, reliability and durability of electrolyte materials in SOFC [86, 87]. For example, Kushi et al. [55] showed that an abnormally large drop of elastic modulus (so called elastic anomaly) occurs in the same temperature range where anelastic relaxation peaks were observed in both YSZ and SCSZ. However, they suggested that a phase transformation is the primary reason for the intense drop of elastic modulus, not anelastic relaxation, in both YSZ and SCSZ [55]. In a previous study, Radovic et al. [83], showed that not only elastic modulus, but also fracture toughness of 8YSZ shows an obvious nonlinear change with temperature with the minimum value around 600 °C, i.e. roughly at the same temperature at which the maximum in anelastic relaxation was observed. Orlovskaya et al. [161] found minimum values of elastic modulus and fracture toughness in SCSZ at approximately 500 °C, which is close to the operation temperature of this electrolyte material in SOFCs, and attributed this to the reversible cubic→rhombohedral→cubic phase transformation in the 300 – 500 °C temperature range.

In this study, Dynamic Mechanical Analyzer (DMA) is used to study changes of elastic modulus and mechanical damping with temperature and frequency in 8 mol% and 10 mol% Yttria stabilized Zirconia (8YSZ and 10YSZ, respectively) and 10 mol%

Scandia and 1 mol% Ceria stabilized Zirconia (SCSZ) in air. The advantage of DMA, when compared to other methods used to obtain mechanical loss spectra of doped zircoinas in the past, lies in the highly automatic, simultaneous measurement of real part (storage) and imaginary part (loss) of elastic modulus in the wide frequency (10^{-6} to 200 Hz) and temperature (-150 °C to 600 °C) ranges [162-164]. Therefore, the effects of anelastic relaxation and/or phase transformations on the mechanical properties of doped zirconia can be observed and analyzed directly using DMA technique.

3.3 Experimental Methods

8YSZ, 10YSZ and SCSZ samples in this study were processed from the commercially available powders introduced in Section 2.3 Commercial powder was first Cold Pressed (CPed) in 80 x 8 x 8 mm^3 samples using uniaxial press at 20 MPa for 10 seconds, and then Cold Isostatically Pressed (CIPed) at 200 MPa for 20 minutes. After that, green samples were sintered at 1500 °C for 2 hours with 5 °C/min heating and cooling rate. Samples were cut into 50 x 5 x 0.8 mm^3 bars and polished on both sides for DMA tests.

Densities of all samples were measured using Archimedes' principle according to modified standard procedure C20-00 [132] as described in Section 2.3 and elsewhere [165]. The relative densities of all samples were higher than 98%. All test methods and results of structural characterization of the samples, including XRD, optical microscopy and FE-SEM, were shown in Section 2.

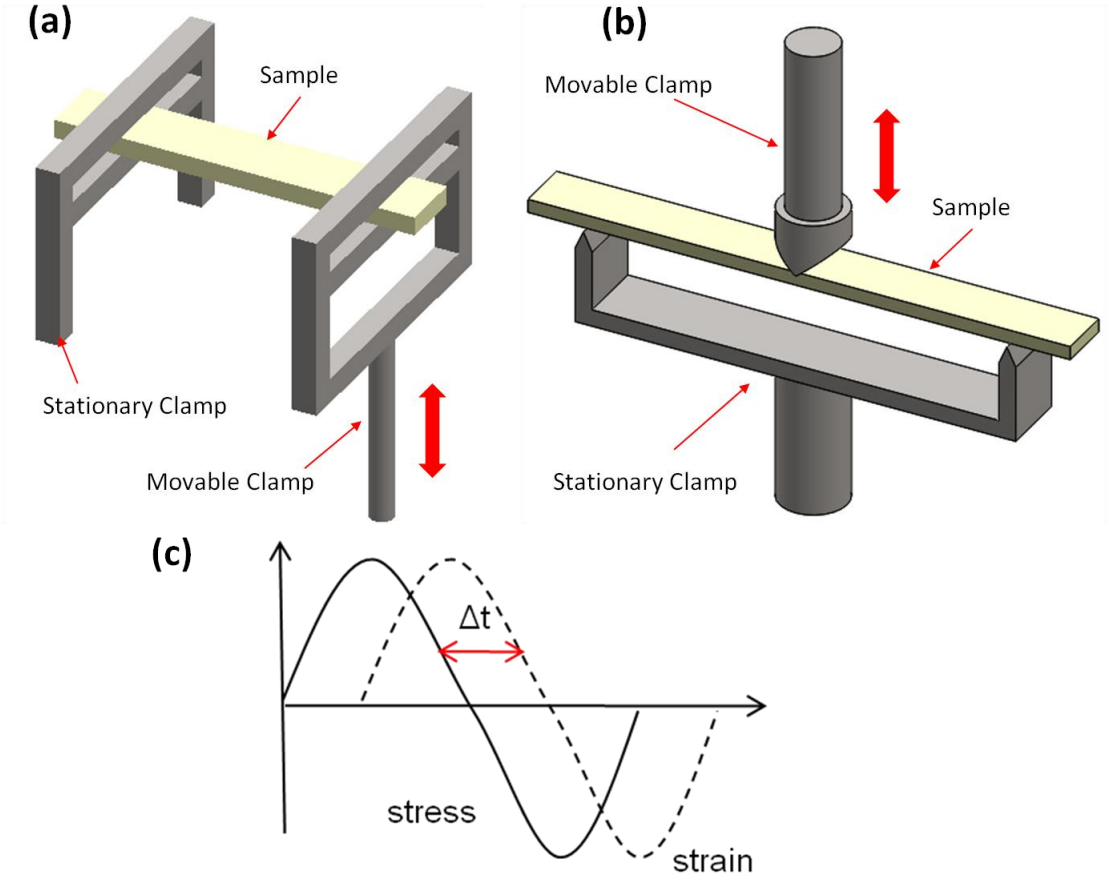

Figure 3.2. Schematic diagram of (a) single cantilever in Q800, (b) three point bending in RSA III and (c) phase delay between applied sinusoidal stress and resultant sinusoidal strain.

To ensure reproducibility of the results and reduce potential influence of equipment and experimental setups on the experimental results, different models of Dynamic Mechanical Analyzers (DMAs) and different clamps were used such as Q800 (TA instruments, IL, USA) with single cantilever clamp and RSA III (TA instrument, IL, USA) with three point bending clamp in air. Figure 3.2 shows the schematic diagram of single cantilever in Q800 and three point bending in RSA III. Sinusoidal stress was

applied on the sample, while responding strain signal and phase lag (δ) between stress and strain was detected. The lengths of clamps were 17.5 mm and 40 mm for single cantilever and three point bending setups, respectively. Two or three samples were tested at the same conditions to ensure repeatability of the results. Samples were tested under constant amplitude strain of 0.0036% in Q800 and 0.01% in RSA III, in the 30 °C to 600 °C temperature range with 5 °C step, at various frequencies (0.1 Hz, 0.5 Hz, 1 Hz, 5 Hz, 10 Hz, 50 Hz, and 80 Hz/100 Hz). Amplitude strains in both Q800 and RSA III were chosen as high as possible to obtain a large mechanical damping peak, but to avoid cracking and failure of the samples.

DMA results were analyzed using procedure described below. For dynamic loading conditions in DMA, strain (ε) and stress (σ) could be expressed as following:

$$\varepsilon = \varepsilon_0 \sin(\omega t) \quad (3.2)$$

$$\sigma = \sigma_0 \sin(\omega t + \delta) \quad (3.3)$$

where $\omega = 2\pi f$ is angular frequency, f is frequency of strain oscillation, t is time and δ is the phase lag between stress and strain. For viscoelastic materials, the elastic modulus can be expressed as:

$$E = E' + iE'' \quad (3.4)$$

where storage modulus (E') is the measure of stored energy of the material, while the loss modulus (E'') is the measure of dissipated energy. E' and E'' can also be expressed as a function of phase lag (δ) as follows:

$$E' = \frac{\sigma_0}{\varepsilon_0}\cos\delta \text{ and } E'' = \frac{\sigma_0}{\varepsilon_0}\sin\delta \quad (3.5)$$

Finally, mechanical damping, or internal friction is defined as:

$$\tan\delta = \frac{E''}{E'} \quad \text{..... (3.6)}$$

Mechanical loss or damping during anelastic relaxation represents energy dissipated during mechanical vibration due to the movement of defects [60], in very similar way as dielectric loss is caused by reorientation of dipoles with alternating electric field. The frequency dependent mechanical loss from Equation 3.6 can be described by the Debye model as: $\tan\delta = \Delta\omega\tau/(1+\omega^2\tau^2)$ where Δ and τ are relaxation strength and relaxation time, respectively. At the maximum internal friction (Debye peak), $\tan\delta_{max} = \Delta/2$ and $\omega\tau = 1$, and thus for a known internal friction peak frequency it is possible to calculate relaxation time τ for every relaxation mechanism [74, 166, 167], exactly like in dielectric spectroscopy but without the effects of contributions from free charges to the relaxation spectrum [168]. In the case of thermally activated relaxation mechanisms, relaxation rate can be expressed as:

$$\tau^{-1} = \tau_\infty^{-1}\exp(-\frac{H_r}{kT}) \quad \text{..... (3.7)}$$

where H_r is the activation energy of the relaxation process [167], τ_∞^{-1} is related to atomic jump rates inherent to the specific relaxation mechanism; k is Boltzmann constant; T is temperature in Kelvin. Thus, to calculate activation energy according to Equation 3.7, anelastic relaxation needs to be tested at different frequencies (f) as a function of temperature since $f = \tau^{-1}$. Activation energy can be then calculated from the slope of lnf vs. 1/T (Arrhenius plot).

3.4 Results and Discussion

3.4.1 Mechanical Damping of 8YSZ and 10YSZ

Figure 3.3 shows DMA results for 8YSZ that were obtained using the single cantilever setup in Q800. Similar results were obtained using the three point bending setup in RSAIII (not shown here) as it is discussed in more details later in this Chapter. Unlike in other traditional oxides, such as Al_2O_3 where elastic modulus decrease almost linearly with increasing temperature [169], in 8YSZ, storage modulus shows significant drop of approximately 37% in the narrow temperature range from room temperature (~175 GPa) to 400 °C (~110 GPa), Figure 3.3a. Two maxima in loss modulus can be observed in the same temperature range (between 30 °C and 400 °C) in Figure 3.3a. Both, storage and loss modulus are frequency dependent in this temperature range. Above 400°C the storage modulus stays almost constant until 600 °C. To clearly observe the relationship between the changes in storage modulus and mechanical damping with temperature, dE'/dT and mechanical damping (tanδ) vs. temperature are plotted in Figure 3.3b. Figure 3.3b shows that the minima in the dE'/dT vs. temperature plots correspond clearly to the maxima in the tanδ vs. temperature plots at all frequencies, suggesting that the abnormal drop in storage modulus is caused by mechanical damping (loss), similar to what is observed in typical viscoelastic materials. In addition, two mechanical damping peaks shift to higher temperatures with increasing frequency, as expected for a typical viscoelastic material. The first mechanical damping peak (further referred to as Peak 1) is in the 25 °C to 200 °C temperature range; while the other peak (further referred as Peak 2) is in the 200 °C to 500 °C temperature range.

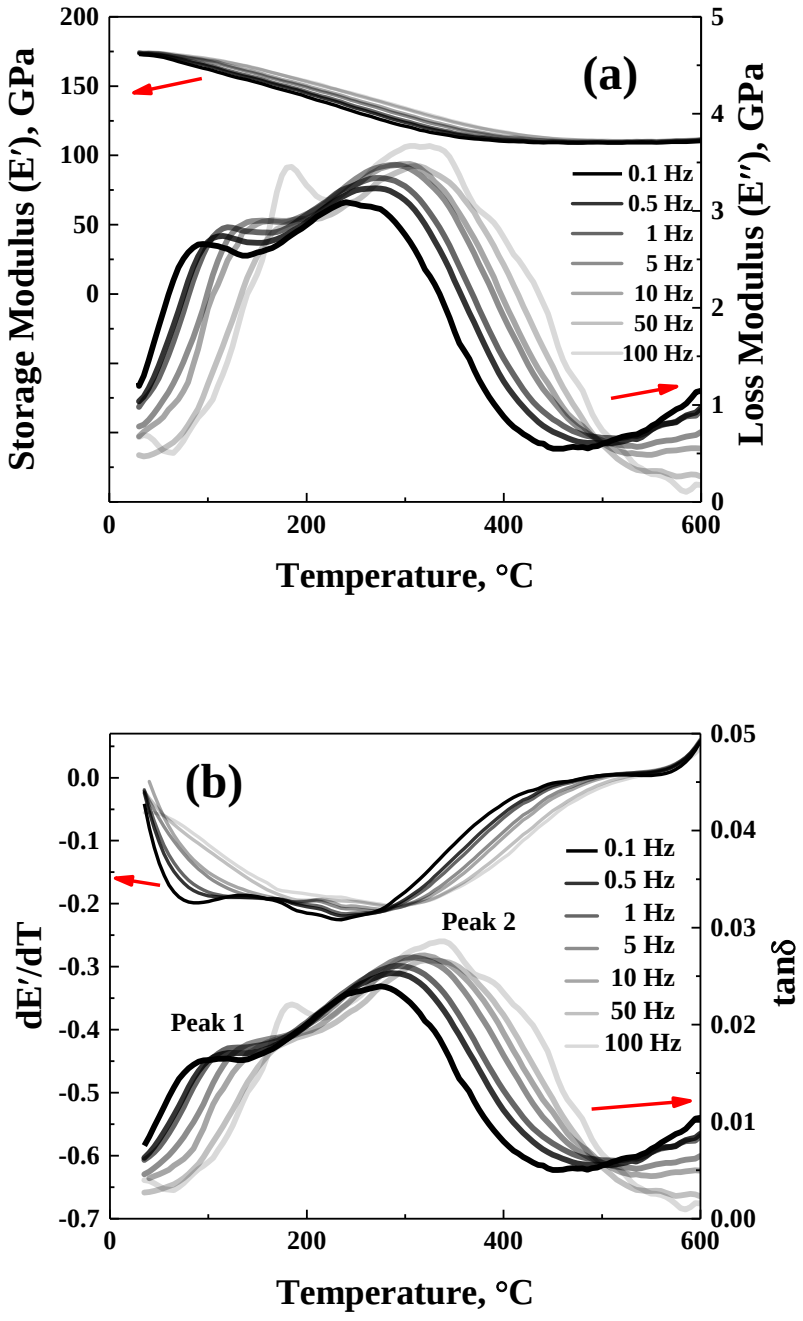

Figure 3.3. (a) Storage modulus (E′) and loss modulus (E″), as well as (b) dE′/dT and tanδ vs. temperature plots for 8 mol% YSZ.

Kushi et al. [55] previously suggested that the drastic drop in elastic modulus can be attributed to the phase transformation from tetragonal to cubic since 8 mol% YSZ is on the edge between cubic and tetragonal regions in phase diagram. However, relationship between the frequency dependent change of dE'/dT and tanδ in Figure 3.3b, suggests that the drop of the storage modulus from room temperature to approximately 400 °C in 8YSZ is caused by the same mechanism as mechanical damping. Even more importantly, frequency dependent changes in elastic moduli and mechanical damping almost exclusively rule out any first order phase transformation as a reason for observed drop in elastic moduli [166].

To further elucidate mechanisms responsible for observed mechanical damping, the damping peaks in 8YSZ were decomposed to two peaks assuming single Debye relaxation model for all three samples tested in Q800 and RSA III. Frequency and temperature of each deconvoluted peak were recorded and plotted in the Arrhenius type plot (lnf vs. 1/T) in Figure 3.4. Activation energies of the two peaks shown in Table 3.1 were calculated from the slope of the best-fitted lines in Figure 3.4, according to Equation 3.7. Results in Table 3.1 and Figure 3.4 show good reproducibility of the results obtained using different experimental setups. More importantly, these results demonstrate clearly that the first damping peak (peak 1) is caused by anelastic relaxation of $(Y'_{Zr}V_O^{\bullet\bullet})^{\bullet}$ elastic dipoles because:

(1) Mechanical loss peaks shift to higher temperature and have higher intensity ($\tan\delta_{max} = \Delta/2$, here $\tan\delta_{max}$ is mechanical damping when $\omega \cdot \tau = 1$, Δ is

relaxation strength) with increasing frequency, which indicates the process responsible for damping peak 1 is thermally activated [68].

(2) Average activation energy for three samples was found to be 1.28 eV, which is in good agreement with Weller's results [68] from torsion pendulum tests showing that activation energy for $(Y'_{Zr}V_O^{\bullet\bullet})^{\bullet}$ dipole reorientation is 1.4±0.2 eV.

(3) Comparable activation energy of 1.22 eV [17] for reorientation of electric dipole $(Y'_{Zr}V_O^{\bullet\bullet})^{\bullet}$ was obtained from dielectric tests, as in this study.

Table 3.1. Comparison of activation energies (H_r) for Peak 1 and Peak 2 in the tanδ vs. temperature plots for 8YSZ (Figure 3.3) and 10YSZ (Figure 3.5).

	Peak 1	**Peak 2**
8YSZ	**H_r, eV**	**H_r, eV**
Sample 1 (Q800)	1.31	2.50
Sample 2 (RSA III)	1.20	2.76
Sample 3 (RSA III)	1.34	2.74
	Peak 1	**Peak 2**
10YSZ	**H_r, eV**	**H_r, eV**
Sample 1 (Q800)	1.41	2.61
Sample 2 (RSA III)	1.48	2.77

As discussed in the introduction of this chapter in more details, previous studies [10, 58, 68] attributed the second relaxation peak (peak 2 in Figure 3.3 and 3.4) either to anelastic relaxation of $(2Y'_{Zr}V_O^{\bullet\bullet})^x$ complexes or to the local ordering of oxygen

vacancies. To elucidate the mechanism responsible for the second relaxation peak, 10 mol% YSZ was tested by DMA and results are shown in Figure 3.5 (test conditions were the same as for 8YSZ samples in Figure 3.3). Similar trends in storage modulus and loss modulus changes with temperature and frequency can be observed in Figure 3.5 as in the case of 8YSZ shown in Figure 3.3. dE′/dT and mechanical damping (tanδ) vs. temperature plots in Figure 3.5b also reveal two frequency dependent local minima in dE′/dT plot that coincide with maxima in mechanical damping.

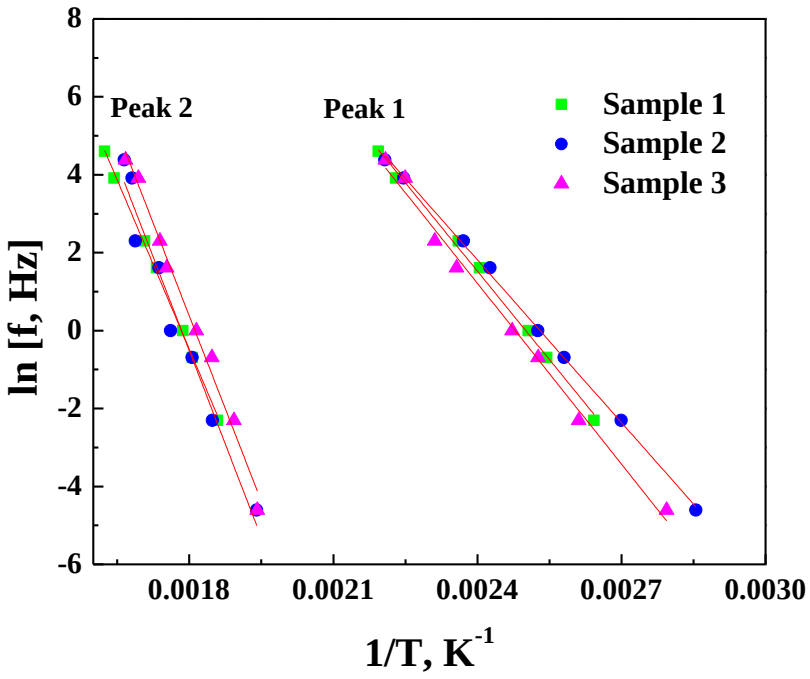

Figure 3.4. Arrhenius plot for Peak 1 and Peak 2 from the tanδ vs. temperature plots for 8YSZ (Figure 3.3).

Mechanical damping curves of 10YSZ were decomposed in the same way as it was done in the case of 8YSZ using single Debye model. Average activation energy of 1.45 eV for peak 1 and 2.69 eV for peak 2 were determined from the Arrhenius type plot (lnf vs. 1/T) for 10YSZ (not shown here), listed in Table 3.1. Selected, but typical mechanical loss vs. temperature plots for 8YSZ and 10YSZ at 0.1 Hz were compared in Figure 3.6. It was observed earlier by Kondoh et al. [58], the temperature of Peak 1 and its intensity do not change significantly by additional doping. However, when compared to 8YSZ, the intensity of the second mechanical loss peak shows a large drop and its position shifts to lower temperature in 10YSZ. This change is similar to what was previously observed in annealed (aged) 8YSZ and was attributed to the local ordering of oxygen vacancies. In addition, the activation energy for both mechanical loss peaks are slightly larger than in 8YSZ (Table 3.1) suggesting that there is a slightly higher energy barrier for thermally activated oxygen vacancies hopping in 10YSZ than in 8YSZ. The latter is not surprising, if ordering of oxygen vacancies in micro-domains is more pronounced in 10YSZ than in 8YSZ. Finally, the activation energies for the second relaxation peaks in 8YSZ and 10YSZ listed in Table 3.1, match very well with the values published by Weller at al. [68] of 2.7±0.2 eV for the second peak in polycrystalline 8YSZ, but they are larger than activation energy of 2 eV that was associated with anelastic relaxation of $(2Y'_{Zr}V_O^{\bullet\bullet})^x$ observed in single crystal YSZ [68].

Nevertheless, the results of this study cannot completely rule out the possible contribution of anelastic relaxation of more complex oxygen vacancy-dopant clusters such as $(2Y'_{Zr}V_O^{\bullet\bullet})^x$ that was first proposed by Nowick et al. [71] as the relaxation

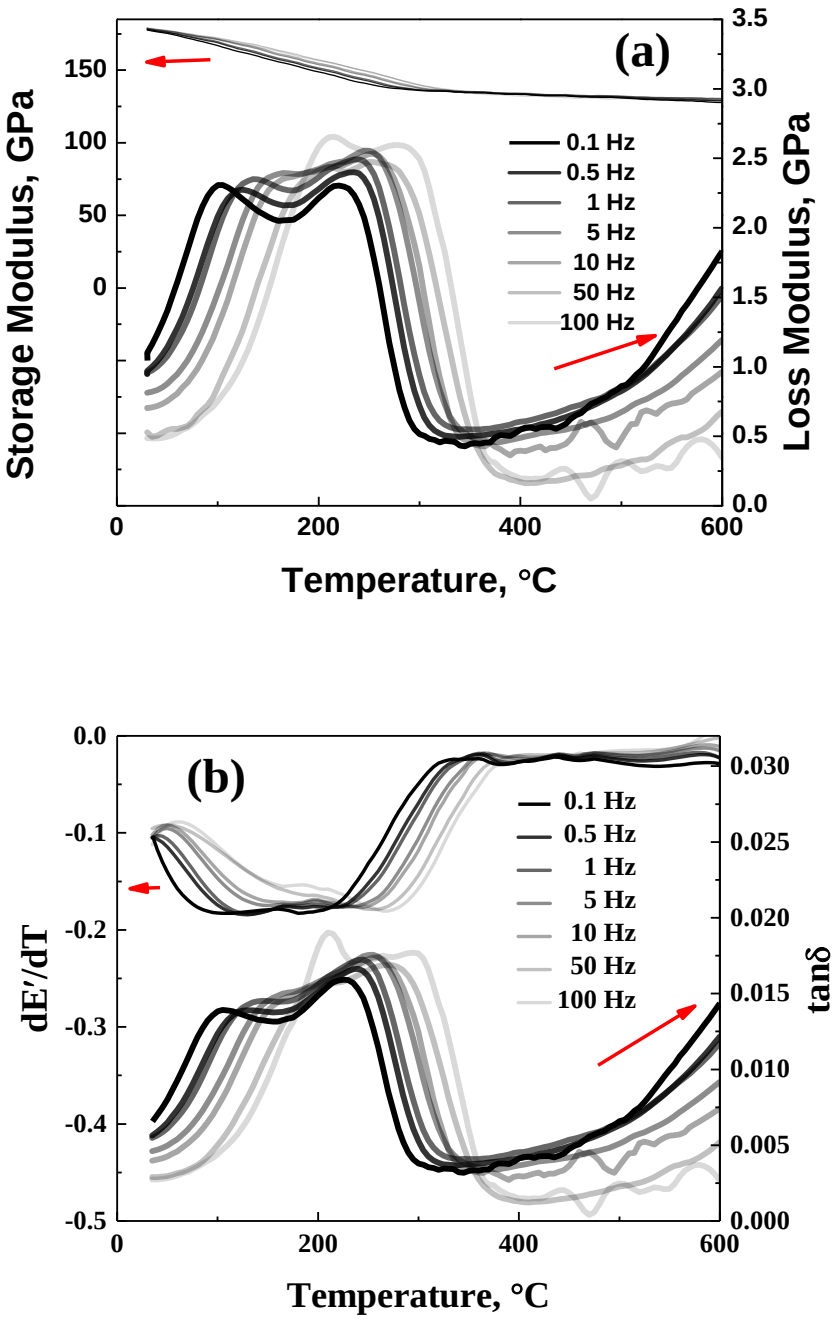

Figure 3.5. (a) Storage modulus (E′) and loss modulus (E″), as well as (b) dE′/dT and tanδ vs. temperature plots for 10 mol% YSZ.

mechanism responsible for the second mechanical loss peak in Y_2O_3 doped CeO_2, and later by Weller et al. [70] in single crystal YSZ. Reorientation of $(2Y'_{Zr}V_O^{\bullet\bullet})^x$ complexes may not be the primary reason for the second mechanical loss peak, but it could still contribute to the second relaxation peak.

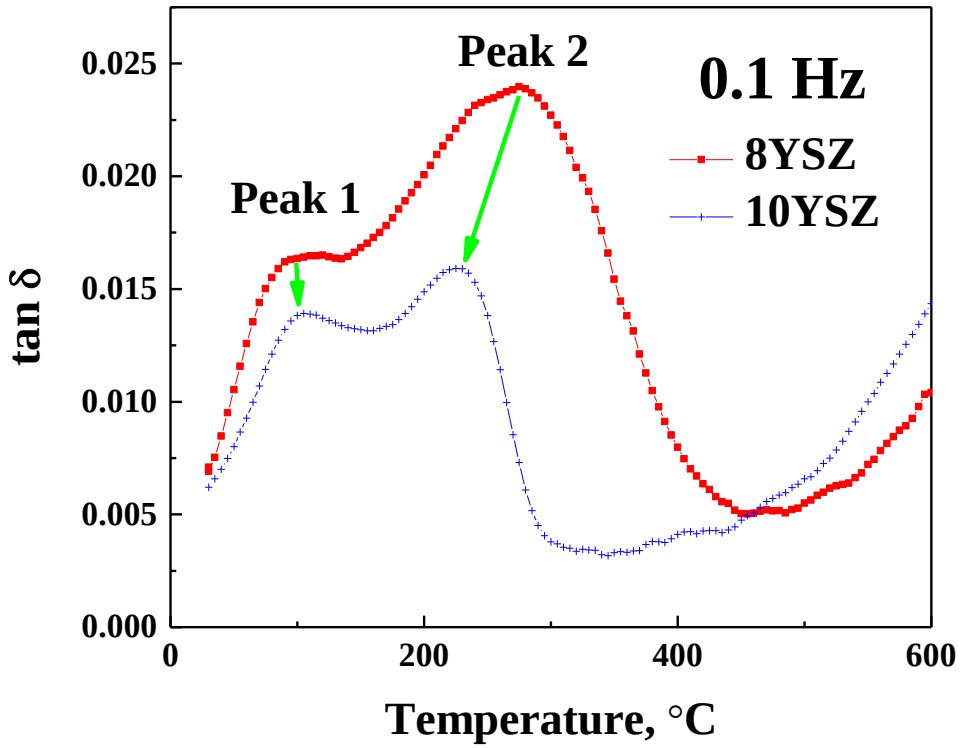

Figure 3.6. Comparison of mechanical loss in 8YSZ and 10YSZ at 0.1 Hz with all other test conditions being the same.

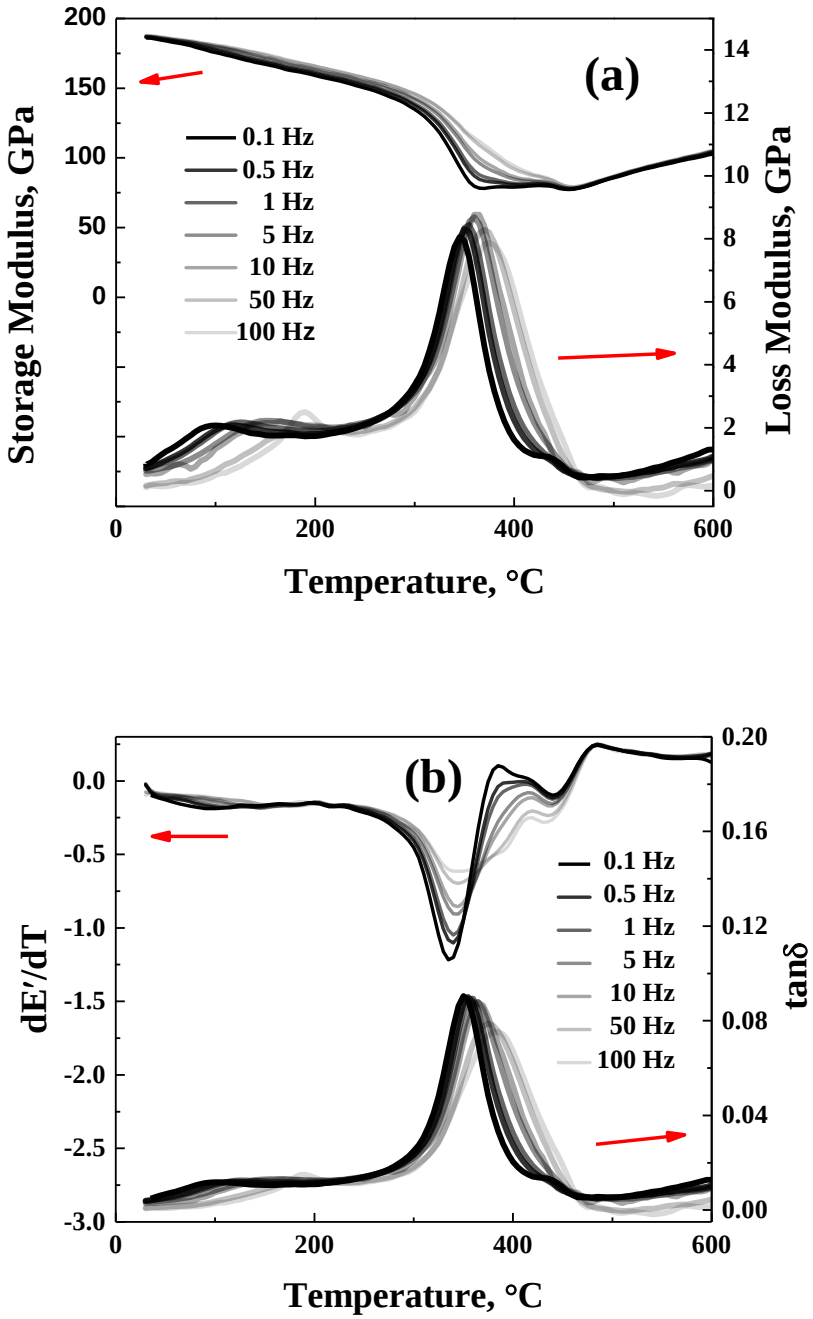

Figure 3.7. (a) Storage modulus (E′) and loss modulus (E″), as well as (b) dE′/dT and tanδ vs. temperature plots for 100% cubic SCSZ.

3.4.2 Mechanical Damping of SCSZ

Figure 7a shows the typical changes of storage and loss moduli with temperature for SCSZ with the stabilized cubic structure at room temperature, as determined using DMA instrument Q800 at different frequencies. Similar to DMA results for 8YSZ and 10YSZ shown in Figure 3.3 and 3.5, storage modulus of SCSZ drops between room temperature and 300 ^{o}C, Figure 3.7a. However, unlike in 8YSZ and 10YSZ, more significant drop in storage modulus from ~140 GPa to ~75 GPa can be observed in the 300 – 450 °C temperature range in SCSZ. Above 450 °C, storage modulus even slightly increases with increasing temperature. dE'/dT and tanδ vs. temperature plots in Figure 7b, clearly show that the storage modulus change in the 30 °C to 200 °C and 300 °C to 400 °C temperature ranges are frequency dependent. The storage modulus at approximately 445 °C seems to be frequency independent, as well as corresponding changes in tanδ.

Internal friction peaks of SCSZ were deconvoluted to four peaks as illustrated in Figure 3.8 for two selected but typical frequencies (0.1 Hz and 100 Hz as example), using the same procedure that described previously in the case of YSZ. Figure 3.8 clearly shows that peak 1 and peak 3 are frequency dependent, as their positions shift to higher temperatures with increasing frequency, while the position of the Peak 4 is frequency independent.

It should be noted that existence of Peak 2 cannot be observed directly in the original data obtained from DMA measurements. However, deconvolution without assuming existence of this peak (not shown here) leads to very poor matching with

experimental results. Therefore, we can assume that since intensity of peak 2 is small, it is most likely covered by the shoulders of peak 1 and, especially, the large peak 3 in the original data collected by DMA. Since the existence of peak 2 cannot be confirmed with the high level of certainty at this moment, it will not be discussed further in this chapter. However it is worth noting that if this relaxation peak exists, it could be associated with local ordering of oxygen vacancies and/or anelastic relaxation of $(2R'_{Zr}V_O^{\bullet\bullet})^x$ dipole, as in the case of YSZ.

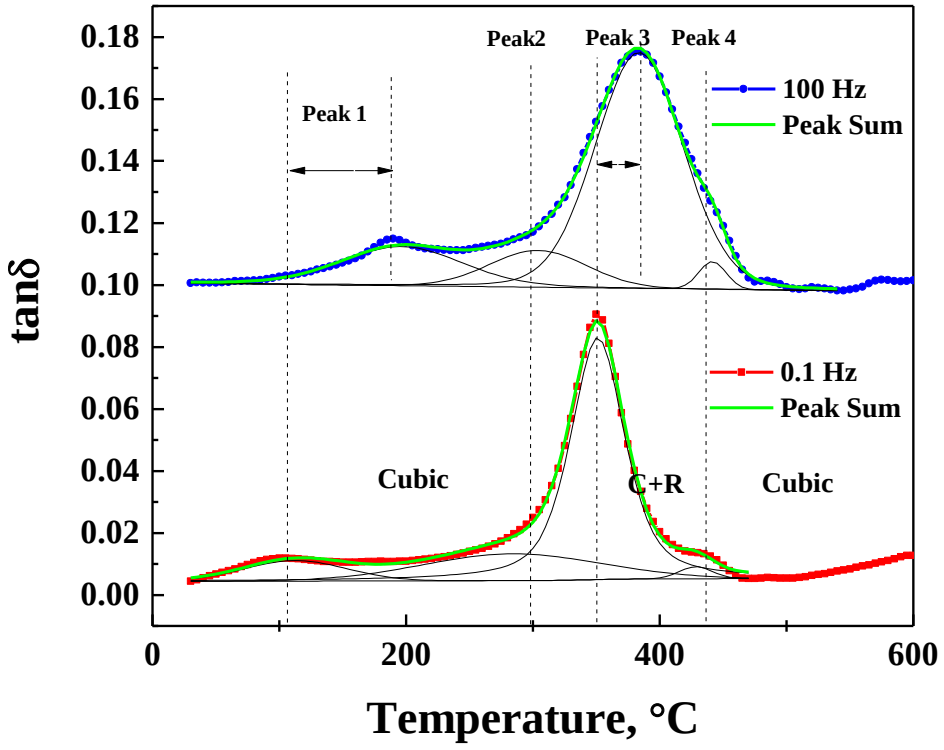

Figure 3.8. Decomposition of tanδ vs. temperature plot for cubic SCSZ to four peaks at two different frequencies (0.1 Hz and 100 Hz).

The activation energies for peak 1 and peak 3 were calculated from the slope of lnf vs. 1/T Arrhenius type plots in Figure 3.9 and they are listed in Table 3.2. Three different samples (Samples 1 – 3) were tested by two different DMA instruments as they are indicated in Table 3.2.

Table 3.2. Comparison of activation energies (H_r) for Peak 1 and Peak 3 in the tanδ vs. temperature plots for cubic SCSZ structure (Figure 3.7) and cubic + rhombohedral SCSZ structure (Figure 3.11).

Cubic SCSZ	**Peak 1**	**Peak 3**
	H_r, eV	**H_r, eV**
Sample 1 (Q800)	1.29	7.97
Sample 2 (RSAⅢ)	1.22	6.56
Sample 3 (RSAⅢ)	1.22	6.97
Cubic + Rhombohedral SCSZ	**Peak 1**	**Peak 3**
	H_r, eV	**H_r, eV**
Sample 1 (Q800)	0.95	8.05

The average value of the activation energies for thermally activated relaxation peak 1 was found to be 1.24 eV (Table 3.2), and thus slightly smaller than that for the first relaxation peak in YSZs (Table 3.1). Since the first damping peak in SCSZ is also frequency-dependent with the activation energy similar to that associated with the reorientation of $(Y'_{Zr}V_O^{\bullet\bullet})^{\bullet}$ dipole in YSZ, it is reasonable to assume that the relaxation peak 1 in SCSZ is caused by anelastic relaxation of $(Sc'_{Zr}V_O^{\bullet\bullet})^{\bullet}$ dipole. The smaller

activation energy in SCSZ could be explained by the smaller difference of ionic radii between dopant and host cations in SCSZ than that in YSZ. The larger difference in ionic radii, increases lattice distortion and activation energy of oxygen vacancy hopping around dopant. Since Y^{3+} (101.9 pm) is larger than Sc^{3+} (87 pm), it causes larger lattice strain when it replaces Zr^{4+} (84 pm) host in the crystal structure, that in turn makes oxygen vacancy hopping around dopant more difficulty [43].

For the third frequency dependent mechanical loss peak in SCSZ, activation energies in Table 3.2 from two different experimental setups are different, namely 7.97 eV for single cantilever setup in Q800 and 6.76 eV (average) for bending setup in RSAⅢ. However, both values are significantly larger than activation energies due to anelastic relaxation of dipoles in YSZ (peaks 1 and 2) and SCSZ (peak 1). The relaxation of peak 4 is clearly frequency independent from the results presented in Figures 3.7 – 3.9.

To further elucidate the mechanisms responsible for relaxation peaks 3 and 4 in Figures 3.7 – 3.9, pure cubic phase SCSZ samples were annealed at 350 °C for 100 hours, to stabilize the rhombohedral structure at room temperature. SCSZ was found to show phase transformations during heating at approximately 300 °C from room temperature stable cubic to rhombohedral structure, that transforms back completely to cubic structure at approximately 500 °C [170]. This phase transformation is also proved by authors' high temperature-XRD studies in Section 2 during heating and cooling of SCSZ. However, during annealing at 350 °C for 100 hours the cubic structure did not completely transform to rhombohedral phase in our sample, as it was previously reported

in the literature [170]. After annealing and cooling down to the room temperature, the sample contained 39.05 % cubic phase and 60.95 % rhombohedral phase, as it was determined from XRD, Figure 3.10.

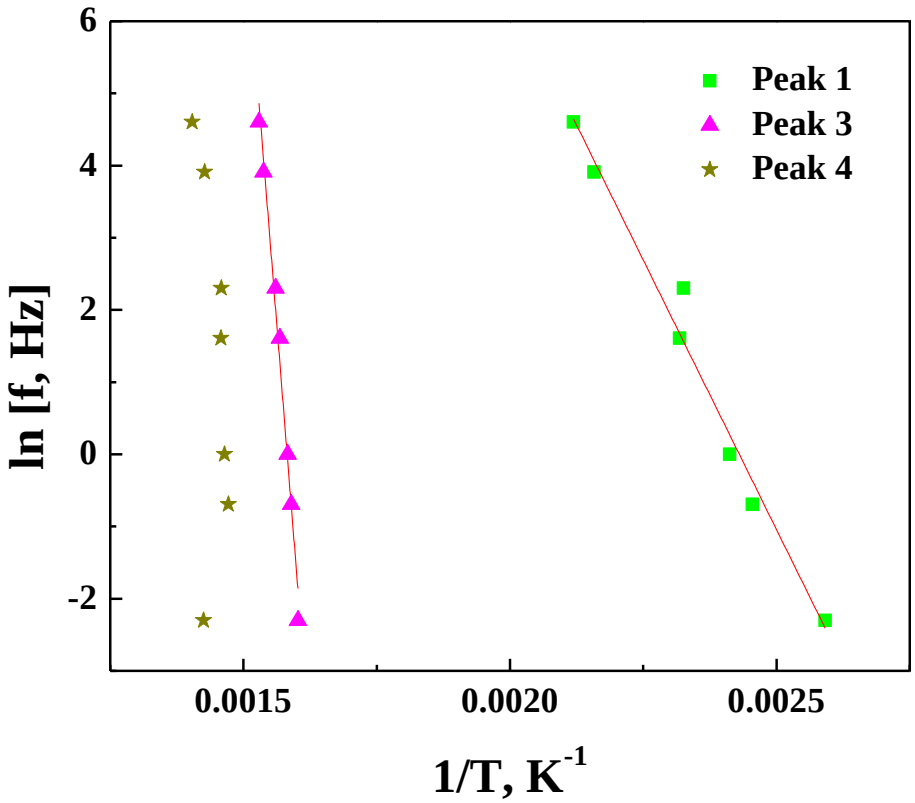

Figure 3.9. Arrhenius plot for Peak 1, Peak 3 and Peak 4 from the tanδ vs. temperature plot for cubic SCSZ (Figure 3.7).

Figure 3.11a summarizes DMA results for annealed SCSZ sample with two-phase (rhomboheral + cubic) structure at room temperature, that were obtained using Q800 while Figure 3.11b shows changes of dE′/dT with temperature together with

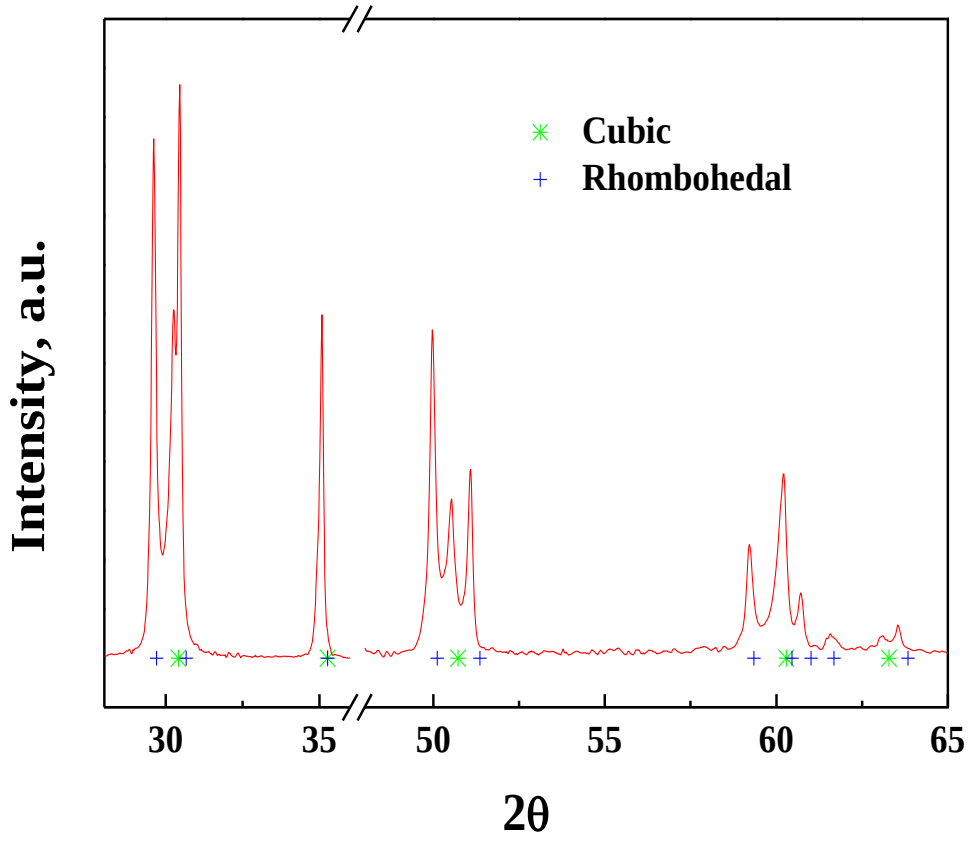

Figure 3.10. XRD result of SCSZ cubic sample annealed at 350°C for 100 hours (60.05% rhombohedral + 39.95% cubic).

internal friction peaks, for different frequencies. Like in purely stabilized cubic SCSZ, the frequency dependent decrease in storage modulus can be observed in the 30 °C to 200 °C and 300°C to 400°C temperature ranges, Figure 3.11. However, a more intense decrease in the storage modulus can be observed between 400 °C and 480 °C when

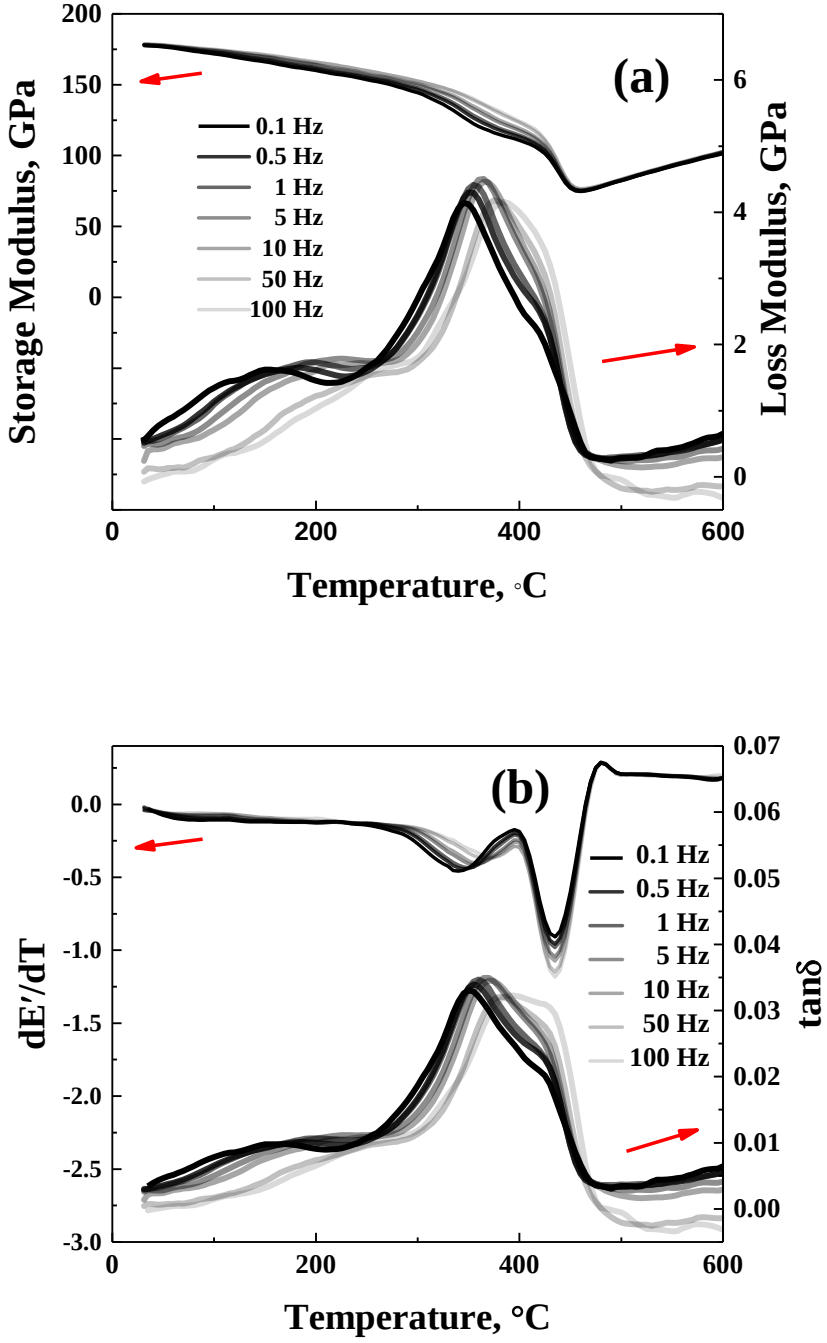

Figure 3.11. (a) Storage modulus (E′) and loss modulus (E″), as well as (b) dE′/dT and tanδ vs. temperature plots for cubic + rhombohedral SCSZ.

compared to cubic SCSZ. The change of storage modulus in this region is also frequency independent and reach local minimum at 445 °C. In addition, the local maxima in tanδ and E'' vs. temperature plot—previously labeled as peak 4 for cubic SCSZ—samples can be observed at 445 °C, Figure 3.11. The fact that the drop of storage modulus around 445 °C is more pronounced in cubic+rhomohedral structure (Figure 3.11) than in pure cubic structure (Figure 3.8), as well as the frequency independence of the mechanical loss peak at that temperature indicate that the phase transformation from rhombohedral to cubic structure is responsible for observed drop in storage modulus and corresponding mechanical loss peak, as this behavior is typical for the first order phase transformation [74, 166]. Figure 3.11 also shows that above 480 °C the storage modulus remains almost constant up to 600 °C, which is the same tendency as observed previously in stabilized cubic SCSZ.

Mechanical loss peaks for annealed SCSZ sample was decomposed to four peaks in the similar way as in the case of cubic SCSZ (Figure 3.8), and two typical examples at different frequencies (0.1 Hz and 100 Hz) are shown in Figure 3.12. Figure 3.12 illustrates clearly that peak 1 and 3 are again frequency dependent, while the temperature of peak 4 does not change with frequencies. Activation energy of peak 1 and peak 3 are calculated from Arrhenius type plots for annealed SCSZ samples (not shown here) and they are also listed in Table 3.2. Activation energy for peak 1 was found to be 0.95 eV, which is smaller than 1.24 eV determined for cubic SCSZ. The reason for this is still unclear. Activation energy for peak 3 (Table 3.2) in the two phases sample (8.05 eV) is comparable to that of cubic SCSZ (7.97 eV), only in the case when both were calculated

from the results obtained using the same DMA apparatus, namely Q800 equipment under identical testing conditions.

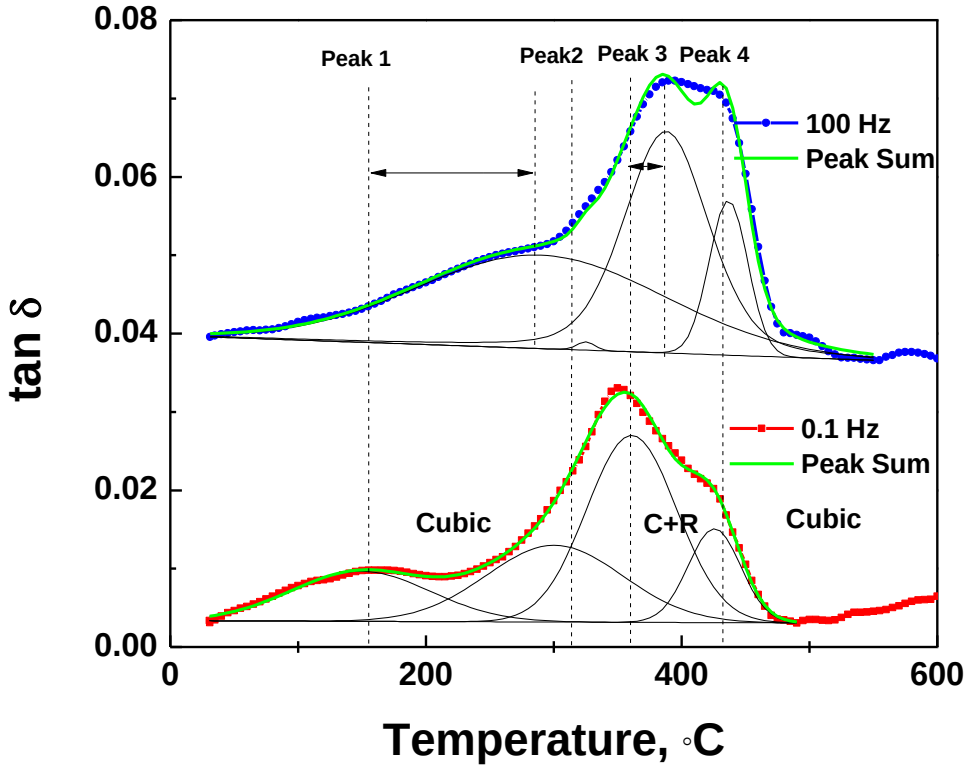

Figure 3.12. Decomposition of tanδ vs. temperature plot for cubic + rhombohedral SCSZ to four peaks at two different frequencies (0.1 Hz and 100 Hz).

Selected but typical mechanical damping vs. temperature plots for samples with pure cubic phase and cubic + rhombohedral structure at room temperature at the same frequency of 0.1 Hz are compared in Figure 3.13. It clearly indicates that the intensity of the third peak drops significantly in the sample with more rhombohedral phase stabilized at room temperature, while intensity of the peak 4 for the same sample increases when

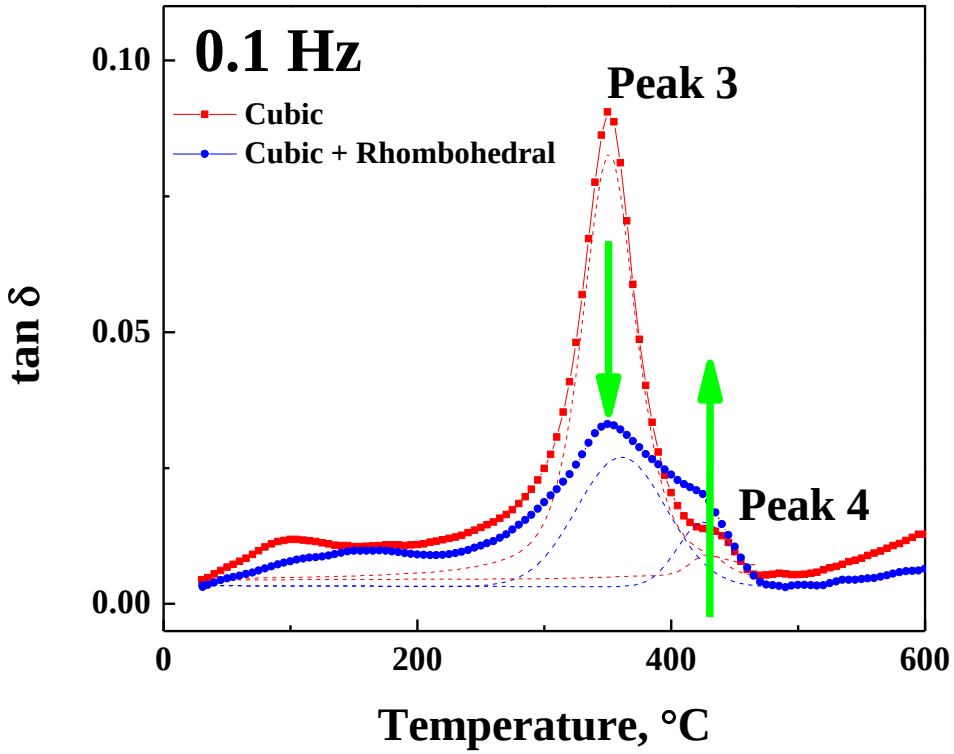

Figure 3.13. Comparison of mechanical damping peaks for cubic single phase SCSZ and cubic + rhombohedral SCSZ at 0.1 Hz (all other test conditions were the same).

compared to the one with pure cubic structure. All these indicate that peak 3 can be attributed to a phase transformation from rhombohedral to cubic structure, while peak 4 can be attributed to a phase transformation from cubic to rhombohedral structure. Since 60.05 % rhombohedral phase structure has already existed in the two phases sample before DMA test, less cubic to rhombohedral transformation occurred during testing

leading to lower peak intensity of mechanical damping peak 3, but larger intensity of mechanical damping peak 4.

Furthermore, the activation energy associated with peak 3 was determined from the results collected using RSA III at higher amplitude strains/stress is smaller (Table 2), when compared to that determined from the results obtained using Q800 in pure cubic SCSZ samples. In other words, when amplitude strain of 0.01 %, was used in RSA III activation energy of 6.56/6.95 eV was determined for peak 3, while at the amplitude strain of 0.0036 % in Q800 the activation energy associated with that peak was found to be 7.97/8.05 eV. This as well as the fact that peak 3 is frequency dependent suggest that it can be attributed to the stress-induced cubic to rhombohedral phase transformation. Previously, Orlovskaya and coworkers [153] also suggested that cubic to rhombohedral phase transformation around 300 °C in SCSZ could be stress induced.

As for peak 4, results of this study clearly indicate that this peak is associated with the first order rhombohedral to cubic phase transformation since both dE'/dT and mechanical damping peak are frequency independent as it is expected for first order phase transformations [74]. Additional evidence can be also found in that the intensity of this peak is higher for cubic + rhombohedral structure than for pure cubic structure. Finally, the first order rhombohedral to cubic phase transformation has been previously observed around 500 °C in other Scandia doped Zirconia samples with rhombohedral structure at room temperature [74].

3.5 Conclusions

Storage modulus, loss modulus and mechanical loss peaks vs. temperature in 8YSZ, 10YSZ, SCSZ were obtained simultaneously at different frequencies in the 30 – 600 °C temperature range by DMA. A rapid drop in storage modulus (~37%) was observed in YSZ samples in the 30 – 400 °C temperature range while additional sharp drop in storage modulus (from ~140 GPa at 300 °C to ~75 GPa at 450 °C) was observed in SCSZ samples. Analysis of E', E'', dE'/dT, and mechanical damping (tanδ) vs. temperature curves, clearly show that the observed drops in elastic moduli can be attributed to anelastic relaxation of oxygen vacancy-dopant complexes, local ordering of oxygen vacancies and/or phase transformations.

Observed mechanical loss peaks in YSZ samples were de-convoluted to two frequency dependent peaks by assuming single Debye relaxation model. Average activation energy was found to be 1.28 eV for the first relaxation peak in 8YSZ and 1.45 eV in 10YSZ. This matches the activation energy of anelastic or dielectric relaxation due to reorientation of $(Y'_{Zr}V_O^{\bullet\bullet})^{\bullet}$ dipoles. The second damping peak at higher temperature shows activation energy of 2.67 eV in 8YSZ and 2.69 eV in 10YSZ. The mechanism for the second peak is still not completely clear, although results presented here suggest that ordering of oxygen vacancies in micro-domain and anelastic relaxation of $(2Y'_{Zr}V_O^{\bullet\bullet})^{x}$ complexes may contribute to this loss peak.

In the case of as-process and annealed SCSZ with pure cubic and 39.95 % cubic + 60.05 % rhomobohedral structures at room temperatures, respectively, mechanical damping vs. temperature plots were decomposed to four peaks. The first frequency-

dependent peak with average activation energy of 1.24 eV in cubic SCSZ and 0.95 eV in two phases SCSZ is attributed to anelastic relaxation of $(Sc'_{Zr}V_O^{\bullet\bullet})^{\bullet}$ similarly as in YSZ. In cubic SCSZ, the activation energy of this relaxation mechanism is slightly smaller than it in YSZ due to the smaller lattice strains caused by substitution of host cation by Sc^{3+} which has an ionic radius closer to that of Zr^{4+} radius than Y^{3+}. The position of the second peak for SCSZ samples was hard to identify with high level of certainty since it is on the covered by shoulders of first and third peaks. Stress induced phase transformation from cubic to rhombohedral is the reason for the occurrence of the third frequency-dependency peak on mechanical loss vs. temperature curve. Activation energy of this peak was found to be stress dependent, i.e. smaller activation energy was determined from the results of the tests carried out at larger amplitude strain. The first order phase transformation from rhombohedral to cubic lead to the appearance of the fourth frequency independent damping peak in mechanical loss spectra. Comparison of intensities of the third and fourth mechanical loss peaks of cubic and two phases SCSZ, also confirmed that those two peaks are associated with cubic to rhombohedral and rhombohedral to cubic phase transformations.

At high temperature, stabilized zirconias show not only a high modulus, which is comparable to some of conventional ceramics, but also large mechanical damping, which is similar to that of some polymer materials [171]. Good mechanical behaviors of stabilized zirconias make them suitable to endure relative large internal stress by exhibiting high modulus and large mechanical energy dissipation capability in Solid Oxide Fuel Cells at high temperature during heating and cooling cycles. However, the

intense nonlinear drop of modulus in the 300 – 500 °C temperature range needs more attention during fabrication and operation.

4. ANELASTIC RELAXATION AND SPONTANEOUS POLARIZATION OF 8 MOL% Y_2O_3 STABILIZED ZrO_2

4.1 Summary

Doped zirconia ceramics (ZrO_2) are a vivid textbook example of significant improvements that can be achieved in material properties through the careful engineering of point defects [172]. The doping of ZrO_2 with aliovalent cations not only stabilizes the high-temperature cubic structure of ZrO_2 down to the room temperature, but also introduces additional vacancies to the oxygen sublattice. The latter results in the fast directional migration of the oxygen ions in doped zirconia ceramics such as 8 mol% Y_2O_3 Stabilized ZrO_2 (8YSZ) at high temperatures (above 600 °C for 8YSZ), and consequently improvements in its ionic conductivity for several orders of magnitude [16, 17, 173]. Therefore, those materials have been extensively used as solid-state ionic conductors in fuel cells, oxygen sensors, and gas separation membranes [174].

However, our previous research showed that the formation of oxygen vacancies in doped zirconia ceramics and their clustering in vacancy-cation complexes might lead to another interesting phenomena, namely the intense decrease of elastic moduli and large mechanical damping in the 20 °C to 500 °C temperature range [69]. It is believed to be the result of anelastic reorientation of vacancy-cation dipoles and their ordering under stress. In this study, 8YSZ was tested under cyclic compression loading to obtain stress-strain curves from room temperature up to 600 °C. Reproducible closed stress-strain hysteresis loops were observed for the first time in 8YSZ in the 20 °C to 500 °C temperature range due to the reorientation of defect complexes. More importantly, a

stress-induced polarization was also observed in the same temperature region, suggesting that 8YSZ exhibits electro-mechanical coupling similar to that in piezoelectric materials. However, unlike other piezoelectric materials having crystal structures belonging exclusively to one of 20 non-centrosymmetric point groups, 8YSZ has the centrosymmetric cubic structure. Therefore, the results shown here indicate that piezoelectric effect can be achieved in a centrosymmetric system through the introduction of defect clusters with a lower symmetry, as those clusters represent both elastic and electric dipoles. This finding paves the way to the extension of existing piezoelectric materials to those with centrosymmetric structure by engineering their defect structure.

4.2 Introduction

It has been well established by now that the electric conductivity of binary oxides is closely related to the presence, type and mobility of point defect [16, 56, 58, 68]. A noteworthy progress has been realized in the development of solid-state ionics based on binary oxides such as ZrO_2 or CeO_2 with transport properties that are tailored successfully for different applications, predominately through engineering chemistry and the structure of point defects by doping oxides with aliovalent cations (valence two or three) [22, 43, 56, 113]. Thus far, 8 mol% Y_2O_3 stabilized ZrO_2 (8YSZ) has been one of the most commonly used solid state ionics in various applications such as solid oxide fuel cells (SOFCs) and oxygen sensors due to its high ionic conductivity and good structural stability [15, 22, 110, 174]. 8 mol% Y_2O_3 has stabilized cubic fluorite crystal

structure (cubic: $Fm\bar{3}m$), stable stoichiometry (chemistry), and high ionic conductivity, even in harsh operating environments, including high temperatures, external electric fields, mechanical stresses and oxygen potential gradients. The doping of zirconia results in the formation of oxygen vacancies, to balance the charge difference between the doped cation (Y^{3+}) and host cation (Zr^{4+}), as shown in Equation 1 using Kroger-Vink nomenclature [17, 43-45].

$$Y_2O_3 \xrightarrow{ZrO_2} 2Y'_{Zr} + V_O^{\bullet\bullet} + 3O_O^x \quad \text{(4.1)}$$

Oxygen vacancies freely move in dilute solutions at high temperatures (above 600 °C) leading to high ionic conductivity. However, at low temperatures (below 600 °C), oxygen vacancies become trapped by immobile opposite charged cations even in dilute solutions partially due to a strong Columbic attraction between them, but mainly because this clustering minimizes the lattice strain energy [15]. Therefore, a simple type of complexes is formed between oxygen vacancy and dopant cation, i.e. $(Y'_{Zr}V_O^{\bullet\bullet})^{\bullet}$ [10, 46-49]. Another simple complexes, i.e. $(Zr_{Zr}^{x}V_O^{\bullet\bullet})^{\bullet\bullet}$ was found in a number of studies [50-54] using EXAFS to study the local structure of oxygen vacancies as vacancies preferentially around Zr^{4+}.

When increasing the concentration of dopants, more complex dipoles, e.g. $(2Y'_{Zr}V_O^{\bullet\bullet})^{x}$, may appear in the lattice [10, 55]. Meanwhile, with higher dopant concentrations or longer aging time, oxygen vacancies tend to form aggregated clusters (or local-domains), such as $Zr_3Y_4O_{12}$ (rhombohedral structure with space group $R\bar{3}$) [56], fluorite-derivative structure (delta phase) [57] and other similar structures (pyrochlore, bixbyite, zirconolite) [57]. Increasing the concentration of dopants and

aging time, the number and size of aggregates increase [48, 58]. This process is energetically favorable as it minimizes strain energy caused by the difference between ionic radius of dopant (Y^{3+}) and host (Zr^{4+}) ions, usually referred to as the local ordering of oxygen vacancy clusters in the literature [57, 58]. Kondoh et al. [58, 59] indicated that the short range ordering of oxygen vacancies lead to a decrease of ionic conductivity in YSZ with a higher dopant concentration (> 8 mol%) or longer service time.

Significant progress has been achieved in understanding the effect of the distribution, concentration and association/clustering of point defects on its ionic conductivity until now [14, 22, 75]. But the studies addressing the influence of point defect complexes to mechanical behaviors are relatively scarce. However, the intense ~40% drop of elastic modulus at 600 °C from room temperature severely threatens the reliability and durability of 8YSZ during thermal cycling and high temperature services [83]. As reported in the previous studies by RUS in Section 2 and DMA in Section 3 [69], 8YSZ shows two large frequency-dependent mechanical damping peaks in the temperature range of 20 °C to 500 °C together with the abnormal change of elastic moduli. The mechanical damping is quantified by tanδ as:

$$\tan\delta = E''/E' \quad \text{.....(4.2)}$$

where, E' and E'' are two components of elastic modulus E^* ($E^* = E' + iE''$), namely storage modulus and loss modulus, respectively. Therefore, $\tan\delta$ represents the ratio between energy dissipated and stored in each load-unload cycle. The changes of storage modulus and mechanical damping with temperature show two corresponding frequency-dependent peaks around 150 °C and 350 °C, respectively. It indicates that the reasons

leading to the mechanical damping are also responsible for the abnormal change of the storage modulus.

4.3 Experimental Methods

All 8YSZ samples in this study were processed from 8 mol% yttria stabilized zirconia commercial powder (TOSOH Corp., Japan). The powder was first cold uniaxially pressed at 20 MPa for 10 seconds and then cold isotactically pressed at 200 MPa for 20 minutes. After that, green samples were sintered in the furnace in air at 1500 °C for 2 hours with 5 °C/minute heating and cooling rates. The relative densities of all samples were found to be above 98% using modified standard Archimedes procedure C20-00 [132]. The grain sizes of all samples were measured to be around 5 μm from the field emission scanning electron microscopy (FE-SEM; Quanta 600 FEG, FEI, Oregon, USA) images of the thermal etched polished sample surfaces.

Material testing system (MTS, MTS Systems Corporation, MN, USA) was used for the cyclic compression tests, Figure 4.1a. 8YSZ samples were cut to 20 x 10 x 10 mm^3 rectangular blocks and each of them was loaded between two hydraulic pushing heads and held at 5 MPa pre-loading stress (Figure 4.1a). Sinusoidal stress was applied from 10 MPa to 450/550 MPa, and then back to 10 MPa for three cycles with a frequency of 0.1 Hz at the selected temperature steps from 25 °C to 600 °C (25 °C/step in the temperature range of 25 – 200 °C and 450 – 600 °C; 10 °C/step from 200 °C to 450 °C). A highly accurate high temperature extensometer (Model: 632.59, MTS Systems Corporation, MN, USA) was directly attached to the sample to record the

change of strain under the sinusoidal stress. A split tube furnace was used to heat up the sample to the desired temperatures. A K-type thermocouple located very close to the sample was used to control the temperature. The sample was held under preloading for 20 minutes at each temperature before cyclic loading tests to ensure uniform temperature distributing within the sample. Then, cyclic loading was applied at this temperature and strain change was recorded by the extensometer. After that, temperature was increased to the next desired temperature and cyclic loading was applied again. The secant moduli were calculated from the slopes of the stress-strain curves at different temperatures, while the area of the hysteresis loops were used to calculate dissipated energy per load-unload cycle as $W_d = \oint \sigma d\varepsilon$, where σ is the stress and ε is the strain. To verify the repeatability of the test, different powder batches and multiple samples were used. Also, alumina (Al_2O_3) was tested at the same conditions as a control material and compared with 8YSZ.

In this study, in-situ neutron diffraction was equipped with uniaxial compression MTS load frame and induction furnace performed at VULCAN engineering materials diffractometer beamline at Spallation Neutron Source (SNS), Oak Ridge National Laboratory (ORNL). Diffraction pattern with a bandwidth of 0.5 – 3.5 Å was obtained using a chopper at 20 Hz frequency. Two detectors at $2\theta \pm 90°$ (bank 1 and bank 2) collected neutron diffractions patterns parallel and perpendicular to the loading directions from different crystal planes (hkl) [175]. An incident slit of 4 mm width and 3 mm height, with a pair of 5 mm radial collimators providing a 60 mm^3 gauge volume was used. Figure 4.2a shows the photo of the sample setup. Cylindrical 8YSZ samples

with the diameter of 10 mm and length of 20 mm were prepared for the test. The sample was placed in the specially machined stainless steel to allow induction heating by copper induction coils. The sample was then horizontally loaded between two alumina-pushing heads with 10 MPa preloading stress. A K-type thermal coupling was inserted inside of the sleeve and close to the sample to control temperature. Before this test, five other K-type thermocouples were spot welded outside of the sleeve evenly from one end to the other to monitor the temperature and confirm its uniform distribution all over the sample. The sample was first tested at room temperature under the stresses of 10 MPa, 150 MPa, 250 MPa, 350 MPa, 450 MPa, 550 MPa during loading and unloading. A similar test was done at 350 °C under the same stresses. The neutron diffraction data was collected at each stress using the high-resolution mode for 80 minutes. The structure refinement was performed using GSAS software [176]. Single peak fitting were processed by VDRIVE software to obtain the stress-lattice strain curves on different crystal planes [177].

For the electro-mechanical coupling tests, the MTS system was used to apply sinusoidal loading in compression, in combination with an oscilloscope to record corresponding open circuit voltage outputs from sample as it is illustrated in Figure 4.5a. Five 8YSZ samples were cut to 7.5 x 7.5 x 1 mm^3 square plates. Two alumina spacers with the dimension of 10 x 10 x 5 mm^3 were sputtered with 5 μm platinum on one side as electrodes. The spacers were also able to insulate the platinum electrodes and conducting sample from the SiC conductive pushing rods in the MTS system. One gold wire connected an electrode to the oscilloscope (DS1102E, RIGOL technologies Inc.,

OR) to measure voltage, while the other grounded gold wire connected the other electrode and grounding oscilloscope. 8YSZ sample was placed between two alumina spacers with the sputtered electrodes on the interface between 8YSZ sample and the spacer, and mounted in the compression loading stage. A nickel cage was placed outside of the sample as an electromagnetic shielding from surrounding electric heating elements. The sample was heated to the desired temperature and then, tested under cyclic loading for 6 load-unload compressive cycles at the loading frequency of 1 Hz under the different amplitudes of sinusoidal stresses ranging from 5 MPa to 650 MPa with the increments of 50 MPa. Voltage outputs from the direction of external stress was monitored and recorded at different temperatures. The amplitude of voltage signals (ΔV) was calculated from the difference of average maximum and minimum in the observed sinusoidal voltage outputs over six load-unload cycles. Al_2O_3 samples were also tested using the same conditions and the same procedures for a comparison.

The polarization (P-E curve) of 8YSZ was measured under different stresses using Sawyer-Tower method illustrated in Figure 4.6a. A constant compressive stress was loaded on the sample by the MTS system. At the same time, an analog triangular electric signal was generated by a signal generator (33220A 20 MHz Waveform Generator, Agilent Technologies, CA) and amplifier (609E-6, TREK Inc., NY) and was applied to the sample. Tests were carried out on a plate sample with the dimension of 5 mm x 5 mm x 0.78 mm when the applied force has the same direction as the electric field. Platinum films were also sputtered on one surface of two alumina spacers and placed in contact with the YSZ sample as in the previous electro-mechanical coupling

test. The two channels of oscilloscope (DS1102E, RIGOL technologies Inc., OR) were connected with the electrodes using gold wires. A capacitor with the capacitance, C_{ref}, of 50 nF was used in series with the sample. The oscilloscope and the wire between the reference capacitor and amplifier connected to the signal generator were grounded. The sample was first heated up to 600 °C, and then cooled down to the desired temperature. After the sample was isothermally kept for 20 minutes at the desired temperature to reach equilibrium, two voltage-time plots, namely V_X-time and V_Y-time, obtained from the two channels of oscilloscope were recorded under several constant compressive stress steps at 5 MPa, 150 MPa, 300 MPa and 450 MPa while simultaneously applying triangular electric signals from -200 V to 200 V. After that, temperature was decreased to next level and the test procedure was repeated. The same procedure was repeated at room temperature, 150 °C, 300 °C, and 450 °C.

Applied voltage (V_{app}) generated by signal generator and amplifier at the frequency of 1 Hz was recorded by the X-terminal of the oscilloscope (V_X), and applied to the reference capacitor (V_{ref}) and sample (V) in series, i.e. $V_X=V_{app}=V_{ref}+V$. Given that $C_{ref}>>C$, where C represents the capacity of YSZ sample, we can have $V>>V_{ref}$, and thus $V_X \approx V$. The applied electric field, E, on the sample was calculated as $E=V/t=V_X/t$, where t is the thickness of sample. The polarization of sample (P) was calculated as $P = \frac{Q}{A} = \frac{C*V}{A}$, where A and Q are the area of electrode and the charge developed on the sample, respectively. Since the sample is in series with the reference capacitor and they have the same amount of charges on them, we have $Q=Q_{ref}$. The voltage signal from channel Y (V_Y) indicates the voltage drop come across the reference capacitor (V_{ref}).

Therefore, the polarization of sample can be calculated by the equation as $P = \frac{Q}{A} = \frac{Q_{ref}}{A} = \frac{C_{ref}V_{ref}}{A} = \frac{C_{ref}V_Y}{A}$.

4.4 Results and Discussion

Motivated by the observation of the energy dissipation under stress in the previous studies [10, 27, 68, 69], we designed a test to directly observe the stress-strain energy dissipation during loading and unloading process by applying a sinusoidal uniaxial compressive loading on a 8YSZ sample, as it was described in more details in the previous experimental method section (Section 4.3). Figure 4.1b shows the selected but typical stress-strain curves obtained at different temperatures during the cyclic load-unload in compression at the frequency of 0.1 Hz and amplitude stress of 450 MPa. Note here that strains in all tests started from zero when the stress was not applied. However, stress-stain curves are shifted along strain-axes in Figure 4.1b to allow their easy comparison at different temperatures. In addition, five different samples were tested by applying three load-unload cycles at each amplitude stress to check for repeatability of the results. Although Figure 4.1b shows only some typical but selected stress-strain curves, no significant differences among stress-strain curves obtained at the same temperature and amplitude stress were observed for different samples and the number of load-unload cycles. Furthermore, an extremely sensitive resonant ultrasound spectroscope (RUS) was used to check the samples after testing to make sure no cracking was formed during cyclic loading and unloading [178].

As clearly illustrated in Figure 4.1b, 8YSZ shows a typical linear elastic (Hookian) stress-strain behavior at 20 °C and above 500 °C. However, stress-strain curves form fully closed hysteresis loops between 20 °C and 500 °C, indicating that the significant portion of the strain energy was dissipated during each load-unload cycle. The area of the hysteresis loops increase from 20 °C and reaches a maximum around 300 °C. Then the loops shrink with increasing temperature until 500 °C. For comparison (results not shown here), Al_2O_3 was tested under the same conditions as 8YSZ and no hysteresis loops were observed over the entire temperature range. As expected, the strain almost linearly increased with the applied stress in Al_2O_3 similar to 8YSZ at 20 °C or above 500 °C.

The results of further analysis of the stress-strain hysteresis loops in 8YSZ and Al_2O_3 under 10 – 450 MPa are presented in Figure 4.1c where the change of the secant moduli (open symbols) and energy dissipation (W_d, closed symbols) are plotted as a function of temperature. The change of the secant moduli in 8YSZ is nonlinear with a minimum value around 400 °C. Simultaneously with the significant drop of the secant moduli, two large energy dissipation peaks were observed with one around 100 °C and the other one around 300 °C. For comparison, the energy dissipation for Al_2O_3 was also calculated and plotted in Figure 4.1c. No large energy dissipation was observed in Al_2O_3 throughout the entire temperature range. These results are in good agreement with our previous results obtained using DMA and RUS [69], which showed two tanδ peaks in the same temperature range, together with a significant drop in elastic moduli. In

addition, the previous measurements of internal friction (mechanical loss) in single crystal and polycrystalline 8YSZ samples also showed two relaxation peaks [10, 68].

This pseudoelastic or superelastic behavior of 8YSZ with a large stress-strain hysteresis and corresponding significant drop in elastic moduli between 20 °C and 500 °C is fairly unusual for otherwise brittle linear-elastic ceramics, and more typical of viscoelastic and ferroelastic materials. When the mechanical loss coefficient of 8YSZ around 300 °C was calculated as E''/E', which is equal to mechanical damping ($\tan\delta$), where E' and E'' represent storage modulus and loss modulus, and plotted vs. elastic modulus in Ashby map (Figure 4.1d) together with other materials, it is clear that the mechanical loss in 8YSZ is comparable to that of some viscoelastic polymeric materials, although its elastic modulus is still comparable to that of other stiff ceramics.

Large stress-strain hysteresis has been previously observed in some ferroelastic ceramics, such as $Pb_3(PO_4)_2$ [179], $LaAlO_3$ [180], $BaTiO_3$ [181] and Sm_2O_3 [182], in which twinning occurring under applied stresses results in the hysteretic stress-strain behaviors [183]. Ferroelasticity in ceramics normally appears in low symmetry structures as a result of changes between twin orientations (ferroelastic domain switching) [184, 185]. The stress-induced abnormal strain change in ferroelastic materials is nonlinear, highly non-Hookian, and leading to spontaneous strains. The spontaneous strain indicates the distortion from the original phase to the paraelastic one [183]. An abnormal decrease in elastic moduli or softening occurs with the spontaneous strain in ferroelastic materials [184]. Most ferroelastic materials show the phase transformation from a ferroelastic phase to a paraelastic phase only up to a critical

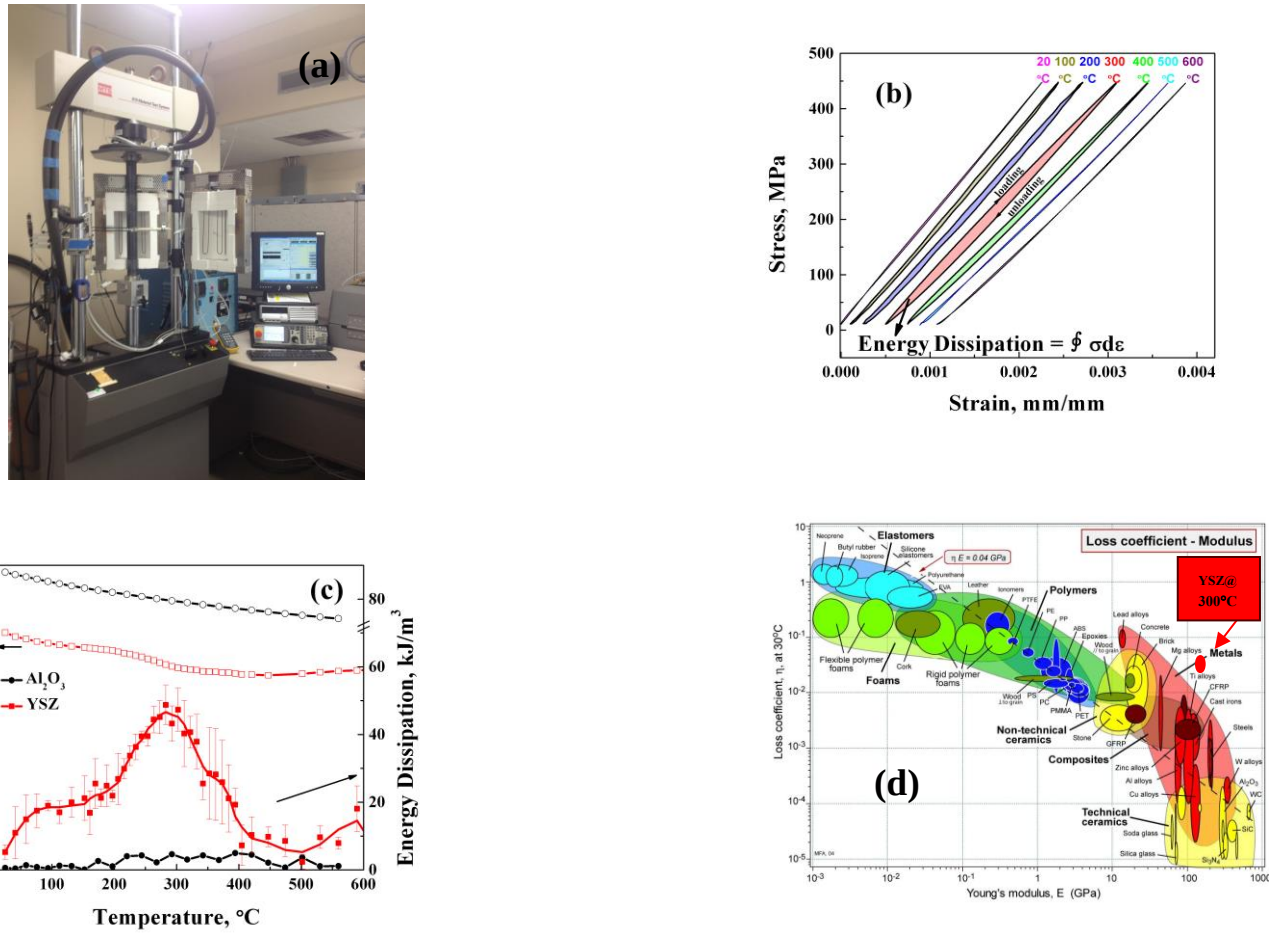

Figure 4.1. (a) Cyclic loading test setup (b) stress − strain hysteresis loops at different temperatures at 0.1 Hz (c) the change of the secant modulus and energy dissipation of 8YSZ and Al_2O_3 with temperature under 450 MPa, calculated as the area of a stress-strain loop (d) the comparison of loss coefficient and Young's modulus of 8YSZ with other materials in the Ashby map [186].

temperature, called the Currie temperature (T_c).

Ferroelastic behavior has been observed and studied in some Y_2O_3, CeO_2, and MgO doped zirconia ceramics [187-191]. ZrO_2 has a monoclinic structure at room temperature, and doping can stabilize its high temperature tetragonal or even cubic structure down to the room temperature. For example, in the monoclinic zirconia, doping with 3 mol% Y_2O_3 (3Y-PSZ), the tetragonal phase was partially stabilized at room temperature. 3Y-PSZ exhibits higher toughness when compared to ZrO_2 and thus, is an excellent material to be used as durable thermal barrier coatings, dental crowns, etc. One of the toughening mechanisms in 3Y-PSZ is based on the ferroelastic domain switching within the tetragonal-prime (t') structure. Without stress, the tetragonal structure has six different energetically equivalent orientations of the c-axis. Under stress, one of them is more favorable [192]. Obviously, the ferroelastic domain switching in 3Y-PSZ can only happen due to the presence of tetragonal structure. It is also worth mentioning here that ferroelastic materials also show more or less open hysteresis looks due to a remanent strain upon unloading, unlike in the case of 8YSZ (Figure 4.1b).

Unlike 3Y-PSZ, 8YSZ examined here has a fully stabilized centrosymmetric cubic ($Fm\bar{3}m$) structure at room temperature. If we assume that the mechanism responsible for the pseudoelastic behavior of 8YSZ is similar to those observed in the traditional ferroelastic zirconias, we can expect that a stress induced phase transformation from a high symmetry structure (cubic) to the low symmetry one (tetragonal) take place in 8YSZ and eventually, ferroelastic twinning could happen in the tetragonal phase. It is worth emphasizing here that the phase transformation from the

cubic to tetragonal or even monoclinic structure has been discussed before [193, 194] as a possible phase transformation because 8YSZ is near the cubic/tetragonal boundary in the phase diagram of Y_2O_3-ZrO_2. However, as to our best knowledge, there is no firm experimental evidence confirming that this phase transformation could happen under applied stress at any temperature.

In-situ neutron diffraction is an important technique to identify a long-range phase transformation or a ferroelastic transformation. The appearance of new phase can be identified by the structure refinement using the full profile fitting approach—the Rietveld method. As to the detection of ferroelastic transformation, one case is the transformation to a preferred orientation under stress in the tetragonal crystallites 3Y-PSZ [151]. Under uniaxial stress, the preferred orientation was observed among the six different orientations of the c-axis in tetragonal YSZ by analyzing neutron diffraction pattern. Cain et al. [151] pointed out that the ferroelasticity and crystalline reorientation in tetragonal YSZ can be observed by the abnormal changes of the stress-lattice strain hysteresis loop and a/c ratio (a, c: the lattice parameter of the tetragonal unit cell) under continuously increasing stress. This crystalline reorientation or ferroelastic microdomain switching is a stress-assisted process. Another case is in the perovskite-type ferroelastic $LaCoO_3$. Aman et al. [195] observed a significant texture formation under uniaxial stress by the in-situ neutron diffraction.

In this study, 8YSZ was studied by an in-situ neutron diffraction to see if tetragonal phase was present in the initial samples or formed during loading in the 20 – 500 °C temperature range that might contribute to the observed pseudoelastic behavior.

The neutron diffraction data was collected at different stress levels while applying stepwise load-and-hold uniaxial compressive stress from 10 MPa to 550 MPa, and then returned back to 10 MPa (for the specific stress steps, refer to the method section). Sample was tested at room temperature and 350 °C when it showed the largest hysteresis loop. Figure 4.2b shows selected, but typical, four neutron diffraction patterns and fitting results under the lowest and highest stresses at room temperature and 350 °C. Two phases were identified using the Rietveld method including the cubic of the $Fm\bar{3}m$ space group 8YSZ and cubic Fe structure induced by the stainless steel heating sleeve outside of the sample. No obvious tetragonal or monoclinic peak appeared at 350 °C and room temperature under different stresses. The only obvious peak that may be attributed to tetragonal phase is that at d-space around 2.1Å shown in Figure 4.2c. However, the peak position stayed unchanged at the same d-space under different stresses and changed only slightly with temperature due to thermal expansion. On the other hand, all peaks belonging to 8YSZ changed their position significantly with the different applied stresses (not shown here). This stress-independence peak at d-space around 2.1Å is different indicating that it originates from the stress-free heating sleeve material, and not from the loaded sample.

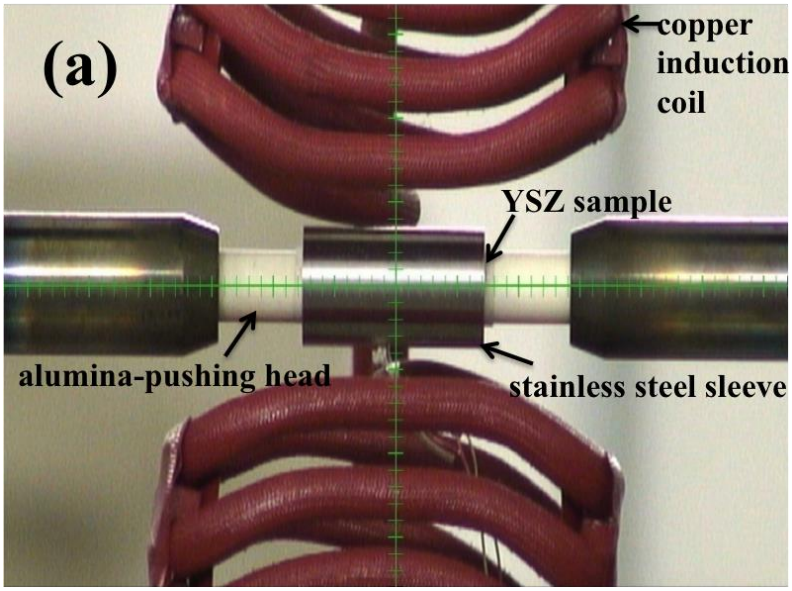

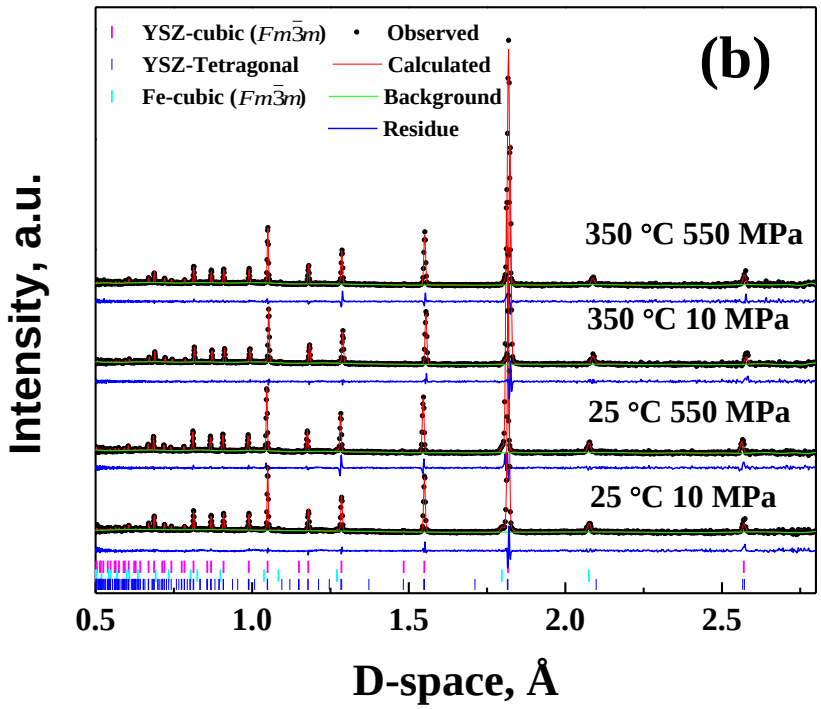

Figure 4.2. (a) Picture of in-situ neutron diffraction sample setup (b) neutron diffraction patterns and fitting results.

Therefore, we can conclude that the in-situ neutron study of 8YSZ showed no obvious phase transformation from cubic to tetragonal, monoclinic or rhomobohedral at different temperatures and under stresses. Also, no obvious texture was observed in 8YSZ at all testing conditions. This rules out any possible long-range phase transformations between the high symmetry and low symmetry structures under stress or ferroelastic switching previously observed in partially stabilized zirconia ceramics as a mechanism responsible for the observed pseudoelastic behavior.

Furthermore, the neutron diffraction results were analyzed to determine stress-lattice strain plots for selected crystallographic planes at room temperature and 350 °C from the single peak fits of the neutron diffraction patterns. As it is shown in Figure 4.3, the lattice strain change linearly with the applied stress at room temperature, as it is expected for any linear-elastic (Hookian) material. However, the stress vs. lattice strain curves show an obvious nonlinear change at 350 °C for some lattice planes. The shape of the curve (Figure 4.3) resembles the shape of one half of the hysteresis stress-strain loops obtained in mechanical testing (Figure 4.1b). By connecting two points under the minimum and maximum stresses (red line in Figure 4.3), we can observe that the deviations of the stress-strain curves from the straight line are different on various planes. The largest deviation shows on the (400) plane. This abnormal change of lattice-strain at 350 °C suggests that this phenomenon can be attributed to another mechanism, namely the reorientation of the oxygen vacancy complexes by vacancy hopping, rather than to any ferroelastic switching or stress induced phase transformation.

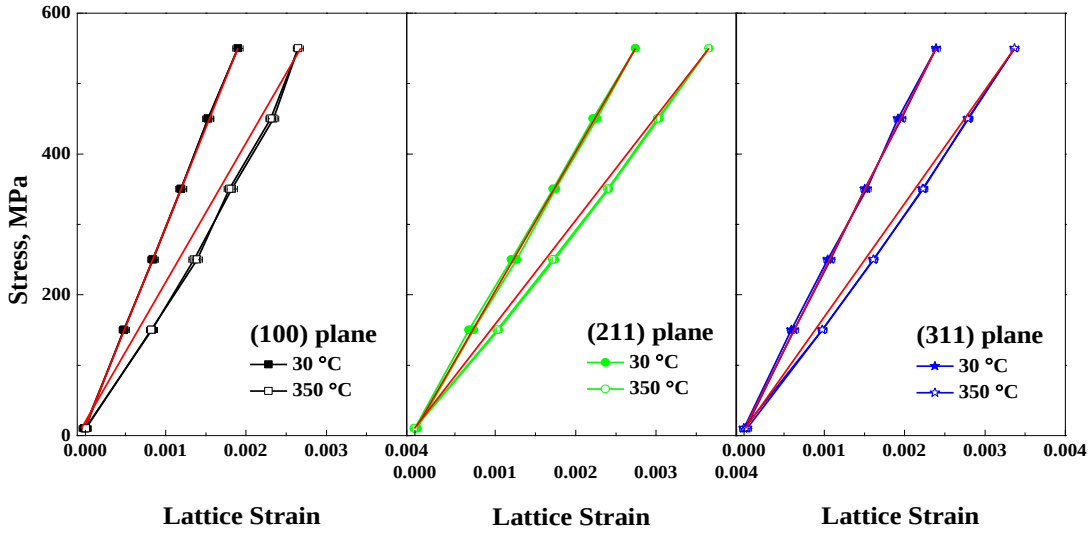

Figure 4.3. The comparison of stress vs. lattice strain on different lattice planes at room temperature and 350 °C. Red line connects two points under the minimum and maximum stresses.

It has been proposed [10, 57, 60, 61] that the defect complexes in doped zirconia ceramics could orient with both applied stress and electric field. As discussed at the beginning of this section in more detail, oxygen vacancies in 8YSZ tend to form several types of complexes and short-range ordering domains [57]. Wachtman's eight-position model [62] in Figure 1.4a shows that oxygen vacancies have the same possibility to occupy the eight equivalent first-neighbor positions (labeled as '1's in Figure 1.4a)

around either a dopant cation (used as an example in Figure 1.4) or host cation. However, the eight positions could be biased if applying an electric or stress field, as those complexes form elastic and electrical dipoles. Nowick et al. [60, 63] was the first who proposed that the anelastic relaxation or dielectric relaxation of the simple elasto-electric dipoles, $(Y'_{Zr}V_O^{\bullet\bullet})^{\bullet}$, can take place under an electric field or applied stress, dissipating energy under cyclic loading or electric field. If we look at (110) planes and $(Y'_{Zr}V_O^{\bullet\bullet})^{\bullet}$ dipole as an example (Figure 1.4b), the dopant-vacancy association with a partial separation of charges (electric dipole) can reorient under the electrical field in a [111] direction by the thermally activated hopping of the vacancy around the dopant cation as illustrated in Figure 1.4c. This reorientation process results in dielectric relaxation at temperatures below ~600 °C [64-67]. For example, Komine et al. [17, 109] reported that this dielectric relaxation is thermally activated with activation energy of around 1.2 eV in single crystal YSZ. Similarly, when stress is applied, for example in the [111] direction on the (110) plane as it is illustrated in Figure 1.4d, the oxygen vacancy can also jump to the preferential positions to minimize the lattice strain energy. The latter is commonly referred as anelastic relaxation. As it is discussed in the previous studies [10, 55, 58, 68, 69], this process results in frequency dependent, thermally activated anelastic relaxation peaks in mechanical loss spectra. Two relaxation peaks are usually observed in the mechanical loss spectra of 8YSZ: one at lower temperatures with the activation energy of 1.28 eV, which is similar to the activation energy of dielectric relaxation (~ 1.2 eV), and one at higher temperatures with activation energies of 2.7 ± 0.2 eV [68, 69]. Previous simulation models and experimental results show the relaxation

time of the anelastic relaxation is two times that in the dielectric relaxation [107, 108], as expected. Also, the activation energies for the anelastic and dielectric relaxation processes are found to be very similar [106, 107]. Based on the proposed models for the reorientation of electro-mechanical dipoles under electric field or applied stresses, one would expect that the reorientation of those dipoles under applied stress would result in the simultaneous spontaneous separation of charges, i.e. the polarization of material under applied stress. However, to our best knowledge, this has not been demonstrated in the avaliable literature.

To further investigate the stress induced reorientation of electro-mechanical dipoles as a possible reasons for observed pseudoelastic behavior and the dissipation of strain energy, we have measured the voltage output signals between two electrodes on the 8YSZ sample during cyclic load-unload in compression as it is illustrated in Figure 4.4a. Figure 4.4b shows that a corresponding sinusoidal voltage output signal was observed under applied sinusoidal stress (5 – 650 MPa) at 300 °C. In addition, the frequencies of the voltage outputs are the same as that of the applied stresses as it is illustrated in Figure 4.4b for two selected frequencies (1 Hz and 10 Hz). The same tests were repeated under various amplitude stresses with a frequency of 1 Hz at different temperatures. Figure 4.4c shows no polarization at 20 °C and 600 °C under the applied cyclic compressive stress with amplitudes ranging from 50 to 650 MPa. However, Figure 4.4c also illustrates that cyclic loading in the 210 °C to 570 °C temperature range generates voltage in which the magnitude of voltage depends on the magnitude of the amplitude stress. Furthermore, when the magnitude of measured voltage ΔV is plotted

as a function of temperature for different amplitude stresses in Figure 4.4d, the spontaneous polarization shows between 210 °C and 570 °C. The reason for the difference between the ΔV vs. temperature curve and the mechanical damping vs. temperature curve is still unclear. However, it is probably attributed to the different types of anelastic dipoles and dielectric dipoles. The same testing procedures were used to measure ΔV on an alumina (Al_2O_3) sample and no voltage output was detected throughout the entire temperature range (black line in Figure 4.4d), as expected.

Results shown in Figure 4.4 are the first experimental evidence of piezoelectric behavior in 8YSZ as a result of spontaneous polarization due to the stress-induced reorientation of electro-elastic dipoles in 8YSZ. However, unlike typical piezoelectric materials having crystal structures that belong to one of the 20 non-centrosymmetric crystal systems [116, 196-198], 8YSZ has a centrosymmetric fluorite (cubic) structure. Therefore, results shown here suggest that electro-mechanical coupling similar to that observed in piezoelectric materials can also be achieved in the centrosymmetric crystal systems by the introduction of point defect clusters having lower symmetry than that of host crystal structure such as $(Y'_{Zr}V_O^{\bullet\bullet})^{\bullet}$ clusters with trigonal symmetry [60, 63] or $(Zr^x_{Zr}V_O^{\bullet\bullet})^{\bullet\bullet}$ clusters in the cubic 8YSZ. It is worth noting here that an inverse behavior has been recently observed in another binary oxide, namely CeO_2 doped with Gd_2O_3 ($Ce_{0.8}Gd_{0.2}O_{1.9}$) [199] that shows giant electrostriction due to the reorientation and alignment of $(Ce^x_{Ce}V_O^{\bullet\bullet})^{\bullet\bullet}$ dipoles under applied electric field.

Finally, we have measured the electrical polarization of 8YSZ vs. electrical field (P-E) under constant compressive stresses using the experimental setup illustrated in

Figure 4.5a and described in more detail in the experimental procedure section. The applied stress was kept at different constant values while applying an alternating electric field at 1 Hz frequency at 25 °C, 150 °C, 300 °C and 450 °C in the same direction as applied stress. Figure 4.5b shows that very small, stress independent polarization loops at 25 °C suggesting very weak ferroelectric response of 8YSZ. However, 8YSZ shows distinct stress dependent polarization loops at 300 °C, Figure 4.5c. The values of polarization range from 1.1 μC/cm^2 at 150 MPa to 3 μC/cm^2 at 300 MPa and 450 MPa, while the measured coercive fields were relatively low, ranging from 1.4 kV/cm at 150 MPa to 2.6 kV/cm at 300 MPa and 450 MPa. The obtained values in this case falls within the ranges of remnant polarizations (0.1 – 100 μC/cm^2) and coercive fields (1 – 100 kV/cm) measured in typical piezoelectric materials [200]. Although 8YSZ samples show polarization that is quite lower than a typical value for polycrystalline PZT ceramics (about 30 μC/cm^2), it is still valuable result since it is obtained at 300 °C in simple, chemically, thermally stable and inexpensive material under relative lower electric field without prepoling. The latter cannot be overemphasized since that the operating temperature of traditional piezoelectric ceramics is typically at temperatures lower than 200 °C and scientists are in constant search for high temperature (>300 °C), especially lead free piezoelectric ceramics [201, 202]. Finally, no polarization loops were observed at 450 °C (Figure 4.5d) most likely because defect complexes disassociated at that temperature and the directional migration of oxygen vacancies under electric field took place.

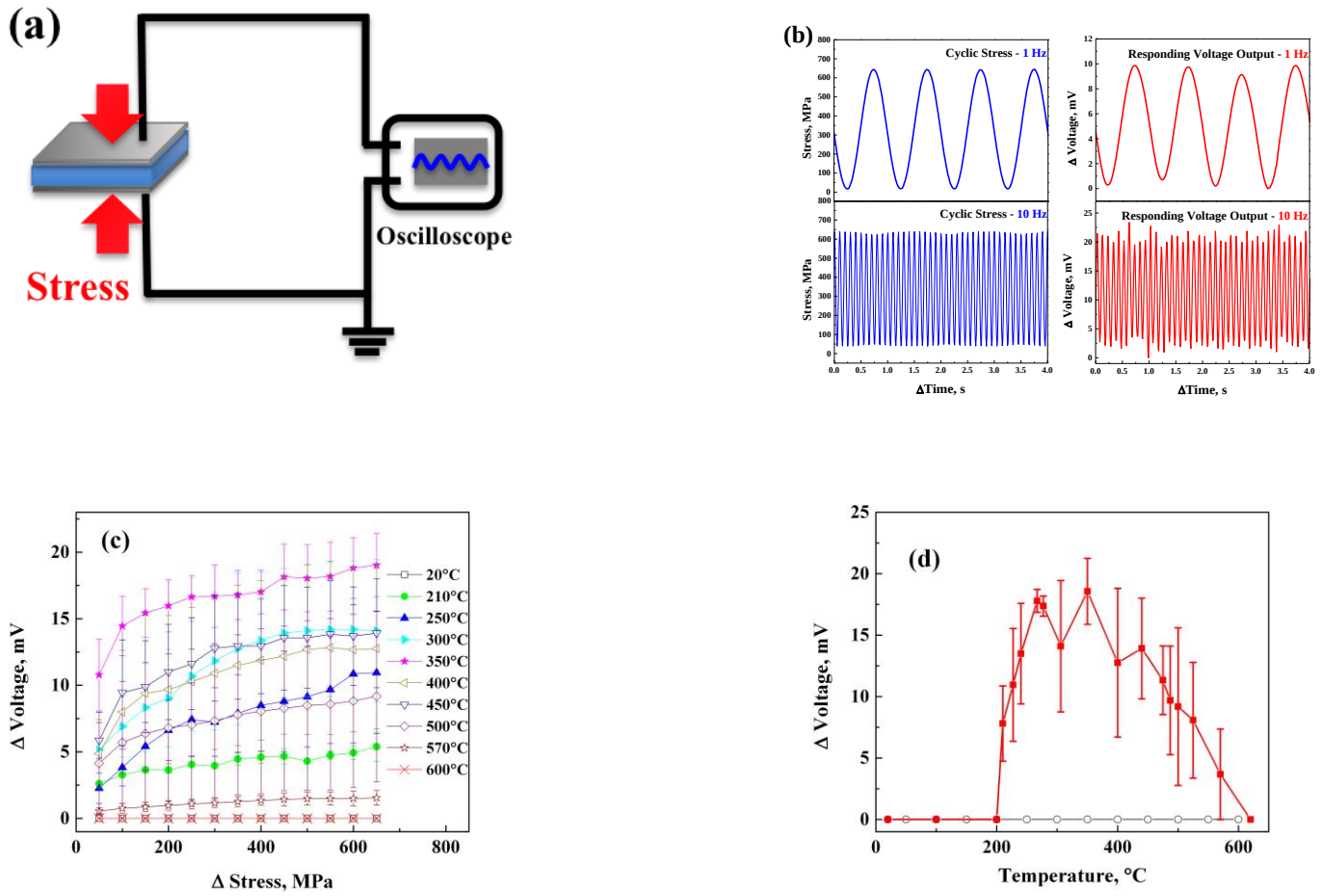

Figure 4.4. (a) Setup of electro-mechanical coupling test (b) corresponding Δ voltage vs. Δ time under different frequencies of applied sinusoid stresses at 300 °C (c) corresponding ΔV vs. 0.1 Hz sinusoid stress of 8YSZ at different temperatures (d) Δ voltage vs. temperature of 8YSZ and Al_2O_3 under 5 − 650 MPa.

When the results presented here are put in conjunction, it is clear that the doping of inexpensive and widely available binary oxides having a centrosymmetric fluorite structure with aliovalent cations and their arrangements in the defect clusters with the lower symmetry that can reorient under applied stress or electric field by oxygen vacancy hopping. The reorientation process can results in a direct piezoelectric effect, i.e. spontaneous polarization under applied electric fields. This provides a new way to design materials for high temperature stress sensors by only manipulating the type and structure of the defect clusters, as the spontaneous polarization in those materials is stress dependent (Figure 4.4c). In addition, no pre-polarization under high voltage is needed for 8YSZ, unlike in the case of typical piezoelectric materials. The working temperature range and sensitivity of sensors can be tuned by changing the host cation and dopant, or adding a different concentration of dopant. These changes adjust the activation energy of the dielectric relaxation and, thus, lead to different working temperature ranges or different sensitivities to the applied stress. Finally, one of the common limitations in typical piezoelectric materials is phase transformation leading to a disappearance of piezoelectricity at higher temperatures. However, this is not an issue with 8YSZ as it has stable fluorite structure up to 2690 °C [203].

By studying the activation energy of dielectric and anelastic relaxation, we hope to find some rules to guide the design of high temperature defect sensors. The activation energy (H_c) for ionic conductivity is the sum of association enthalpy (H_a) and migration enthalpy (H_m) below 600 °C before the oxygen vacancy becomes completely free [16].

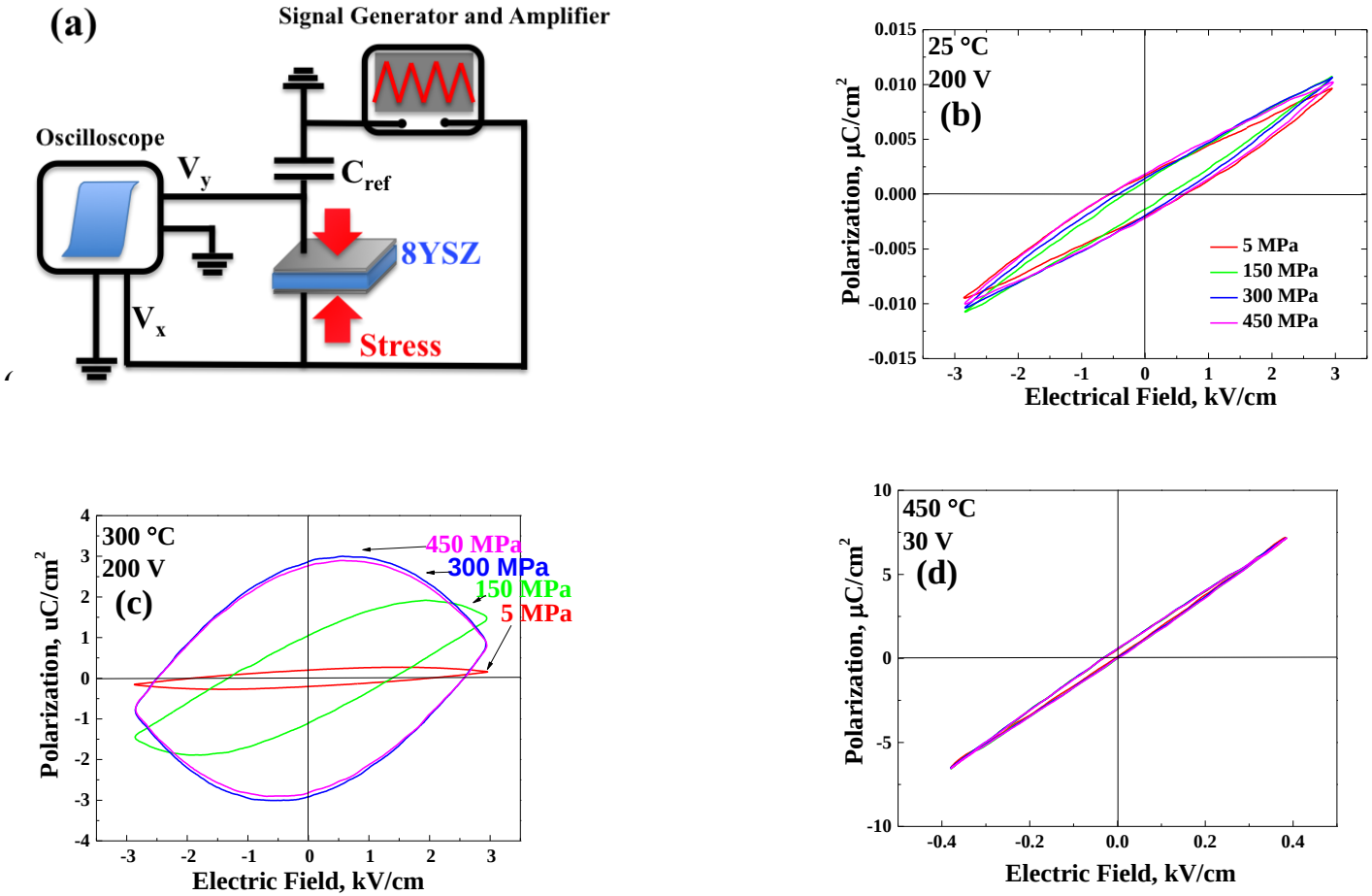

Figure 4.5. (a) Setup of polarization test. The polarization of 8YSZ at (b) 25 °C, (c) 300 °C and (d) 450 °C under applied voltage parallel with compressive loadings at different temperatures. Note: the sample was tested under 30 V electrical field in the Figure 4.5d at 450 °C, which is different with other tests, due to the high conductivity of 8YSZ at 450 °C reaching the test limit of oscilloscope.

On one hand, migration enthalpy increases while association enthalpy decreases with increasing dopant radius; one the other hand, the large ionic radius of dopants would reduce the Columbic attraction force between charged defects and dopants. The study of the zirconia-based and ceria-based oxides illustrate that the change of activation energies show a convex curve with the increase of difference between doped ion radius and critical ion radius. The critical ionic radius is calculated based on reducing the lattice strain in the material. RUS results show that the temperature range of the mechanical damping is higher with larger activation energy. From this point of view, the temperature and sensitivity of stress sensor can be tuned by host cation, type and concentration of dopants.

4.5 Conclusions

In summary, results presented here show the pseudoelastic behavior of 8YSZ during compressive cyclic loading with large stress-strain hysteresis loops in a particular temperature range (20 °C – 500 °C). Between 210 °C and 570 °C, electro-mechanical coupling behavior was observed in 8YSZ similar to that of piezoelectric materials, i.e. stress induced spontaneous polarization was measured under applied compressive stress. Therefore, this unusual pseudoelastic behavior and piezoelectric coupling in 8YSZ are not related to long-range phase transformation or domain switching, but to the reorientation of defect complexes with a lower symmetry that form electro-elastic dipoles under applied stress and electric field. This finding paves the way toward development of new, inexpensive piezoelectric materials for high temperature stress

sensing by engineering point defects and their clustering in binary oxides with a fluorite structure.

5. EFFECT OF PHASE TRANSFORMATIONS ON MECHANICAL PROPERTIES OF 10 MOL% Sc_2O_3 – 1 MOL% CeO_2 – 89 MOL% ZrO_2

5.1 Summary

The elastic moduli, energy dissipation and electro-mechanical coupling response of 10 mol% Sc_2O_3, 1 mol% CeO_2, 89 mol% ZrO_2 (SCSZ) have been characterized at elevated temperatures. Two different structures of SCSZ were studied: (i) fully stabilized cubic and (ii) two-phase (60.05% rhombohedral + 39.95% cubic) structure at room temperature obtained after a long term annealing of the cubic structure at 350 °C. Elastic moduli, which was determined using resonant ultrasound spectroscopy (RUS) and cyclic compression testing (CCT), showed non-linear decrease with the temperature with minimum values in the 400 – 600 °C temperature range. The decrease of elastic moduli in two-phase SCSZ around 500 °C is much larger and steeper than in cubic SCSZ, indicating more rhombohedral phase transforms back to cubic at this temperature. Simultaneously with the large decrease of elastic moduli, SCSZ shows large energy dissipation peaks, which are both caused by the relaxation of defect complexes and phase transformations. Large stress-strain hysteresis loops were observed under sinusoidal compressive stresses between 200 °C and 500 °C, showing that the energy dissipation of SCSZ under stresses is caused mainly by phase transformations. However, spontaneous polarization was observed in SCSZ only in the 200 – 300 °C range. Corresponding sinusoidal output voltages were recorded with applied sinusoidal stresses at the same frequencies. The latter suggests that anelastic relaxation and dielectric

relaxation due to the reorientation of electro-elastic dipoles under stress result in spontaneous polarization.

5.2 Introduction

Although 8 mol% yttria stabilized zirconia (8YSZ) is a commonly used solid electrolyte material in solid oxide fuel cells (SOFCs), due to its high ionic conductivity [15, 204], its application is limited to very high temperatures as ionic conductivity of YSZ drops sharply from 0.1 S/cm at 1000 °C to 0.03 S/cm at 800 °C. Since decreasing service temperature of SOFC can improve reliability, durability and reduce cost [38, 126], many research efforts have been focused on the development of new electrolyte materials with high ionic conductivity, low electric conductivity, stable chemical, thermal and mechanical properties in both oxidation and reduction environments used at intermediate or low temperatures for the new generation of SOFCs [22].

10 mol% Sc_2O_3 stabilized ZrO_2 (SSZ) is one of the most promising materials to be used in intermediate temperature SOFC (IT-SOFC), since it's conductivity is roughly 1.5 times higher than that in YSZ at 850 °C [205]. However, unstable structure caused by phase transformation from cubic to rhombohedral structure, is one of the most critical problems in SSZ leading to the fast degradation of its structure and decrease in ionic conductivity [206]. To stabilize the cubic crystal structure and reduce phase changes during aging at high temperature service, 1 mol% of different oxides (CeO_2, Al_2O_3, MgO, Ga_2O_3 and Bi_2O_3) were added to SSZ [31, 32, 36, 37, 207-210]. 1 mol% CeO_2 stabilized SSZ (SCSZ) showed the best structural stability and obviously higher

conductivity than others; thus, it has been studied as a potential electrolyte material for IT-SOFC [37, 129, 211].

However, most recently, phase transformations were also observed in 10 mol% Sc_2O_3, 1 mol% CeO_2 stabilized ZrO_2 (SCSZ) [129]. In SCSZ, cubic structure at room temperature is metastable. Cubic phase, stabilized at room temperature, starts to transform to rhombohedral during heating around 300 °C, and then completely changes back to cubic around 500 °C [129]. The fraction of the SCSZ that is in rhombohedral phase between 300 °C and 500 °C temperature range depends on several factors including sintering temperature, annealing temperature, annealing time, grain size, and most likely applied stress, etc. [129, 138, 212]. Although the rhombohedral phase is the thermodynamically stable phase in the 300 – 500 °C, the phase transformations with a low kinetic rate due to low temperatures are expected to have a small influence on the conductivity of SCSZ in a short term. Especially, phase transformations only happen in a relatively short heating and cooling time since the phase transformation temperature range is below its operation temperatures (600 – 800 °C). However, after longer service time, it can result in severe structural degradations and decrease in ionic conductivity.

Besides, local ordering of oxygen vacancies may also contribute to the decrease of conductivity in SCSZ. High ionic conductivity in SCSZ is a result of the directional movement of oxygen vacancies introduced by aliovalent dopants (Sc_2O_3) at high temperatures. The formation of the point defects in SCSZ can be described using Kroger-Vink nomenclature [45]:

$$Sc_2O_3 \xrightarrow{2ZrO_2} 2Sc''_{Zr} + V_O^{\bullet\bullet} + 3O_O^x$$

where V is vacancy; prime is negative charge; dot is positive charge and x is zero effective charge.

Similar as in 8YSZ, in a dilute solution, one oxygen vacancy may associate with one dopant, $Sc'_{Zr} + V_O^{\bullet\bullet} = (Sc'_{Zr}V_O^{\bullet\bullet})^{\bullet}$, primarily to minimize lattice stress and also due to electrostatic attraction, Figure 1.4a. With higher dopant concentration, one oxygen vacancy may cluster with two dopants to form more complex types of dipoles, such as $2Sc'_{Zr} + V_O^{\bullet\bullet} = (Sc'_{Zr}V_O^{\bullet\bullet}Sc'_{Zr})^x$ [67, 156, 213]. A competition between more oxygen vacancies with increasing dopant concentration and more local ordering trapping oxygen vacancies leads to the highest ionic conductivity with about 10 mol% Sc_2O_3.

The effects of the clustering and ordering of oxygen vacancies, and phase transformations on ionic conductivity of SCSZ have been a subject of several studies [38, 214, 215]. However, their effects on the mechanical properties of SCSZ are still poorly understood. It is expected that point defect complexes might have significant effect on mechanical properties of SCSZ similar to their effect on those properties in YSZ and other doped zirconia electrolyte materials [10, 60, 70, 216]. In addition, it has been proposed that the changes of mechanical properties of SSZ, such as elastic moduli, bending strength and fracture toughness, largely depend on phase transformations observed in this material [210]. For example, the addition of only 1 mol% CeO_2 improves significantly bending strength of SSZ as it stabilizes the cubic structure at lower temperatures. However, the changes of Young's modulus, four-point bending strength and fracture toughness show nonlinear change with temperature in SCSZ [84].

The minimum value appears around 500 °C, together with large energy dissipation peaks. This drastic drop in mechanical properties threatens the reliability and durability of the whole devices since 500 °C is close to the operating temperature of SOFC having SCSZ as an electrolyte material. Kushi et al. [55] first proposed that the phase transformations contribute to both the observed significant drop in elastic moduli and increase in the energy loss of SCSZ around 500 °C. More recently we showed [69] that the main reason for the intense drop of moduli in both the pure cubic and two-phase SCSZ is phase transformations from cubic to rhombohedral, and then back to cubic phase. Yarmolenko et al. [140] concluded that the cubic phase SCSZ (10.6×10^{-6} °C^{-1}) shows significantly higher coefficient of thermal expansion (CTE) than rhombohedral phase (8.6×10^{-6} °C^{-1}). This, together with the change in the volume of the unit cell of 0.11 % during cubic to rhombohedral transformation, build up internal stresses in materials and external stresses between electrolyte and electrode layers. Although the phase transformations only happen during the heating and cooling process and long time is needed for the large fraction of phase to transform, decrease in mechanical properties for around 50 % from room temperature to 600 °C is still a big challenge for the long-term service of SOFCs [69, 84].

However, we showed in Section 3 that the reorientation of defect complexes and possible ordering that take place at even lower temperatures (100 – 300 °C) also affect the changes of elastic moduli with temperature [69]. The reorientation of dipoles such as $(Sc'_{Zr}V_O^{\bullet\bullet})^{\bullet}$, $(Zr_{Zr}^{x}V_O^{\bullet\bullet})^{\bullet\bullet}$, $(Sc'_{Zr}V_O^{\bullet\bullet}Sc'_{Zr})^{x}$ and/or local ordering oxygen vacancies were found to be responsible for large frequency-dependent mechanical damping peaks and

the drop of elastic moduli, in a similar manner as in YSZ [69] using dynamic mechanical analysis (DMA). The reorientation process of dipoles under stress is called anelastic relaxation and thus those dipoles are usually referred to as elastic dipole. Several researchers [106, 108, 156] also reported anelastic relaxation in Sc_2O_3 doped CeO_2 (ScDC) with a cubic structure as a process caused by the reorientation of two types of dipoles under stress and electrical field. Weller et al. [74] also discussed a similar anelastic relaxation in different doped zirconias (ZrO_2), including partially stabilized cubic SSZ. According to Weller et al. [74], two mechanical damping peaks observed in the temperature range of -50 – 673 °C can be attributed to different mechanisms. One peak around 227 °C is identified due to anelastic relaxation in SSZ, which shifts to higher temperature with the increase of frequency. Activation energy is 1.2 – 1.3 eV calculated by Arrhenius equation, $\tau^{-1} = \tau_{\infty}^{-1}\exp(-H_r/kT)$. The other frequency independent peaks around 500 °C is caused by ferroelastic phase transformation from the rhombohedral to cubic phase. In our previous DMA study of fully stabilized SCSZ (see previous Section 3) we found 4 damping peaks: Peak 1 with activation energy of 1.2 eV; Peak 3 with activation energy of 6 – 8 eV depending on the applied stress magnitude and Peak 4 around 425 °C that is frequency independent. Activation energy for Peak 2 in this study could not be determined with a high accuracy because this peak partially overlaps with Peak 3.

One of the most effective ways to observe the difference between mechanical loss peaks belonging to phase transformation in SCSZ and those caused by anelastic relaxation is also to look at dielectric properties of SCSZ since vacancy-cation clusters

represent not only anelastic dipoles but also electric dipoles that can be reoriented under electric field [74]. Dielectric relaxation as a result of the reorientation vacancy-cation clusters in SCSZ has not been studied in details. Nowick et al. [108] studied the relationship between electric dipole and elastic dipole in the wide range of doped ceria (CeO_2) ceramics and concluded that the in all of them activation energies for dielectric and anelastic relaxations due to reorientation of vacancy-cation clusters are almost the same, but that relaxation times for dielectric relaxation process must be twice that in anelastic relaxation. In our recent study (see Section 4), we showed for the first time that the stress-induced reorientation of defect complexes also causes spontaneous polarization in 8YSZ.

In this paper, the effect of phase transformation and point defect relaxation on the mechanical properties of different phases SCSZ was studied by resonant ultrasound spectroscopy (RUS) and cyclic compression test (CCT) in more details. In addition, electro-mechanical coupling due to the relaxation of electro-elastic dipoles was analyzed.

5.3 Experimental Methods

All samples in this study were processed from 10 mol% Sc_2O_3, 1 mol% CeO_2, 89 mol% ZrO_2 from Daiichi Kigenso Kagaku Kogyo (DKKK, Japan) commercial powder. The specific surface area of powder is 10.4 m^2/g. The sample processing was described in Section 3.3. Density of samples after sintering were measured by alcohol immersion method based on ASTM Standard C20-00 [132] and all relatively density were higher

than 97 %. Partial phase transformation from cubic to rhombohedral around 300 °C, and then completely back to cubic structure around 500 °C, were detected by HT-XRD, as it was described in more details in Section 2. Cubic structure as processed samples and cubic+rombohedral structure samples after different annealing times and temperatures in SCSZ were confirmed using a room temperature X-ray diffractometer (XRD; D8 Discover, Bruker, Madison, USA) with Cu K_α radiation. Phase compositions were analyzed utilizing the Inorganic Crystal Structure Database (ICSD) and PANalytical X'Pert HighScore Plus software [217]. To eliminate the influence of grain size to mechanical properties, the grain sizes of samples were measured with digital optical microscope (Keyence VH-Z100) and field emission scanning electron microscope (FE-SEM; Quanta 600 FEG, FEI, Oregon, USA) to ensure similar 5 μm grain size (Figure 2.1). Young's and shear moduli of the materials used in the present study were determined using resonant ultrasound spectroscope, RUS, (Magnaflux Quasar, Albuquerque, NM). The experimental details for RUS were provided in Section 2.3**.**

The Materials Testing System (MTS, MTS Systems Corporation, MN, USA) was used in the cyclic loading tests. SCSZ samples were cut to 20 x 10 x 10 mm^3 rectangular blocks for the testing. A sample was loaded between two hydraulic pushing heads and hold by 5 MPa pre-loading stress. Sinusoidal stress was applied from 50 MPa to 450 MPa, and then back to 50 MPa in three loading cycles at each amplitude stress, with a frequency of 0.1 Hz. All tests were carried out at selected temperatures starting from 25 °C to 550 °C with 10 °C/step. A high resolution, high temperature extensometer (Model: 632.59) was directly attached to the sample to record the change of strain under the

applied sinusoidal stress. A split tube furnace was used to heat up the sample to the desired temperature. A K-type thermocouple very close to the sample was used to control the temperature. The sample was hold under preloading for 20 minutes to reach temperature equilibrium before testing. Then, cyclic loading was applied at this temperature and the strain change was recorded by the extensometer. After that, temperature was increased to next desired temperature for isothermal holding. A secant modulus was calculated from the slope of stress-strain curve in the second load-unload cycle. In addition, the area of the hysteresis loops were used to calculate dissipated energy per load-unload cycle as $W_d = \oint \sigma d\varepsilon$, where σ is the stress and ε is the strain.

The electro-mechanical coupling test used a mechanical test system (MTS) to apply sinusoidal loadings, combining with an oscilloscope (DS1102E, RIGOL technologies Inc., OR) to record the corresponding open circuit voltages from a sample. The test setup and procedures were the same as in 8YSZ described in Section 4.3. Five samples were cut to the dimension of 7.5 x 7.5 x 1 mm^3 square plates. Two alumina spacers with the dimension of 10 x 10 x 5 mm^3 were sputtered with 5 μm platinum film on one side as electrodes. One gold wire connected one electrode to a probe of oscilloscope at Channel 1. The second gold wire grounded the other electrode. A nickel cage was put outside of the sample as an electromagnetic shielding. The sample was heated to the desired temperature and then, tested under cyclic loading for 15 cycles at 1 Hz. The applied sinusoidal stress was recorded by MTS system. The oscilloscope recorded six cycles of voltage output signals within the applied 15 cycles. Voltage outputs from the direction of external stress was monitored and recorded at different

temperatures from 25 °C to 550 °C and different sinusoidal stresses. The sinusoidal stresses are between 5 MPa and a maximum value, which is from 50 MPa to 650 MPa with the increments of 50 MPa. ΔV (or ΔVoltage) was calculated from the difference of average maximum and minimum sinusoidal output signals over six cycles.

5.4 Results and Discussion

5.4.1 Phase Transformations in SCSZ

The XRD of SCSZ collected at different temperatures (Section 2, Figures 2.2b and 2.2c) clearly shows a cubic to rhombohedral phase transformation starts at 300 °C and then a rhombohedral completely back to cubic transformation between 400 and 500 °C. To determine the effect of annealing on the formation of rhombohedral structure, the samples were annealed at different temperatures in the 300 – 400 °C temperature range (i.e. 300 °C, 325 °C, 350 °C, 375 °C and 400 °C) for 12 hours in open air. Figures 5.1a and 5.1b summarize the XRD results and phase compositions of SCSZ as sintered and after annealing at different temperatures. SCSZ samples after sintering at 1500 °C for two hours had 100% cubic structure at room temperature, which is good agreement with the results published by Yarmolenko et al. [129] showing that SCSZ was a pure cubic phase after sintering above 1300 °C. The lattice parameter calculated from the XRD results is 5.09 Å at room temperature. Both rhombohedral and cubic peaks exist in samples after annealing at different temperatures in 300 – 400 °C for 12 hours.

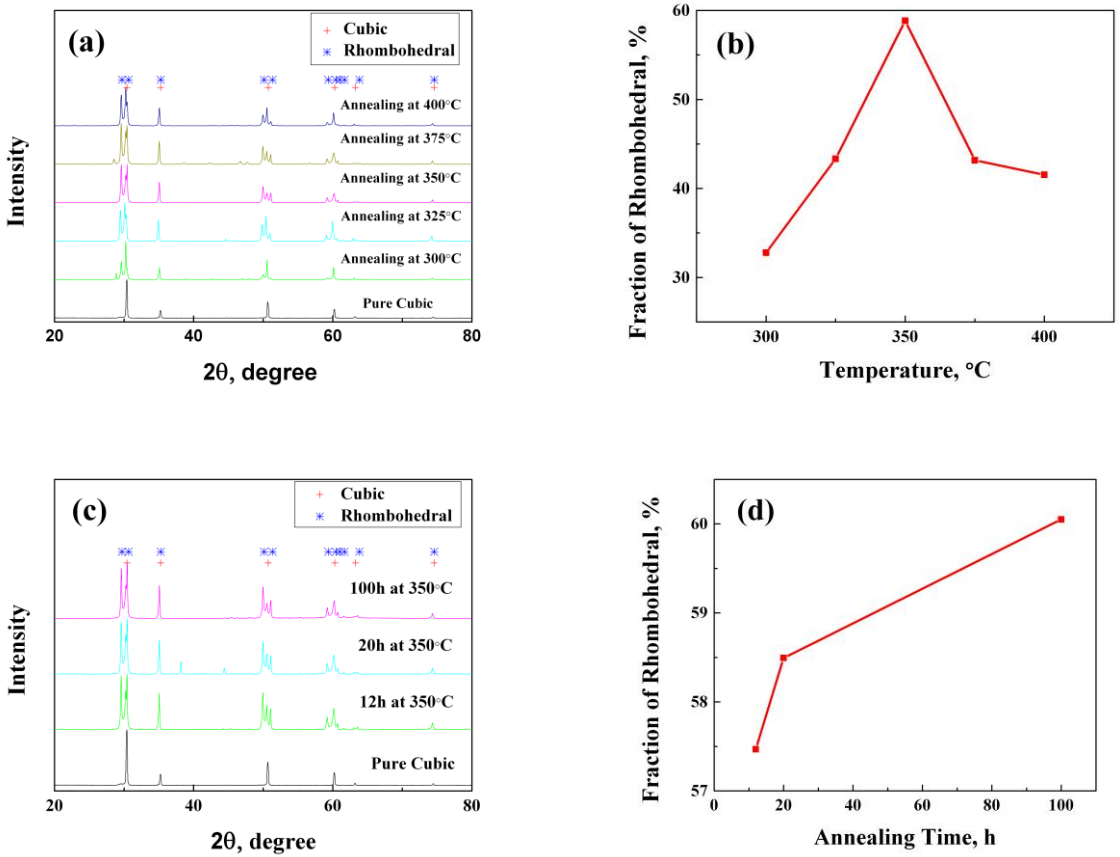

Figure 5.1. (a) The XRD patterns and (b) the fractions of rhombohedral phase of annealed SCSZ at different temperatures for 12 hours. (c) The XRD patterns and (d) the fractions of rhombohedral phase of SCSZ annealed for different times at 350 °C.

The fraction of the rhombohedral phase vs. temperature was calculated and shown in Figure 5.1b. The content of rhombohedral phase reached a maximum at 350 °C, which is 57.4% after annealing for 12 hours. The latter is in disagreement with results published by Yarmolenko et al. [129] because they found a large fraction of rhombohedral phase (>90%) after annealing around 350 °C for 12 h. One possible explanation for the difference is the content of impurities in different batches of powders. Moreover, results shown here suggest that unlike rhombohedral-to-cubic phase transformation around 400 – 500 °C, which is almost instantaneous, the kinetics of cubic-to-rhombohedral phase transformation is quite sluggish.

To further study the kinetics of this reaction, the phase compositions of SCSZ samples after annealing for different times at the temperature of 350 °C at which the largest fraction of transformed rhombohedral structure was observed (Figures 5.1c and 5.1d). XRD results of SCSZ samples after annealing for different times in Figure 5.1c show the amount of transformed rhombohedral phase increases with annealing time. The fractions of rhombohedral phase were calculated and plotted in Figure 5.1d after annealing for up to 100 h. It shows the fraction of rhombohedral phase reaches value of 60.05% after annealing time from at 100 h. These results once again confirm very slow kinetics of cubic-to-rhombohedral phase transformation around 350 °C. To further investigate the effect of rhombohedral phase on the elastic and mechanical properties of SCSZ, some of the samples used for DMA in Section 3.4.2 and RUS were annealed at 350 °C to obtain samples with 60.05 % rhombohedral and 39.95 % cubic structure (two-phase SCSZ).

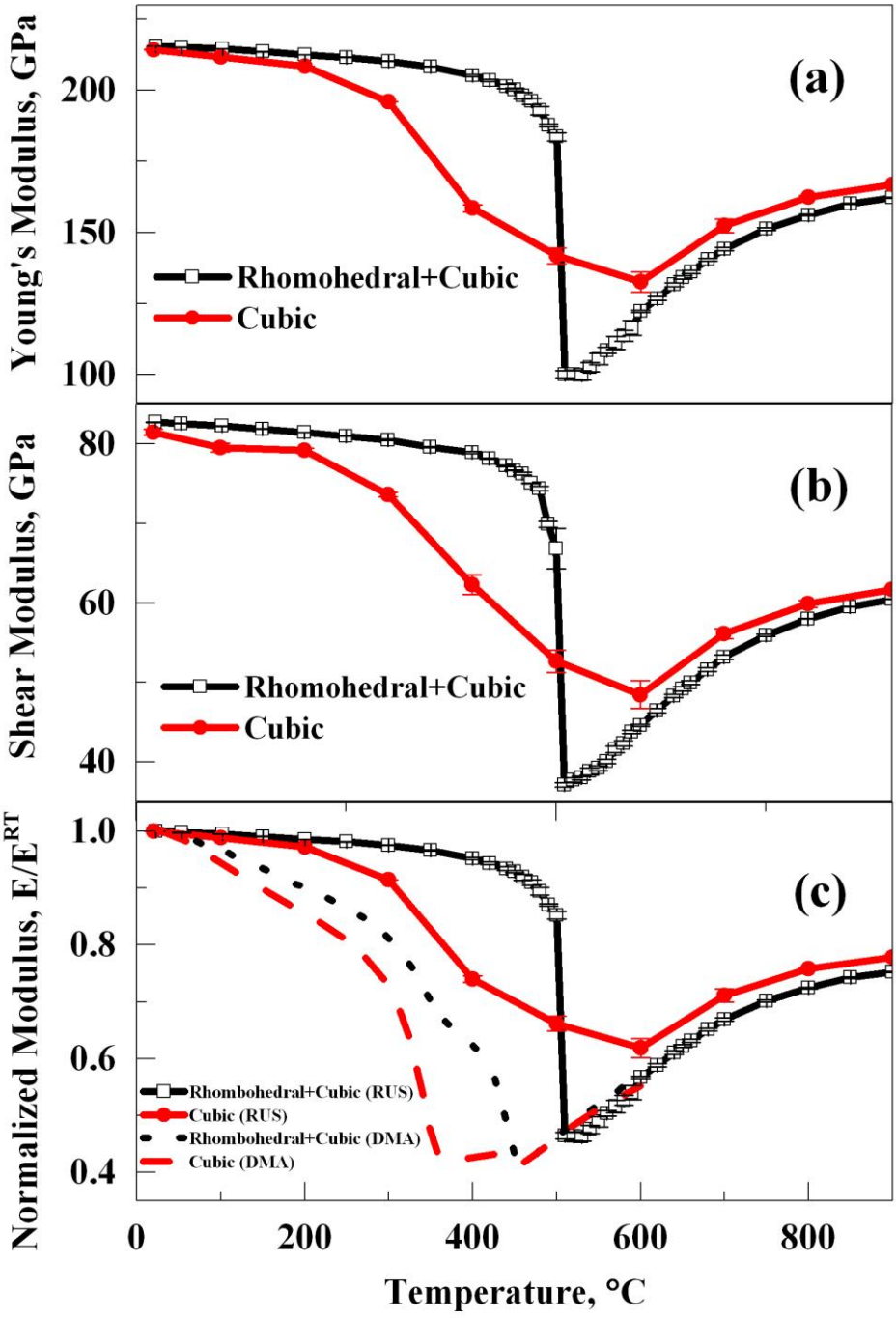

Figure 5.2. (a) Young's modulus and (b) shear modulus of cubic SCSZ and two-phase SCSZ from 25 °C to 1000 °C from RUS results (c) comparison of the changes of normalized modulus from RUS and DMA. DMA data were obtained at 0.1 Hz. Note: E^{RT} represents the modulus at room temperature.

5.4.2 Elastic Properties of Cubic and Two-phase SCSZ

The changes of the Young's and shear moduli of cubic SCSZ and two-phase SCSZ determined by RUS in the 25 °C to 900 °C temperature range are shown in Figure 5.2. The Young's and shear moduli of two-phase SCSZ having 60.05 vol% rhombohedral phase show sharp, abrupt drop (45.6 % decrease) of elastic moduli around at 500 °C. In cubic SCSZ, elastic moduli start to decrease significantly at much lower temperatures, i.e. around 150 °C and gradually decrease in non-linear manner until they reach a minimum around 600 °C. For example, Young modulus of cubic SCSZ gradually decrease from ~210 GPa to ~130 GPa in this temperature range, i.e. it decreases for 38%. In contrast, the change of Young's modulus in two-phase SCSZ shows much larger decrease from 216 GPa at room temperature to the minimum value of 100 GPa at 510 °C. Furthermore, there is an instant drop from 184 GPa at 500 °C to 100 GPa at 510 °C in two-phase SCSZ. Elastic moduli of both two-phase and cubic SCSZ increase with temperature above 500 °C and 600 °C, respectively, up to 900 °C, reaching almost the same values at 900 °C. The changes of shear modulus in Figure 5.2b follows the same trend as Young's modulus in both pure cubic and two-phase SCSZ.

Large differences in the changes of elastic moduli with temperature can be attributed to the cubic to rhombohedral and back to cubic phase transformations. As discussed in introduction, partial phase transformation from cubic to rhombohedral starts around 300 °C followed by another phase transformation from rhombohedral completely back to cubic around 500 °C. The first phase transformation was also found to depend on the frequency of applied load, i.e. it shifted to higher temperatures with increasing

frequency or rate of applied load. Two-phase sample contain 60.05 % rhombohedral phase after annealing and thus very small amount of cubic phase is left to partially transform to rhombohedral around 300 °C. resulting in less steep drop of elastic moduli in the 300 – 500 °C temperature range when compared to cubic SCSZ. However, in pure cubic samples, only small portion of structure transformations to rhombohedral at 300 °C, resulting in less abrupt drop in elastic modulus during rhombohedral-cubic transformation around 500 °C.

Those findings are in agreement with DMA results for both cubic and two-phase SCSZ in Figure 5.2c. The abnormal changes of elastic moduli of RUS results are consistent with the nonlinear change of storage modulus in dynamic mechanical analysis (DMA) results. The similar trends indicate that the same mechanisms contribute to the drop of moduli in DMA and RUS. According to a more detailed analysis in Section 3.4.2 [69], the drop of storage modulus are attributed mainly to phase transformations and, to some extent, anelastic relaxation and/or local ordering of oxygen vacancies. The percentage of modulus drop tested by DMA is larger than that obtained using RUS in cubic SCSZ. The reasons for the difference are not very clear, but it might be attributed to the differences between two testing methods. First, the frequency used in DMA (0.01 – 100 Hz) is 3 – 4 orders of magnitude smaller than that in RUS test (20 – 500 kHz). Phase transformation from cubic to rhombohedral at 300 °C, which contributes to the large drop of storage modulus at lower temperatures, is a frequency-dependent process as shown in Section 3 [69] and thus the intense large mechanical damping peaks shift to higher temperatures under higher frequencies. Second, stresses experienced by

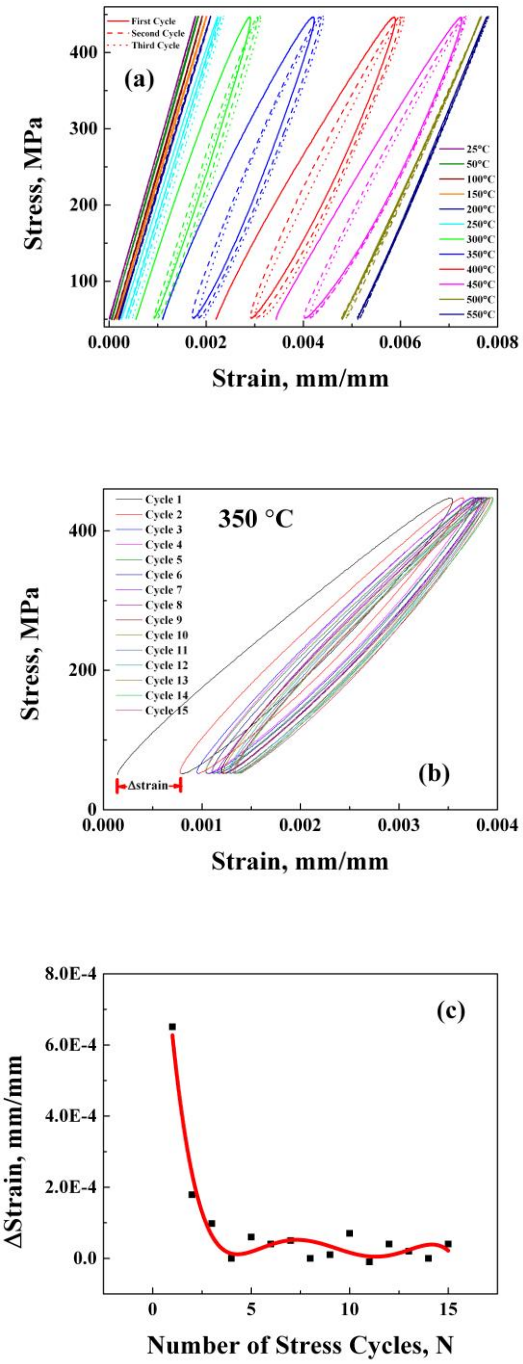

Figure 5.3. (a) The stress vs. strain curves of SCSZ under sinusoidal stresses with 0.1 Hz frequency between 10 – 450 MPa at different temperatures for three load-unload cycles (b) the stress vs. strain curves of SCSZ at 350 °C for 15 cycles with 0.1 Hz frequency (c) the differences of strains (Δstrain) before and after loading for one cycle at 350°C.

sample during DMA testing are significantly larger than those in RUS. Moreover, those external stresses can largely assist phase transformation in SCSZ from cubic to rhombohedral as it was suggested elsewhere [212].

5.4.3 Stress-strain Hysteresis in Cyclic Compression Test (CCT)

Since the large non-linear drop of elastic moduli with increasing temperature were found in SCSZ accompanied with increase in mechanical damping peaks using both DMA and RUS tests, sinusoidal compressive loading test was carried out to directly observe effects of energy dissipation (Figure 5.3) during anelastic relaxation on the shape of stress-strain curves. In addition, as those tests were performed at much larger stresses than in DMA and RUS, they can provide fundamental insight in the effect of the stresses on cubic-to-rhombohedral phase transformation discussed above.

Figure 5.3a shows stress-strain curves under three load-unload cycles between 50 MPa and 450 MPa in the temperature range of 25 – 550 °C. It indicates that the strain linearly increases with stress at room temperature. Loading and unloading curves overlap completely during three loading cycles and no stress-stain hysteresis was observed. With temperature increase, large hysteresis loops can be observed from 200 °C to 500 °C. Those loops are open in the first several loading cycles, and after that gradually closed in each subsequent loading cycle. To further investigate changes in stress-strain hysteresis loops in this temperature range, stress-strain curves during 15 load-unload cycles at 350 °C and 0.1 Hz loading frequency were recorded in Figure 5.3b. Figure 5.3c shows the opening of the loop, or permanent stain, after each loading

cycle. The residue strains greatly decrease with the increase of load-unload cycles, and eventually, approaching almost zero after three loading cycles. Above 450 °C, hysteresis loops gradually decrease with temperature increase until completely disappear around 500 °C.

When compared to the hysteresis loops in 8YSZ (see Section 4), SCSZ shows quite different hysteresis loops in 200 – 500 °C. In 8YSZ, closed hysteresis loops without residue strain after unloading were observed in the entire temperature range of 100 – 500 °C. The stress-strain curves in three subsequent load-unload cycles overlap and no residual strain or opening of the hysteresis loops was observed. SCSZ shows not only large residual strains, but also much larger hysteresis loops than those observed in YSZ.

To further study the hysteresis behavior, the change of secant modulus and energy dissipation with temperature was calculated based on results illustrated in Figure 5.3a and plotted in Figure 5.4a. Secant modulus shows nonlinear change with temperature and a minimum value around 450 °C, which is consistent with previous DMA and RUS results. Figure 5.4a also illustrates large energy dissipation peaks at 380 °C and 450 °C, which is compared to the mechanical damping of cubic SCSZ obtained by DMA and RUS in Figure 5.4b. The shape of energy dissipation vs. temperature curve is similar to the shape of mechanical damping vs. temperature curves in DMA and RUS tests, which suggests that hysteresis loops in SCSZ are the same as mechanical damping in DMA and RUS. Therefore, the small hysteresis loops and the energy dissipation observed in 200 – 300 °C for SCSZ may be attributed to the same

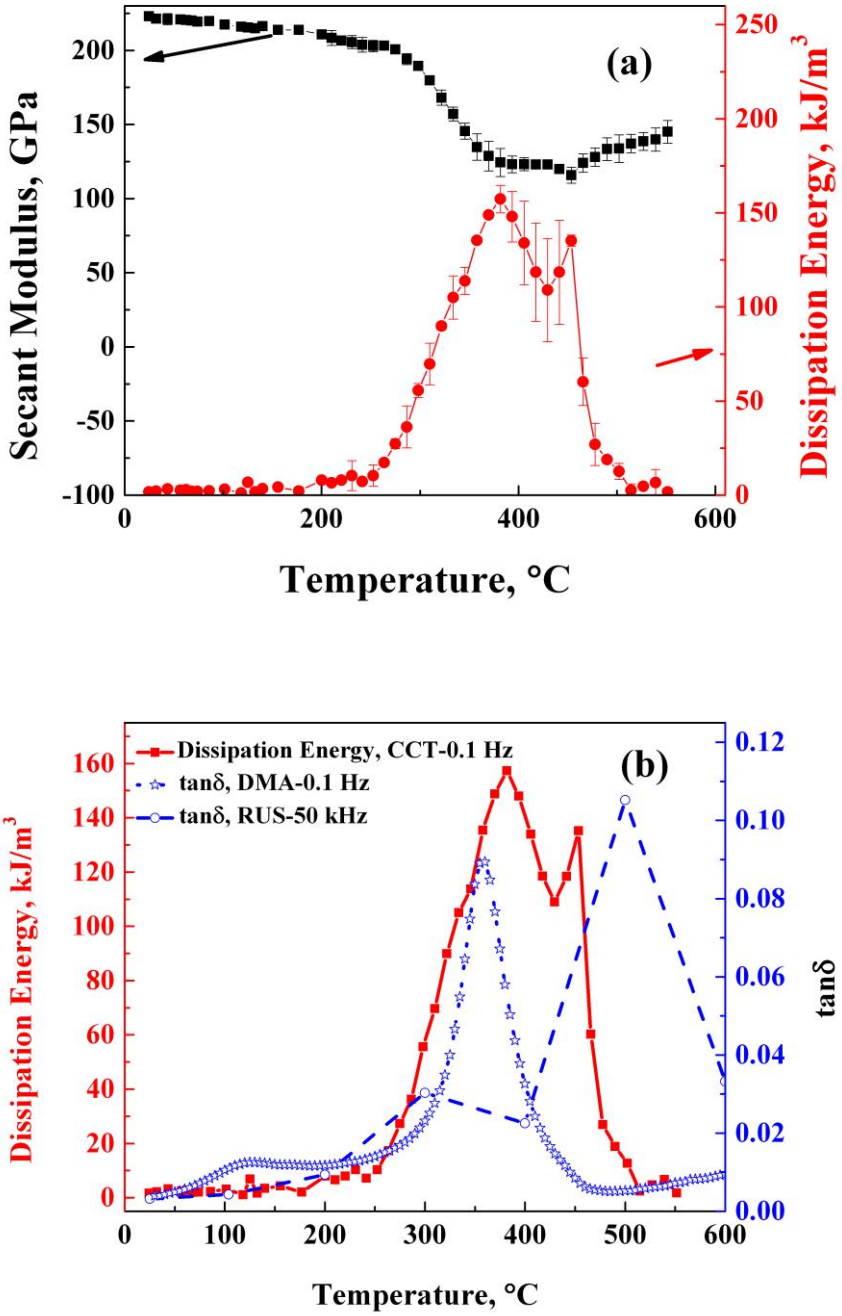

Figure 5.4. (a) The change of secant modulus and energy dissipation with temperature during the second load-unload cycle (b) comparison of energy dissipation vs. temperature from cyclic compression test and mechanical damping peaks from DMA and RUS.

mechanisms as in the first mechanical damping peak of DMA test, namely the reorientation of defect clusters and/or vacancy ordering [69]. In 300 – 500 °C, The most possible reason for the difference between SCSZ and YSZ is phase transformation that was observed in SCSZ, but not in YSZ. However, it cannot exclude some possible contribution of oxygen vacancy complexes, although it might be very small when compared to phase transformations. Above 500 °C, most of the structure is stable cubic with oxygen vacancies free and disassociated from complexes. Consequently, the hysteresis loops disappear at 500 °C.

The hysteresis loops between 300 °C and 500 °C recall hysteresis loops in ferroelastic materials. Several researchers noticed the ferroelasticity behavior in oxides, as it is discussed in more details in the previous section. One case is a tetragonal 3 mol% Y_2O_3 partially stabilized ZrO_2 (3Y-PSZ) under uniaxial stress. Baither et al. [218] observed the stress-strain ferroelastic of 3Y-PSZ in a uniaxial compression test. Cain et al. [151] concluded that the ferroelasticity in 3Y-PSZ was caused by the change of preferred orientation in the tetragonal structure. Aman et al. [195] studied the stress-strain hysteresis in $LaCoO_3$ perovskite by in-situ neutron diffraction and summarized that the preferred orientation and texture development contribute to the hysteresis loops. During the first load-unload cycle, a large hysteresis loop was observed due to recoverable domain reorientation and texturing; while residue strain (remnant strain) was the result of permanent alignment of some domains after the first loading cycle. They also observed smaller hysteresis loops after the first loading cycle. Although ferroelastic hysteresis observed in 300 – 500 °C for SCSZ, it is not related to the change in domain

orientation under stresses as in the previous two cases, the large differences between first and second load-unload cycle is still an evidence of ferroelastic behavior of SCSZ caused by stress induced phase transformation. The huge hysteresis loop and residue strain in the first load-unload cycle are the results of stress assisted phase transformation from cubic to rhombohedral. However, after the first loading cycle, much less cubic phase can transform to rhombohedral in each subsequent loading cycle leading to the smaller hysteresis loop and residue strain. With the increase in number of loading cycles up to the same amplitude stress, the fraction of phase transformed to rhombohedral decreases. Consequently, the size of hysteresis loops and residual strain decreases too. It is worth noting here that heating and loading history also might play a role in the hysteretic behavior. As it is shown, the fraction of phase transformed from cubic to rhombohedral at a constant temperature increases with annealing time. However, this transformation is very slow when compared since it takes up to 100 h to transform 60.05% of cubic to rhombohedral phases, while the duration of even 15 subsequent loading cycles as those shown in Figure 5.3b was only 2.5 minutes.

5.4.4 Electro-mechanical Coupling Behaviors

As previously mentioned in the introduction, dipoles, formed by point defects and catons such as $(Sc'_{Zr}V_O^{\bullet\bullet})^{\bullet}$, $(Zr_{Zr}^{x}V_O^{\bullet\bullet})^{\bullet\bullet}$ and $(2Sc'_{Zr}V_O^{\bullet\bullet})^{x}$, are elasto-electric dipoles, which mean they can be reoriented both by the stress and electric field. In author's previous work in Section 4, electro-mechanical coupling was observed in 8YSZ due to the reorientation of dipoles or local ordering oxygen vacancies complexes. A

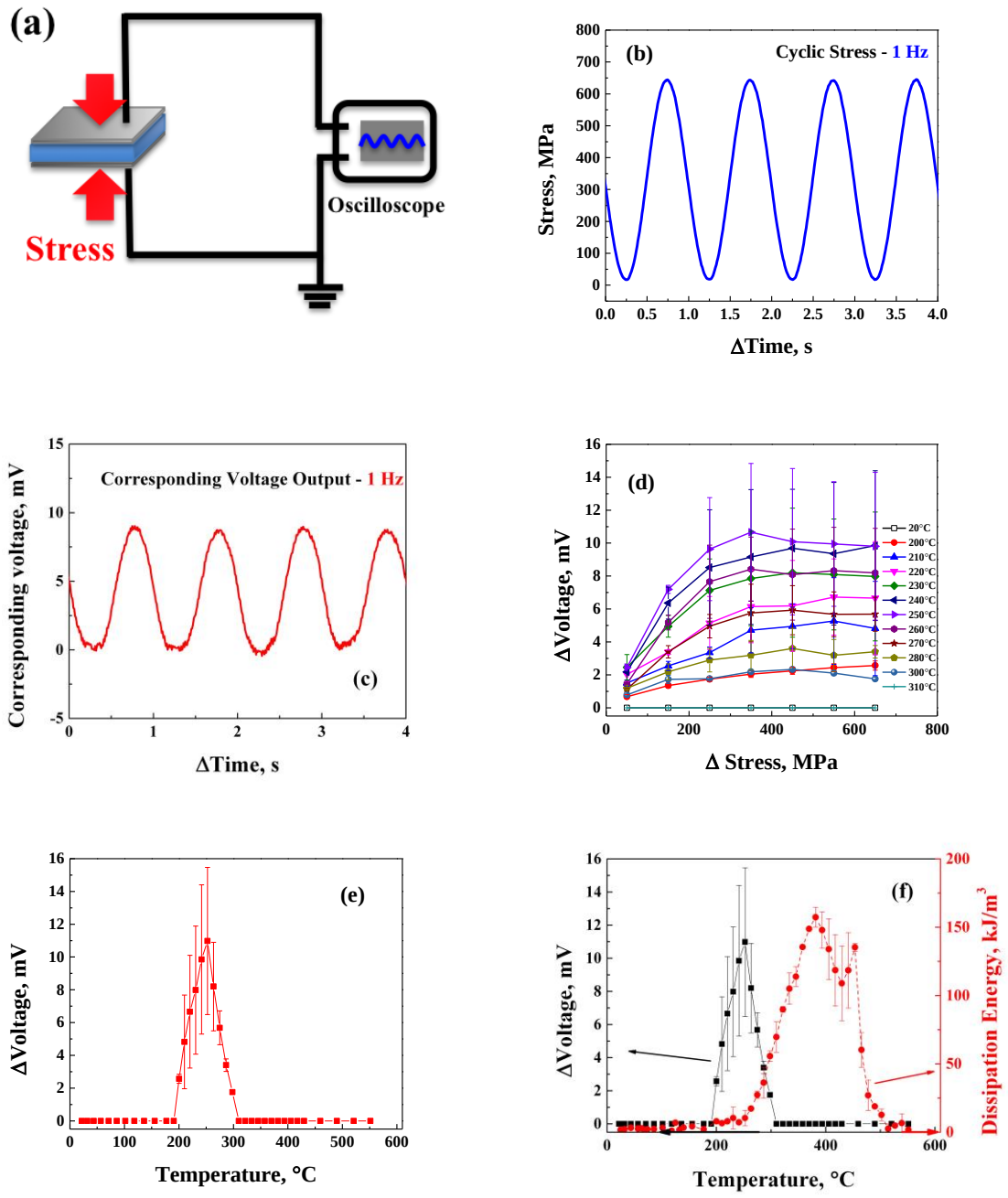

Figure 5.5. (a) Schematic of electro-mechanical coupling test setup (b) applied sinusoidal stress at 350°C with the frequency of 1 Hz (c) the corresponding voltage output of SCSZ vs. time under the applied sinusoid stress as shown in Figure 5.5b (d) the amplitude of voltage (ΔV) vs. the amplitude of applied compressive stress at 1 Hz at different temperatures (e) the Δvoltage vs. temperature of SCSZ under 5 − 650 MPa sinusoidal stress (f) the comparison of Δvoltage vs. temperature and energy dissipation vs. temperature in SCSZ.

corresponding open circuit voltage was measured by oscilloscope under sinusoidal compressive stress, as a result of the stress-induced polarization of YSZ. Ferroelectric hysteresis loops (P-E loops) at different temperatures under different stresses were found using a Sawyer-Tower method. Similarly as in 8YSZ, mechanical damping and energy dissipation peaks in SCSZ were observed due to the reorientation of oxygen vacancy complexes at lower temperatures using RUS (Section 2), DMA (Section 3) and CCT (this section). Corresponding voltage outputs under sinusoidal applied stresses were tested in SCSZ and the test setup is shown in Figure 5.5a.

Figure 5.5b and Figure 5.5c show the sinusoidal applied stress between 5 MPa and 650 MPa with the frequency of 1 Hz at 250 °C and its corresponding voltage output, respectively. Voltage output with time is also sinusoidal shape and shows the same frequency as the applied stress. The amplitude of open circuit voltage (amplitude = average maximum value - average minimum value) is around 9 mV. The voltage outputs were recorded at different stress amplitudes ($\Delta\sigma$) and temperatures with the frequency of 1 Hz shown in Figure 5.5d. Corresponding open circuit voltages were also measured in the temperature range of 200 – 300 °C. The open circuit voltage first quickly increases with the increasing amplitude stress and then, gradually approach to a certain value as most of the electro-elastic dipoles become aligned with applied stress. The calculated amplitudes of corresponding open circuit voltage were plotted vs. temperature from the room temperature to 550 °C under 5 – 650 MPa stresses with the frequency of 1 Hz in Figure 5.5e. The amplitudes of the open circuit voltage increase with temperature and

reach a maximum value at 250 °C. Above 250 °C, the value gradually reduce and reach to zero at 310 °C.

To further relate the observed peak in open circuit voltage to energy dissipation determined in CCT, they are compared in Figure 5.5e. As it can be seen in Figure 5.5f, the maximum open circuit voltage is at 250 °C well below the temperature of maximum energy dissipation due to phase transformations, i.e. 380 °C and 450 °C. However, it overlaps with a small mechanical damping peak observed at temperatures below Peaks 3 and 4 in Figure 3.12 that are related to the phase transformations. Therefore, the peak can be attributed to the reorientation of electro-elastic dipoles as it is discussed in Section 3.4.2 [69]. Moreover, ΔV increases with the applied stress (Figure 5.5d) suggesting that this reorientation mechanism is a stress dependent process. In addition, as it is discussed in more detail in Section 4, stable cubic structure 8YSZ shows similar dependence of ΔV on the applied stress amplitude. When compared with ΔV output in 8YSZ at the same temperatures, the signal in SCSZ is weaker. The latter is in good agreement with DMA and RUS results as they also show that mechanical damping in SCSZ is lower between room temperature and 300 °C (peak 1 and peak 2) when compared to 8YSZ. For the reasons discussed above, phase transformations does not cause the observed stress induced polarization, but rather the reorientation of elasto-electric dipoles, such as $(Sc'_{Zr}V_O^{\bullet\bullet})^{\bullet}$, $(Zr^x_{Zr}V_O^{\bullet\bullet})^{\bullet\bullet}$ and $(2Sc'_{Zr}V_O^{\bullet\bullet})^x$, and local ordering of oxygen complexes.

5.5 Conclusions

XRD results in this study showed that the cubic phase partially transforms to rhomboheral in SCSZ after annealing in the temperature range of 300 – 400 °C. The fraction of the SCSZ that is in the rhombohedral phase in annealed samples depends on the annealing temperature and time. A SCSZ structure with 60.05 % rhombodedral and 39.95 % cubic phase (two-phase SCSZ) was achieved after annealing for 100 hours at 350 °C. This structure was selected in further tests together with the pure cubic structure.

Results of Resonant Ultrasound Spectroscopy (RUS) showed abrupt decrease in elasrtic moduli of two-phase SCSZ around 510 °C as a result of the rhombohedral to cubic phase transformation. However, for cubic SCSZ, elastic moduli were found to decrease from 100 °C to 600 °C in a more gradual manner, due to (i) the anelastic relaxation of elastic dipoles in cubic structure, (ii) cubic to rhombohedral phase transformation at 300 °C and (iii) rhombohedral to cubic phase transformation around 500 °C.

Cyclic compression tests showed that the stress-strain behavior at room temperature is linear elastic. At temperatures between 200 °C and 300 °C, the small hysteresis loops are caused by the anelastic relaxation of dipoles and/or local ordering of oxygen vacancies. Between 300 °C and 500 °C, much larger stress–strain hysteresis loops were observed. Those loops are open having some residual (permanent) strain after each loading cycle. Stress induced phase transformation from cubic to rhombohedral at back to cubic was the main reason for appearance of those hysteresis loops. Above 500 °C, hysteresis loops disappear.

SCSZ also shows electro-mechanical coupling at temperatures at which the reorientation of dipoles or ordering is the main cause of the observed anelastic relaxation. An open circuit voltage was measured on the cubic SCSZ samples during cyclic loading in the 200 – 300 °C temperature range as a result of the stress induced polarization.

6. CONCLUSIONS AND FUTURE DIRECTIONS

In this study, the thermal, elastic and electro-mechanical properties of doped binary oxides DBOs with high ionic conductivity were investigated from room temperature to 1000 °C and the major results and findings can be summarized as follows:

1. The commercial powder of 8YSZ, 10YSZ, SCSZ, 10GDC and 20GDC were processed to be almost fully dense (relative density>95%) samples with around a 5 μm grain size. 8YSZ, 10YSZ, 10GDC and 20GDC were confirmed to have stable cubic structure by high temperature XRD in the entire temperature range of 20 – 800 °C. However, the cubic phase partially transformed to rhombohedral beginning at 300 °C, and then completely back to cubic around 500 °C in SCSZ. In addition, it was shown that the long term annealing of cubic SCSZ samples could result in the stabilization of the rhombohedral structure at room temperature. For example, SCSZ samples annealed at 350 °C for 100 hours have 60.05 vol% rhombohedral and 39.95 vol% cubic structure. YSZs, SCSZ and GDCs show almost the linear thermal expansion with increasing temperature. However, the instantaneous coefficient of thermal expansion (CTE) vs. temperature plots show a small change in the slope around 600 °C. Other than the reduction of Ce^{4+} to Ce^{3+} in GDCs and phase transformation in SCSZ, an order-disorder transition may also contribute to the increase of instantaneous CTE slope in all materials. The thermal expansion coefficient of YSZs and SCSZ

are similar, but much smaller than in GDCs. The study of thermal expansion is critical to the integrity of the layered structures in SOFCs.

2. The nonlinear changes of elastic moduli and large energy dissipation were observed in stabilized zirconias by DMA, RUS and cyclic compression tests. In doped cerias, the elastic moduli change almost linearly with temperature except in the 100 – 300 °C temperature range where a small deviation from the linear trend can be observed. In doped zirconias, much larger deviations from the linear decrease of elastic moduli with temperature were observed in the 100 – 600 °C temperature range. A further analysis of DMA, RUS and cyclic loading results suggested that the mechanisms responsible for the observed large mechanical damping and energy dissipation also result in the non-linear changes in elastic moduli with temperature.

3. Two frequency dependent relaxation peaks were observed in the YSZ: Peak 1 at lower temperature and Peak 2 at higher temperature. Both peaks were found to be frequency depended, i.e. maximum mechanical damping was observed at higher temperatures for higher frequencies, suggesting that mechanisms responsible for observed mechanical damping is thermally activated. Activation energies for different anelastic relaxation mechanisms were determined from DMA result to be around 1.2 eV and 2.7 eV for Peak 1 and Peak 2 respectively.

4. In-situ neutron diffraction showed no long-range phase transformation in 8YSZ under applied compressive stresses that might be responsible for the

observed mechanical damping. In addition, cyclic compression tests revealed large fully reversible stress-strain hysteresis loops in 8YSZ from 20 °C to 500 °C. The mechanical loss coefficient as a measure of the portion of deformation energy that is dissipated during mechanical was calculated for 8YSZ from cyclic compressive testing and found to be close to that of typical viscoelastic materials.

5. Spontaneous polarization under applied cyclic compressive stress was also observed in YSZ. The polarization was probably caused by the stress-induced reorientation of clusters such as $(Y'_{Zr}V_O^{\bullet\bullet})^{\bullet}$, $(Zr_{Zr}^{x}V_O^{\bullet\bullet})^{\bullet\bullet}$, or even more complex ones, that usually form at lower temperatures. Since those clusters are both elastic and electric dipoles (electro-elastic dipoles), their thermally activated reorientation under the stress by vacancy hopping to the preferential position causes spontaneous polarization.

6. Polarization vs. electric field plots were also generated for 8YSZ, under different stresses from room temperature to 450 °C. They show weak polarization loops at room temperatures, indicating some ferroelectric behavior. However, at 300 °C polarization loops are large and stress dependent. The maximum polarization was measured to be from 1.1 $\mu C/cm^2$ at 150 MPa to 3 $\mu C/cm^2$ at 300 and 450 MPa. The values of coercive field were found to be relatively low, from 1.4 kV/cm at 150 MPa to 2.6 kV/cm at 450 MPa. Although measured polarization is much lower than the typical value for polycrystalline PZT ceramics (about 30 $\mu C/cm^2$), it is still a valuable material for high temperature applications since the operating temperature of traditional

piezoelectric ceramics is below 200 °C. Those results, together with the results of spontaneous polarization, confirm the piezoelectric behavior of 8YSZ in the 100 – 500 °C temperature range.

7. Mechanical spectroscopy of cubic SCSZ and two-phase SCSZ revealed four mechanical damping peaks. Peak 1 with activation energy of 1.2 eV is probably caused by anelastic relaxation of simple dipoles similar as in YSZs. Peak 2 could not be fully analyzed from DMA results. The frequency dependent Peak 3 is found to be most likely due to stress-induced phase transformation from cubic to rhombohedral; while frequency independent Peak 4 is caused by phase transformation from rhombohedral to cubic.

8. Stress-strain hysteresis loops were also observed in SCSZ from 25 °C to 550 °C. The changes of secant modulus and energy dissipation with temperature were consistent with the change of storage modulus and mechanical damping from RUS and DMA. Compared to 8YSZ, much larger and open stress–strain hysteresis loops were observed between 200 °C and 500 °C. The hysteresis loops between 300 °C and 500 °C are mainly due to cubic to rhombohedral and back to cubic phase transformations. The reorientation of defect complexes contributes to the hysteresis in the temperature range of 200 – 300 °C. Above 450 °C, hysteresis loops gradually decrease, and finally, disappear around 500 °C.

9. Open circuit voltage was also detected on the SCSZ samples during cyclic compressive loading in 200 – 300 °C as a result of the stress induced

reorientation of electro-elastic dipoles.

To further elucidate relaxation mechanisms in doped ceria and zirconia ceramics, the following questions should be addressed in the future:

1. *What mechanisms cause two relaxation peaks in YSZ?* Some previous work suggest that two relaxation peaks are the consequence of anelastic relaxation of different type of complexes, such as $(Y'_{Zr}V_O^{\bullet\bullet})^{\bullet}$, $(Zr_{Zr}^{x}V_O^{\bullet\bullet})^{\bullet\bullet}$, $(2Y'_{Zr}V_O^{\bullet\bullet})^{\bullet}$ or even more complex clusters. Even more, our results show that the broadening of both obvious anelastic relaxation peaks is much larger than that predicted using single Debye model, suggesting multiple relaxation mechanisms with different relaxation times and activation energies. The latter might not be only the result of anelastic relaxation of different type of complexes, but also different types of anelastic relaxation, for example, by vacancy hopping in different crystallographic directions. Mechanical spectroscopy of single crystal YSZ samples with different orientation as well as computational modeling would help significantly in resolving this issue.

2. *What is the effect of the dopant size on the activation energy for anelastic relaxation?* Results presented in this work and some previously published studies suggest that activation energy for reorientation of vacancy-cation clusters depends on the size of cation/dopant. Therefore, the study of the anelastic relaxation oxides with fluorite structure doped with larger number of various aliovalent cations is needed to confirm this hypothesis. In addition,

computational models would help to answer this question much faster by looking at the broader range of dopants.

3. *How strong is electro-mechanical coupling in doped zirconia ceramics*? To characterize electro-mechanical coupling in doped zircons, more work is needed. Measurements of piezoelectric coefficient (d_{33}) at different temperatures, electrochemical impedance spectroscopy under applied stress, and measurements of electrostrictive coefficient at different conditions would help in a better understanding of this newly discovered phenomena.

REFERENCES

1. N. P. Padture, M. Gell, and E. H. Jordan. Thermal Barrier Coatings for Gas-Turbine Engine Applications, Science, **296**(2002) 280-284.
2. Advanced Dental Technology. Porcelain to Zirconia, http://www.adt-us.com/adt-fz--layered-zirconia.html.
3. S. Fischer, D. Schönauer-Kamin, R. Pohle, M. Fleischer, and R. Moos. NO Detection by Pulsed Polarization of Lambda Probes–Influence of the Reference Atmosphere, Sensors (Basel, Switzerland), **13**(2013) 16051-16064.
4. h2e Power Systems Inc. Solid Oxide Fuel Cells, http://h2epower.net/tech.html.
5. A. J. Moulson and J. M. Herbert. Electroceramics: materials, properties, and applications, 2003: Chichester ; Hoboken, NJ : Wiley.
6. P. Pandture, M. Gell, and E. H. Jordan. Thermal Barrier Coatings for Gas-Turbine Engine Applications, Science, **296** (2002) 280-284.
7. A. D. Bona, O. E. Pecho, and R. Alessandretti. Zirconia as a Dental Biomaterial, Materials, **8**(2015) 4978-4991.
8. R. Stevens and L. Magnesium Elektron. An Introduction to Zirconia, 1983: Magnesium Elektron Limited.
9. D. Ray. Characterization of 10MOL% Sc2O3-1MOL% CeO2-ZrO2 Ceramics as Electrolyte Material for Lower Temperature Solid Oxide Fuel Cells, 2007: North Carolina Agricultural and Technical State University.
10. M. Weller, B. Damson, and A. Lakki. Mechanical loss of cubic zirconia, Journal of Alloys and Compounds, **310**(2001) 47-53.

11. T. Settu. Characterisation of MgO–ZrO2 precursor powders prepared by in-situ peptisation of coprecipitated oxalate gel, Ceramics International, **26**(2000) 517-521.

12. A. G. Evans and R. M. Cannon. Overview no. 48, Acta Metallurgica, **34**(1986) 761-800.

13. D. L. Porter and A. H. Heuer. Mechanisms of toughening partially stabilized zirconia (PSZ), Journal of the American Ceramic Society, **60**(1977) 183-184.

14. S. Kim, S. Yamaguchi, and J. A. Elliott. Solid-State Ionics in the 21st Century: Current Status and Future Prospects, MRS Bulletin, **34**(2009) 900-906.

15. S. J. Skinner and J. A. Kilner. Oxygen ion conductors, Materials Today, **6**(2003) 30-37.

16. Y. Arachi, H. Sakai, O. Yamamoto, Y. Takeda, and N. Imanishai. Electrical conductivity of the ZrO2–Ln2O3 (Ln=lanthanides) system, Solid State Ionics, **121**(1999) 133-139.

17. S. Komine and F. Munakata. Dielectric relaxation analysis for 8 mol% YSZ single crystal, Journal of Materials Science, **40**(2005) 3887-3890.

18. I. R. Gibson and J. T. S. Irvine. Study of the order-disorder transition in yttria-stabilised zirconia by neutron diffraction, Journal of Materials Chemistry, **6**(1996) 895-898.

19. National Aeronautics and Space Administration. Solid Oxide Fuel Cells & Electrolysis Membranes, http://www.grc.nasa.gov/WWW/StructuresMaterials /Ceramics/research_solid.html.

20. N. Q. Minh and T. Takahashi. Science and Technology of Ceramic Fuel Cells 1995, Amsterdam: Elsevier, .

21. S. Singhal, S. C. Singhal, and K. Kendall. High-temperature Solid Oxide Fuel Cells: Fundamentals, Design and Applications: Fundamentals, Design and Applications, 2003: Elsevier Science.

22. P. Knauth and H. L. Tuller. Solid-State Ionics: Roots, Status, and Future Prospects, Journal of the American Ceramic Society, **85**(2002) 1654-1680.

23. K. Ukai, M. Yokoyama, J. Shimano, Y. Mizutani, and O. Yamamoto, An Overview of Scandia Stabilized Zirconia Electrolyte Development for SOFC Application, in Ceramic Materials and Components for Energy and Environmental Applications. 2010, John Wiley & Sons, Inc. 185-190.

24. H. G. Scott. Phase relationships in the zirconia-yttria system, Journal of Materials Science, **10**(1975) 1527-1535.

25. R. Ruh, H. J. Garrett, R. F. Domagala, and V. A. Patel. The System Zirconia-Scandia, Journal of the American Ceramic Society, **60**(1977) 399-403.

26. P. Christel, A. Meunier, M. Heller, J. P. Torre, and C. N. Peille. Mechanical properties and short-term in vivo evaluation of yttrium-oxide-partially-stabilized zirconia, Journal of Biomedical Materials Research, **23**(1989) 45-61.

27. M. Weller. Mechanical loss measurements on yttria- and calcia-stabilized zirconia, Journal of Alloys and Compounds, **211–212**(1994) 66-70.

28. O. Yamamoto. Solid oxide fuel cells: fundamental aspects and prospects, Electrochimica Acta, **45**(2000) 2423-2435.

29. H. Yamamura, N. Utsunomiya, T. Mori, and T. Atake. Electrical conductivity in the system ZrO2–Y2O3–Sc2O3, Solid State Ionics, **107**(1998) 185-189.

30. S. P. S. Badwal, F. T. Ciacchi, S. Rajendran, and J. Drennan. An investigation of conductivity, microstructure and stability of electrolyte compositions in the system 9 mol% (Sc2O3–Y2O3)–ZrO2(Al2O3), Solid State Ionics, **109**(1998) 167-186.

31. Y. Arachi, T. Asai, O. Yamamoto, Y. Takeda, N. Imanishi, K. Kawate, and C. Tamakoshi. Electrical Conductivity of ZrO2 - Sc2O3 Doped with HfO2, CeO2, and Ga2O3, Journal of the Electrochemical Society, **148**(2001) A520-A523.

32. T. Ishii. Structural phase transition and ionic conductivity in 0.88ZrO((2)-(0.12 − x))Sc2O(3-x)-Al2O3, Solid State Ionics, **78**(1995) 333-338.

33. K. Nomura, Y. Mizutani, M. Kawai, Y. Nakamura, and O. Yamamoto. Aging and Raman scattering study of scandia and yttria doped zirconia, Solid State Ionics, **132**(2000) 235-239.

34. Y. Mizutani, M. Kawai, K. Nomura, Y. Nakamura, and O. Yamamoto. Performance of Sc2O3-ZrO2 Electrolytes on Planar Solid Oxide Fuel Cell, Solid Oxide Fuel Cells V,(1997) 196-203.

35. Y. Mizutani, M. Tamura, M. Kawai, and O. Yamamoto. Development of high-performance electrolyte in SOFC, Solid State Ionics, **72, Part 2**(1994) 271-275.

36. M. Hirano, T. Oda, K. Ukai, and Y. Mizutani. Suppression of Rhombohedral-Phase Appearance and Low-Temperature Sintering of Scandia-Doped Cubic-Zirconia, Journal of the American Ceramic Society, **85**(2002) 1336-1338.

37. Z. Wang, M. Cheng, Z. Bi, Y. Dong, H. Zhang, J. Zhang, Z. Feng, and C. Li. Structure and impedance of ZrO2 doped with Sc2O3 and CeO2, Materials Letters, **59**(2005) 2579-2582.

38. D. S. Lee, W. S. Kim, S. H. Choi, J. Kim, H. W. Lee, and J. H. Lee. Characterization of ZrO2 co-doped with Sc2O3 and CeO2 electrolyte for the application of intermediate temperature SOFCs, Solid State Ionics, **176**(2005) 33-39.

39. M. Mogensen, N. M. Sammes, and G. A. Tompsett. Physical, chemical and electrochemical properties of pure and doped ceria, Solid State Ionics, **129**(2000) 63-94.

40. M. Gödickemeier and L. J. Gauckler. Engineering of Solid Oxide Fuel Cells with Ceria‐Based Electrolytes, Journal of The Electrochemical Society, **145**(1998) 414-421.

41. F. M. B. Marques and L. M. Navarro. Performance of double layer electrolyte cells Part I: Model behavior, Solid State Ionics, **90**(1996) 183-192.

42. A. Tsoga, A. Gupta, A. Naoumidis, and P. Nikolopoulos. Gadolinia-doped ceria and yttria stabilized zirconia interfaces: regarding their application for SOFC technology, Acta Materialia, **48**(2000) 4709-4714.

43. Y. Arachi, H. Sakai, O. Yamamoto, Y. Takeda, and N. Imanishai. Electrical conductivity of the ZrO2-Ln(2)O(3) (Ln = lanthanides) system, Solid State Ionics, **121**(1999) 133-139.

44. I. R. Gibson and J. T. S. Irvine. Study of the order-disorder transition in yttria-stabilised zirconia by neutron diffraction, Journal of Materials Chemistry, **6**(1996) 895-898.

45. F. A. Kroger, ed. The Chemistry of Imperfect Crystals. 2nd ed. 1974, North-Holland: Amsterdam.

46. H. Morikawa, Y. Shimizugawa, F. Marumo, T. Harasawa, H. Ikawa, K. Tohji, and Y. Udagawa. Local Structures Around Y Atoms in Y2O3-Stabilized Tetragonal ZrO2, Journal of the Ceramic Society of Japan, **96**(1988) 253-258.

47. M. H. Tuilier, J. Dexpert-Ghys, H. Dexpert, and P. Lagarde. X-ray absorption study of the ZrO2-Y2O3 system, Journal of Solid State Chemistry, **69**(1987) 153-161.

48. X. Li and B. Hafskjold. Molecular dynamics simulations of yttrium-stabilized zirconia, Journal of Physics: Condensed Matter, **7**(1995) 1255.

49. M. Ohta, K. Kirimoto, K. Nobugai, J. K. Wigmore, and T. Miyasato. Internal Friction Due to Localized Relaxation around Y-ions in Single Crystal Yttria-Stabilized Zirconia, 2001, Japanese Journal of Applied Physics Part 1-Regular Papers Brief Communications & Review Papers.

50. P. Li, I. W. Chen, and J. E. Penner-Hahn. X-ray-absorption studies of zirconia polymorphs. II. Effect of Y2O3 dopant on ZrO2 structure, Physical Review B, **48**(1993) 10074-10081.

51. M. Cole, C. R. A. Catlow, and J. P. Dragun. EXAFS studies of doped-ZrO2 systems, Journal of Physics and Chemistry of Solids, **51**(1990) 507-513.

52. C. R. A. Catlow, A. V. Chadwick, G. N. Greaves, and L. M. Moroney. EXAFS Study of Yttria-Stabilized Zirconia, Journal of the American Ceramic Society, **69**(1986) 272-277.

53. F. Shimojo, T. Okabe, F. Tachibana, M. Kobayashi, and H. Okazaki. Molecular Dynamics Studies of Yttria Stabilized Zirconia. I. Structure and Oxygen Diffusion, Journal of the Physical Society of Japan, **61**(1992) 2848-2857.

54. M. S. Khan, M. S. Islam, and D. R. Bates. Cation doping and oxygen diffusion in zirconia: A combined atomistic simulation and molecular dynamics study, Journal of Materials Chemistry, **8**(1998) 2299-2307.

55. T. Kushi, K. Sato, A. Unemoto, S. Hashimoto, K. Amezawa, and T. Kawada. Elastic modulus and internal friction of SOFC electrolytes at high temperatures under controlled atmospheres, Journal of Power Sources, **196**(2011) 7989-7993.

56. J. P. Goff, W. Hayes, S. Hull, M. T. Hutchings, and K. N. Clausen. Defect structure of yttria-stabilized zirconia and its influence on the ionic conductivity at elevated temperatures, Physical Review B, **59**(1999) 14202-14219.

57. A. Navrotsky. Thermodynamics of solid electrolytes and related oxide ceramics based on the fluorite structure, Journal of Materials Chemistry, **20**(2010) 10577-10587.

58. J. Kondoh, S. Kikuchi, Y. Tomii, and Y. Ito. Effect of Aging on Yttria‐Stabilized Zirconia: III. A Study of the Effect of Local Structures on Conductivity, Journal of the Electrochemical Society, **145**(1998) 1550-1560.

59. J. Kondoh, S. Kikuchi, Y. Tomii, and Y. Ito. Effect of Aging on Yttria - Stabilized Zirconia: II. A Study of the Effect of the Microstructure on Conductivity, Journal of the Electrochemical Society, **145**(1998) 1536-1550.

60. A. S. Nowick and B. S. Berry. Anelastic relaxation in crystalline solids 1972, New York: Academic press.

61. R. G. Breckenridge. Low Frequency Dispersion in Ionic Crystals, The Journal of Chemical Physics, **16**(1948) 959-967.

62. J. B. Wachtman. Mechanical and Electrical Relaxation in ThO2 Containing CaO, Physical Review, **131**(1963) 517-527.

63. M. Weller. Anelastic Relaxation of Point Defects in Cubic Crystals, J. Phys. IV France, **06**(1996) C8-63-C8-72.

64. A. Ovenston. Effect of atmosphere on the electrical properties of polycrystalline yttria-stabilised zirconia, Solid State Ionics, **58**(1992) 221-229.

65. Y. Chen and J. R. Sellar. Systematic study of dielectric and conductivity relaxations in yttriastabilised zirconia alloys at lower temperatures, Solid State Ionics, **86, Part 1**(1996) 207-211.

66. A. Pimenov, J. Ullrich, P. Lunkenheimer, A. Loidl, and C. H. Rüscher. Ionic conductivity and relaxations in ZrO2–Y2O3 solid solutions, Solid State Ionics, **109**(1998) 111-118.

67. M. Weller, R. Herzog, M. Kilo, G. Borchardt, S. Weber, and S. Scherrer. Oxygen mobility in yttria-doped zirconia studied by internal friction, electrical

conductivity and tracer diffusion experiments, Solid State Ionics, **175**(2004) 409-413.

68. A. Lakki, R. Herzog, M. Weller, H. Shubert, C. Reetz, O. Gorke, M. Kilo, and G. Borshardt. Mechanical loss, creep, diffusion and ionic conductivity of ZrO2-8 mol% Y2O2 polycrystals, Journal of the European Ceramic Society, **20**(2000) 285-296.

69. P. Gao, E. Lara-Curzio, R. Trejo, and M. Radovic. Dynamic Mechanical Analysis of Phase Transformations and Anelastic Relaxation in Stabilized Zirconias, Journal of the Electrochemical Society, **162**(2015) F14-F22.

70. M. Weller and A. Lakki. Defects in cubic zirconia studied by mechanical loss spectroscopy, Berichte Der Bunsen-Gesellschaft-Physical Chemistry Chemical Physics, **101**(1997) 1297-1302.

71. M. P. Anderson and A. S. Nowick. Relaxation Peaks Produced by Defect Complexes in Cerium Dioxide Doped with Trivalent Cations, Journal de physique. Colloque, **42**(1981) C5-822-C5-828.

72. J. Kondoh, H. Shiota, S. Kikuchi, Y. Tomii, Y. Ito, and K. Kawachi. Changes in Aging Behavior and Defect Structure of Y 2 O 3 Fully Stabilized ZrO2 by In2 O 3 Doping, Journal of the Electrochemical Society, **149**(2002) J59-J72.

73. M. Ohta, K. Kirimoto, K. Nobugai, J. K. Wigmore, and T. Miyasato. Localized relaxation in stabilized zirconia, Physica B: Condensed Matter, **316–317**(2002) 427-429.

74. M. Weller, F. Khelfaoui, M. Kilo, M. A. Taylor, C. Argirusis, and G. Borchardt. Defects and phase transitions in yttria- and scandia-doped zirconia, Solid State Ionics, **175**(2004) 329-333.

75. H. L. Tuller. Defect engineering: design tools for solid state electrochemical devices, Electrochimica Acta, **48**(2008) 2879-2887.

76. J. W. Fergus. Electrolytes for solid oxide fuel cells, Journal of Power Sources, **162**(2006) 30-40.

77. K. Eguchi, T. Setoguchi, T. Inoue, and H. Arai. Electrical properties of ceria-based oxides and their application to solid oxide fuel cells, Solid State Ionics, **52**(1992) 165-172.

78. H. Inaba and H. Tagawa. Ceria-based solid electrolytes, Solid State Ionics, **83**(1996) 1-16.

79. B. C. H. Steele. Appraisal of Ce1−yGdyO2−y/2 electrolytes for IT-SOFC operation at 500°C, Solid State Ionics, **129**(2000) 95-110.

80. H. Yahiro, K. Eguchi, and H. Arai. Electrical properties and reducibilities of ceria-rare earth oxide systems and their application to solid oxide fuel cell, Solid State Ionics, **36**(1989) 71-75.

81. V. Butler, C. R. A. Catlow, B. E. F. Fender, and J. H. Harding. Dopant ion radius and ionic-conductivity in cerium dioxide, Solid State Ionics, **8**(1983) 109-113.

82. R. Gerhardt-Anderson and A. S. Nowick. Ionic conductivity of CeO2 with trivalent dopants of different ionic radii, Solid State Ionics, **5**(1981) 547-550.

83. M. Radovic, E. Lara-Curzio, R. Trejo, B. Armstrong, and C. Walls. Elastic Properties, Equibiaxial Strength and Fracture Toughness of 8mol%YSZ Electrolyte for SOFC, in 28th Cocoa Beach Conference on Advanced Ceramics and Composites Ceramics. 2003. The American Ceramic Society

84. N. Orlovskaya, S. Lukich, G. Subhash, T. Graule, and J. Kublert. Mechanical properties of 10 mol% Sc2O3-1 mol% CeO2-89 mol% ZrO2 ceramics, Journal of Power Sources **195**(2010) 2774-2781.

85. C.-K. Lin, T.-T. Chen, Y.-P. Chyou, and L.-K. Chiang. Thermal stress analysis of a planar SOFC stack, Journal of Power Sources, **164**(2007) 238-251.

86. J. Laurencin, G. Delette, F. Lefebvre-Joud, and M. Dupeux. A numerical tool to estimate SOFC mechanical degradation: Case of the planar cell configuration, Journal of the European Ceramic Society, **28**(2008) 1857-1869.

87. A. Atkinson and A. Selçuk. Mechanical behaviour of ceramic oxygen ion-conducting membranes, Solid State Ionics, **134**(2000) 59-66.

88. S. R. Bishop, D. Marrocchelli, N. H. Perry, H. L. Tuller, G. Watson, B. Yildiz, K. Amezawa, and J. A. Kilner. Chemical Expansion in SOFC Materials: Ramifications, Origins, and Mitigation, ECS Transactions, **57**(2013) 643-648.

89. A. Atkinson and T. M. G. M. Ramos. Chemically-induced stresses in ceramic oxygen ion-conducting membranes, Solid State Ionics, **129**(2000) 259-269.

90. C. S. Montross, H. Yokokawa, and M. Dokiya. Thermal stresses in planar solid oxide fuel cells due to thermal expansion differences, British Ceramic Transactions, **101**(2002) 85-93.

91. D. L. Damm and A. G. Fedorov. Reduced-order transient thermal modeling for SOFC heating and cooling, Journal of Power Sources, **159**(2006) 956-967.

92. A. Nakajo, Z. Wuillemin, J. Van herle, and D. Favrat. Simulation of thermal stresses in anode-supported solid oxide fuel cell stacks. Part I: Probability of failure of the cells, Journal of Power Sources, **193**(2009) 203-215.

93. L.-K. Chiang, H.-C. Liu, Y.-H. Shiu, C.-H. Lee, and R.-Y. Lee. Thermo-electrochemical and thermal stress analysis for an anode-supported SOFC cell, Renewable Energy, **33**(2008) 2580-2588.

94. G. Anandakumar, N. Li, A. Verma, P. Singh, and J.-H. Kim. Thermal stress and probability of failure analyses of functionally graded solid oxide fuel cells, Journal of Power Sources, **195**(2010) 6659-6670.

95. E. Lara-Curzio, M. Radovic, and C. R. Luttrell, Applicability of Probabilistic Analyses to Assess the Structural Reliability of Materials and Components for Solid-Oxide Fuel Cells, in Engineered Ceramics. 2016, John Wiley & Sons, Inc. 46-58.

96. H. Yakabe, Y. Baba, T. Sakurai, and Y. Yoshitaka. Evaluation of the residual stress for anode-supported SOFCs, Journal of Power Sources **135** (2004) 9-16.

97. W. Fischer, J. Malzebender, G. Blass, and R. W. Steinbrech. Residual stresses in planar solid oxide fuel cells Journal Of Power Sources, **150**(2005) 73-77.

98. A. Atkinson and A. Selcuk. Residual stresses and fracture of laminated ceramic membranes, Acta Materialia, **47**(1999) 867-874.

99. H. Chen, X. Zhou, and C. Ding. Investigation of the thermomechanical properties of a plasma-sprayed nanostructured zirconia coating, Journal of the European Ceramic Society, **23**(2003) 1449-1455.

100. V. Gorelov, V. Balakireva, I. Yaroslavtsev, V. Kazantsev, and E. Vaganov. Conductivity and thermal expansion of the Ce0.8Gd0.2O1.9 solid electrolyte in the oxidizing and reducing atmospheres, Russian Journal of Electrochemistry, **43**(2007) 888-893.

101. H. Hayashi, M. Kanoh, C. J. Quan, H. Inaba, S. Wang, M. Dokiya, and H. Tagawa. Thermal expansion of Gd-doped ceria and reduced ceria, Solid State Ionics, **132**(2000) 227-233.

102. H. Hayashi, T. Saitou, N. Maruyama, H. Inaba, K. Kawamura, and M. Mori. Thermal expansion coefficient of yttria stabilized zirconia for various yttria contents, Solid State Ionics, **176**(2005) 613-619.

103. D. Marrocchelli, S. R. Bishop, H. L. Tuller, and B. Yildiz. Understanding Chemical Expansion in Non-Stoichiometric Oxides: Ceria and Zirconia Case Studies, Advanced Functional Materials, **22**(2012) 1958-1965.

104. S. R. Bishop, D. Marrocchelli, C. Chatzichristodoulou, N. H. Perry, M. B. Mogensen, H. L. Tuller, and E. D. Wachsman. Chemical Expansion: Implications for Electrochemical Energy Storage and Conversion Devices, Annual Review of Materials Research, **44**(2014) 205-239.

105. M. Radovic, E. Lara-Curzio, and G. Nelson. Fracture toughness and slow crack growth behavior of Ni-YSZ and YSZ as a function of porosity and temperature,

in Proceedings of The 30th Annual International Conference on Advanced Ceramics and Composites. 2006. Cocoa Beach.

106. R. Gerhardt, W. K. Lee, and A. S. Nowick. Anelastic and Dielectric-Relaxation of Scandia-Doped Ceria, Journal of Physics and Chemistry of Solids, **48**(1987) 563-569.

107. K. W. Lay and D. H. Whitmore. Dielectric and Anelastic Relaxation in Ca-Doped Cerium Dioxide, physica status solidi (b), **43**(1971) 175-190.

108. A. S. Nowick. Dielectric and Anelastic Relaxation of Crystals Containning Point Defects. II, (1967).

109. S. Komine. Anisotropic dielectric properties in Y2O3-stabilized ZrO2, Solid State Ionics, **178**(2007) 315-318.

110. A. Lashtabeg and S. J. Skinner. Solid oxide fuel cells—a challenge for materials chemists?, Journal of Materials Chemistry, **16**(2006) 3161-3170.

111. A. Rothschild and H. L.Tuller. Gas sensors: New materials and processing approaches, Journal of Elecroceramics, **17**(2006) 1005–1012.

112. E. Ivers-Tiffee, A. Weber, and D. Herbstritt. Materials and technologies for SOFC-components, Journal of the European Ceramic Society, **21**(2001) 1805-1811.

113. B. C. Steele. Ceramic ion conducting membranes, Current Opinion in Solid State and Materials Science, **1**(1996) 684-691.

114. O. T. Soresen, ed. Nonstociometric Oxides. 1981, Academic Press: New York.

115. O. Yamamoto, Y. Arati, Y. Takeda, N. Imanishi, Y. Mizutani, M. Kawai, and Y. Nakamura. Electrical conductivity of stabilized zirconia with ytterbia and scandia, Solid State Ionics, **79**(1995) 137-142.

116. B. Jaffe. Piezoelectric ceramics, 2012: Elsevier.

117. D. Dragan. Ferroelectric, dielectric and piezoelectric properties of ferroelectric thin films and ceramics, Reports on Progress in Physics, **61**(1998) 1267-1324.

118. H. Yang, C. Zhou, X. Liu, Q. Zhou, G. Chen, W. Li, and H. Wang. Piezoelectric properties and temperature stabilities of Mn- and Cu-modified BiFeO3–BaTiO3 high temperature ceramics, Journal of the European Ceramic Society, **33**(2013) 1177-1183.

119. O. L. Serhiy and E. E. Richard. Progress in engineering high strain lead-free piezoelectric ceramics, Science and Technology of Advanced Materials, **11**(2010) 044302, 1-13.

120. E. E. Richard , A. R. Clive , R. S. Thomas , and P. Seung-Eek. Preparation and Characterization of High Temperature Perovskite Ferroelectrics in the Solid-Solution (1- x)BiScO 3 – x PbTiO 3, Japanese Journal of Applied Physics, **41**(2002) 2099-2104.

121. D. Damjanovic. Materials for high temperature piezoelectric transducers, Current Opinion in Solid State and Materials Science, **3**(1998) 469-473.

122. Y. Guo, K.-i. Guo, H. Kakimoto, and Ohsato. Phase transitional behavior and piezoelectric properties of (Na0.5K0.5)NbO3–LiNbO3 ceramics, Applied physics letters, **85**(2004) 4121-4123.

123. X. N. Jiang, K. Kim, S. J. Zhang, J. Johnson, and G. Salazar. High-Temperature Piezoelectric Sensing, 2014: SENSORS.

124. P. Li, I. W. Chen, and J. E. Penner-Hahn. X-ray-absorption studies of zirconia polymorphs. II. Effect of Y2O3 dopant on ZrO2 structure, Physical Review B, **48**(1993) 10074-10081.

125. L. J. Gauckler, D. Beckel, B. E. Buergler, E. Jud, U. P. Muecke, M. Prestat, J. L. M. Rupp, and J. Richter. Solid Oxide Fuel Cells: Systems and Materials, CHIMIA International Journal for Chemistry, **58**(2004) 837-850.

126. J. P. P. Huijsmans, F. P. F. van Berkel, and G. M. Christie. Intermediate temperature SOFC – a promise for the 21st century, Journal of Power Sources, **71**(1998) 107-110.

127. N. Q. Minh, Centenary of Nernst′ s Discovery of Zirconia Electrolytes - Review of Zirconia-Based Electrochemical Technologies, in *International symposium; 6th, Solid oxide fuel cells*. 1999, Electrochemical Society: Honolulu, HI. p. 127-134.

128. K. Kanamura, S. Yoshioka, and Z.-i. Takehara. The Calculation of Temperature and Thermal Stress Distributions in the Planar Solid Oxide Fuel Cell, Bulletin of the Chemical Society of Japan, **65**(1992) 309-313.

129. Sergey Yarmolenko, Jag Sankar, Nicholas Bernier, Michael Klimov, Jay Kapat, and N. Orlovskaya. Phase Stability and Sintering Behavior of 10 mol% Sc2O3-1 mol %CeO2-ZrO2 Ceramics, Journal of Fuel Cell Science and Technology, **6**(2009) 021007: 1-8.

130. S. R. Bishop, H. L. Tuller, Y. Kuru, and B. Yildiz. Chemical expansion of nonstoichiometric $Pr_{0.1}Ce_{0.9}O_{2-\delta}$: Correlation with defect equilibrium model, Journal of the European Ceramic Society, **31**(2011) 2351-2356.

131. Y. Kuru, S. R. Bishop, J.-J. Kim, B. Yildiz, and H. L. Tuller. Chemical Expansion and Frozen-In Oxygen Vacancies in Pr-Doped Ceria, ECS Transactions, **35**(2011) 1131-1136.

132. ASTM standard C20-00, 2005: ASTM International.

133. ASTM Standard E83, Standard Test Method for Linear Thermal Expansion of Solid Materials by Thermomechanical Analysis 2009: ASTM International.

134. M. Radovic, E. Lara-Curzio, and L. Rieser. Comparison of different experimental techniques for determination of elastic properties of solids, Materials Science and Engineering A, **368**(2004) 56-70.

135. A. Migliori and J. L. Sarrao. Resonant Ultrasound Spectroscopy: Applications to Physics, Materials Measurements and Nondestructive Evaluation, 1997, New York: John Wiley and Sons.

136. M. Radovic, M. W. Barsoum, A. Ganguly, T. Zhen, P. Finkel, S. R. Kalidindi, and E. Lara-Curzio. On the elastic properties and mechanical damping of Ti_3SiC_2, Ti_3GeC_2, $Ti_3Si_{0.5}Al_{0.5}C_2$ and Ti_2AlC, in the 300-1573 K temperature range, Acta Materialia, **54**(2006) 2757-2767.

137. M. Radovic and E. Lara-Curzio. Mechanical properties of tape cast nickel-based anode materials for solid oxide fuel cells before and after reduction in hydrogen, Acta Materialia, **52**(2004) 5747-5756.

138. A. Zevalkink, A. Hunter, M. Swanson, C. Johnson, J. Kapat, and N. Orlovskaya. Processing and Characterization of Sc2O3-CeO2-ZrO2 Electrolyte Based Intermediate Temperature Solid Oxide Fuel Cells, in 2006 Materials Research Society Fall Meeting. 2007.

139. C. Peters, A. Weber, B. Butz, D. Gerthsen, and E. Ivers-Tiffée. Grain-Size Effects in YSZ Thin-Film Electrolytes, Journal of the American Ceramic Society, **92**(2009) 2017-2024.

140. D. Yarmolenko, D. Ray, J. Pai, and Sankar. Phase Transitions and Thermal Expansion of 10mol%Sc2O3-1mol% CeO2-ZrO2 Ceramics, Volume 3: Design and Manufacturing,(2007) 305-311.

141. P. K. Schelling, S. R. Phillpot, and D. Wolf. Mechanism of the Cubic-to-Tetragonal Phase Transition in Zirconia and Yttria-Stabilized Zirconia by Molecular-Dynamics Simulation, Journal of the American Ceramic Society, **84**(2001) 1609-1619.

142. A. Hara, Y. Hirata, S. Sameshima, N. Matsunaga, and T. Horita. Grain size dependence of electrical properties of Gd-doped ceria, Journal of the Ceramic Society of Japan, **116**(2008) 291-297.

143. G. M. Christie and F. P. F. van Berkel. Microstructure — ionic conductivity relationships in ceria-gadolinia electrolytes, Solid State Ionics, **83**(1996) 17-27.

144. N. M. Sammes and Y. Du. Fabrication and Characterization of Tubular Solid Oxide Fuel Cells, International Journal of Applied Ceramic Technology, **4**(2007) 89-102.

145. M. Mori, T. Yamamoto, H. Itoh, H. Inaba, and H. Tagawa. Thermal expansion of nickel-zirconia anodes in solid oxide fuel cells during fabrication and operation, Journal Name: Journal of the Electrochemical Society; Journal Volume: 145; Journal Issue: 4; Other Information: PBD: Apr 1998,(1998) Medium: X; Size: pp. 1374-1380.

146. S. Wang, M. Katsuki, T. Hashimoto, and M. Dokiya. Expansion Behavior of $Ce1-yGdyO2.0-0.5y-\delta$ under Various Oxygen Partial Pressures Evaluated by HTXRD, Journal of the Electrochemical Society, **150**(2003) A952-A958.

147. D. Marrocchelli, S. R. Bishop, H. L. Tuller, G. W. Watson, and B. Yildiz. Charge localization increases chemical expansion in cerium-based oxides, Physical Chemistry Chemical Physics, **14**(2012) 12070-12074.

148. M. Radovic, E. Lara-Curzio, R. Trejo, B. Armstrong, and C. Walls. Elastic properties, equibiaxial strength and fracture toughness of 8mol%YSZ electrolyte for SOFC, in 28th Cocoa Beach Conference on Advanced Ceramics and Composites Ceramics. 2005.

149. Q. Fang, T. Liu, C. Li, X. Wang, and G. Zhang. Damping mechanisms in oxide materials and their potential application, Key Engineering Materials, **319**(2006) 167-172.

150. M. Yashima, M. Kakihana, and M. Yoshimura. Metastable-stable phase diagrams in the zirconia-containing systems utilized in solid-oxide fuel cell application, Solid State Ionics, **86–88**(1996) 1131-1149.

151. M. G. Cain, M. H. Lewis, M. Backshall, S. M. Bennington, and S. Hull. The Ferroelastic Transformation in Yttria- and Ceria-Stabilised Tetragonal Zirconia Via Neutron Diffraction, MRS Proceedings, **376**(1994) 615.

152. J. Cai, C. Raptis, Y. S. Raptis, and E. Anastassakis. Temperature dependence of Raman scattering in stabilized cubic zirconia, Physical Review B, **51**(1995) 201-209.

153. S. Lukich, C. Carpenter, and N. Orlovskaya. Temperature and stress induced changes of the vibrational response of cubic and rhombohedral 10 mol%Sc2O3-1 mol%CeO2-ZrO2 ceramics, Journal of Power Sources, **195**(2010) 2301-2309.

154. A. Selçuk and A. Atkinson. Elastic properties of ceramic oxides used in solid oxide fuel cells (SOFC), Journal of the European Ceramic Society, **17**(1997) 1523-1532.

155. K. Matsushita. Internal-friction in Ceria Ceramics Doped with Alkali-earth Metal-oxides, Journal of Alloys and Compounds,, **211/212**(1994) 374-377.

156. R. Gerhardtanderson, F. Zamaninoor, A. S. Nowick, C. R. A. Catlow, and A. N. Cormack. Study of Sc2O3-doped Ceria by Anelastic Relaxation, Solid State Ionics, **9-10**(1983) 931-936.

157. J. Kondoh, T. Kawashima, S. Kikuchi, Y. Tomii, and Y. Ito. Effect of Aging on Yttria‐Stabilized Zirconia: I. A Study of Its Electrochemical Properties, Journal of the Electrochemical Society, **145**(1998) 1527-1536.

158. K. Jun-ichi, Y. Yuhji, S. Miwa, and Y. Hiroshi. Oxide-ion conduction and dielectric relaxation in the fluorite-type Zr 0.8 Ln 0.2 O 1.9 (Ln = Nd, Sm, Eu,

Gd, Dy, Ho, Er, Tm, Yb, Lu) system, IOP Conference Series: Materials Science and Engineering, **18**(2011) 132010:1-4.

159. A. S. Nowick and W. R. Heller. Dielectric and anelastic relaxation of crystals containing point defects, Advances in Physics, **14**(1965) 101-166.

160. R. Gerhardt. Impedance and dielectric spectroscopy revisited: Distinguishing localized relaxation from long-range conductivity, Journal of Physics and Chemistry of Solids, **55**(1994) 1491-1506.

161. N. Orlovskaya, S. Lukich, G. Subhash, T. Graule, and J. Kuebler. Mechanical properties of 10mol% Sc2O3–1mol% CeO2–89mol% ZrO2 ceramics, Journal of Power Sources, **195**(2010) 2774-2781.

162. K. P. Menard. Dynamic mechanical analysis : a practical introduction, 2008, Boca Raton, Fla.: Boca Raton, Fla. : CRC Press.

163. Dynamic Mechanical Analyzer-Q series User Manual, 2004: TA Instruments-Waters LLC.

164. RSA Ⅲ Rheometrics System Analyzer-Rheometric Series User Manual, 2005: TA Instruments-Water LLC.

165. P. Gudlur, A. Forness, J. Lentz, M. Radovic, and A. Muliana. Thermal and mechanical properties of Al/Al2O3 composites at elevated temperatures, Materials Science and Engineering: A, **531**(2012) 18-27.

166. R. Schaller, G. Fantozzi, and G. Gremaud, eds. Mechanical Spectroscopy Q-1 2001. 2001, Trans Tech Publications Ltd: Zuerich.

167. R. Gerhardt-Anderson, F. Zamani-Noor, A. S. Nowick, C. R. A. Catlow, and A. N. Cormack. Study of Sc2O3-doped ceria by anelastic relaxation, Solid State Ionics, **9–10, Part 2**(1983) 931-936.

168. F. Cordero, A. Franco, V. R. Calderone, P. Nanni, and V. Buscaglia. Anelastic spectroscopy for studying O vacancies in perovskites, Journal of the European Ceramic Society, **26**(2006) 2923–2929.

169. J. B. Wachtman, Jr., W. E. Tefft, D. G. Lam, Jr., and C. S. Apstein. Exponential Temperature Dependence of Young's Modulus for Several Oxides, Physical Review, **122**(1961) 1754-1759.

170. S. Yarmolenko, J. Sankar, N. Bernier, M. Klimov, J. Kapat, and N. Orlovskaya. Phase Stability and Sintering Behavior of 10 mol % Sc2O3-1 mol %CeO2-ZrO2 Ceramics Journal of fuel cell science and technology, **6**(2009) 021007: 1-8.

171. M. F. Ashby. Overview No. 80: On the engineering properties of materials, Acta Metallurgica, **37**(1989) 1273-1293.

172. H. L. Tuller and S. R. Bishop. Point Defects in Oxides: Tailoring Materials Through Defect Engineering, Annual Review of Materials Research, **41**(2011) 369-398.

173. I. R. Gibson and J. T. S. Irvine. Study of the order-disorder transition in yttria-stabilised zirconia by neutron diffraction, J . Mater. Chem, **6**(1996) 895-898

174. R. Ramamoorthy, P. K. Dutta, and S. A. Akbar. Oxygen sensors: Materials, methods, designs and applications, Journal of Materials Science, **38**(2003) 4271-4282.

175. K. An, H. Skorpenske, A. Stoica, D. Ma, X.-L. Wang, and E. Cakmak. First In Situ Lattice Strains Measurements Under Load at VULCAN, Metallurgical and Materials Transactions A, **42**(2011) 95-99.

176. A. C. Larson and R. B. V. Dreele. General Structure Analysis System (GSAS), Los Alamos National Laboratory Report LAUR 86-748,(2004).

177. K. An. VDRIVE- Data Reduction and Interactive Visualization Software for Event Mode Neutron Diffraction, ORNL Report, Oak Ridge National Laboratory, ORNL-TM-2012-621,(2012).

178. R. Schaller, G. Fantozzi, and G. Gremaud. Mechanical spectroscopy Q-¹ 2001 : with applications to materials science, 2001: Zuerich-Uetikon, Switzerland.

179. E. K. H. Salje, A. Graeme‐Barber, M. A. Carpenter, and U. Bismayer. Lattice parameters, spontaneous strain and phase transitions in Pb3(PO4)2, Acta Crystallographica Section B, **49**(1993) 387-392.

180. C. H. Kim, J. W. Jang, S. Y. Cho, I. T. Kim, and K. S. Hong. Ferroelastic twins in LaAlO3 polycrystals, Physica B: Condensed Matter, **262**(1999) 438-443.

181. J. Muñoz-Saldaña, G. A. Schneider, and L. M. Eng. Stress induced movement of ferroelastic domain walls in BaTiO3 single crystals evaluated by scanning force microscopy, Surface Science, **480**(2001) L402-L410.

182. C. Boulesteix, B. Yangui, G. Nihoul, and A. Bourret. High resolution and conventional electron microscopy studies of repeated wedge microtwins in monoclinic rare earth sesquioxides, Journal of Microscopy, **129**(1983) 315-326.

183. E. K. H. Salje. Ferroelasticity, Contemporary Physics, **41**(2000) 79-91.

184. E. K. H. Salje. Ferroelastic Materials, Annual Review of Materials Research, **42**(2012) 265-283.

185. E. K. H. Salje. Phase transitions in ferroelastic and co-elastic crystals : an introduction for mineralogists, material scientists, and physicists, 1990: New York : Cambridge University Press.

186. M. F. Ashby. Materials selection in mechanical design. 4th ed. Michael F. Ashby, 2011: Burlington, MA : Butterworth-Heinemann.

187. A. Lai, Z. Du, C. L. Gan, and C. A. Schuh. Shape Memory and Superelastic Ceramics at Small Scales, Science, **341**(2013) 1505-1508.

188. M. V. Swain. Shape memory behaviour in partially stabilized zirconia ceramics, Nature, **322**(1986) 234-236.

189. M. Mamivand, M. Asle Zaeem, and H. El Kadiri. Shape memory effect and pseudoelasticity behavior in tetragonal zirconia polycrystals: A phase field study, International Journal of Plasticity, **60**(2014) 71-86.

190. R. H. J. Hannink, P. M. Kelly, and B. C. Muddle. Transformation toughening in zirconia-containing ceramics, Journal of the American Ceramic Society, **83**(2000) 461-487.

191. P. E. Reyes-Morel and I. W. Chen. Transformation Plasticity of CeO2-Stabilized Tetragonal Zirconia Polycrystals: I, Stress Assistance and Autocatalysis, Journal of the American Ceramic Society, **71**(1988) 343-353.

192. D. Baither, M. Bartsch, B. Baufeld, A. Tikhonovsky, A. Foitzik, M. Rühle, and U. Messerschmidt. Ferroelastic and Plastic Deformation of t′ -Zirconia Single Crystals, Journal of the American Ceramic Society, **84**(2001) 1755-1762.

193. B. Butz, P. Kruse, H. Störmer, D. Gerthsen, A. Müller, A. Weber, and E. Ivers-Tiffée. Correlation between microstructure and degradation in conductivity for cubic Y2O3-doped ZrO2, Solid State Ionics, **177**(2006) 3275-3284.

194. F. T. Ciacchi, S. P. S. Badwal, and J. Drennan. The system Y2O3-Sc2O3-ZrO2: Phase characterisation by XRD, TEM and optical microscopy, Journal of the European Ceramic Society, **7**(1991) 185-195.

195. A. Aman, Y. Chen, M. Lugovy, N. Orlovskaya, M. J. Reece, D. Ma, A. D. Stoica, and K. An. In-situ neutron diffraction of LaCoO3 perovskite under uniaxial compression. I. Crystal structure analysis and texture development, Journal of Applied Physics, **116**(2014) 013503: 1-10.

196. D. Damjanovic. Ferroelectric, dielectric and piezoelectric properties of ferroelectric thin films and ceramics, Reports on Progress in Physics, **61**(1998) 1267-1324.

197. B. Jaffe. Piezoelectric ceramics, 2012: Elsevier.

198. J. F. Nye. Physical properties of crystals: their representation by tensors and matrices, 1985: Oxford university press.

199. R. Korobko, A. Patlolla, A. Kossoy, E. Wachtel, H. L. Tuller, A. I. Frenkel, and I. Lubomirsky. Giant Electrostriction in Gd-Doped Ceria, Advanced Materials, **24**(2012) 5857-5861.

200. D. Damjanovic. Hysteresis in piezoelectric and ferroelectric materials, The science of hysteresis, **3**(2006) 337-465.

201. B. Jaffe, W. Cook, and H. Jaffe, Piezoelectric Ceramics. 1971, Academic Press, New York and London.

202. J. Rödel, W. Jo, K. T. P. Seifert, E.-M. Anton, T. Granzow, and D. Damjanovic. Perspective on the Development of Lead-free Piezoceramics, Journal of the American Ceramic Society, **92**(2009) 1153-1177.

203. J. F. Shackelford and R. H. Doremus. Ceramic and glass materials : structure, properties and processing, 2008: New York : Springer.

204. S. Sinhal and K. Kendall, eds. High Temperature Solid Oxide Fuel Cells: Fundamentals, Design and Applications. 2003, Elsevier: Oxford.

205. S. P. S. Badwal and F. T. Ciacchi. Oxygen-ion conducting electrolyte materials for solid oxide fuel cells, Ionics, **6**(2000) 1-21.

206. C. Haering, A. Roosen, H. Schichl, and M. Schnöller. Degradation of the electrical conductivity in stabilised zirconia system: Part II: Scandia-stabilised zirconia, Solid State Ionics, **176**(2005) 261-268.

207. R. Chiba, F. Yoshimura, J. Yamaki, T. Ishii, T. Yonezawa, and K. Endou. Ionic conductivity and morphology in Sc2O3 and Al2O3 doped ZrO2 films prepared by the sol–gel method, Solid State Ionics, **104**(1997) 259-266.

208. Z. Lei and Q. Zhu. Phase transformation and low temperature sintering of manganese oxide and scandia co-doped zirconia, Materials Letters, **61**(2007) 1311-1314.

209. T. J. Bastow, T. Mathews, and J. R. Sellar. Al2O3 solubility in the fast ion conductor 0.88ZrO2–(0.12−x)Sc2O3–xAl2O3 determined by 27Al NMR, Solid State Ionics, **175**(2004) 415-417.

210. K. Ukai, M. Yokoyamall, J. Shimano, Y. Mizutani, and O. Yamamoto. An Overview of Scandia Stabilized Zirconia Electrolyte Development for SOFC Application, Ceramic Materials and Components for Energy and Environmental Applications: Ceramic Transactions, **210**(2010) 185-190.

211. S. Omar, W. Bin Najib, W. Chen, and N. Bonanos. Electrical Conductivity of 10 mol% Sc2O3–1 mol% M2O3–ZrO2 Ceramics, Journal of the American Ceramic Society, **95**(2012) 1965-1972.

212. S. Lukich, C. Carpenter, and N. Orlovskaya. Temperature and stress induced changes of the vibrational response of cubic and rhombohedral 10 mol%Sc2O3–1 mol%CeO2–ZrO2 ceramics, Journal of Power Sources, **195**(2010) 2301-2309.

213. M. Weller, F. Khelfaouia, M. Kilob, M. A. Taylorb, C. Argirusisb, and G. Borchardtb. Defects and phase transitions in yttria- and scandia-doped zirconia, Solid State Ionics, **175**(2004) 329–333.

214. S. Omar and N. Bonanos. Ionic conductivity ageing behaviour of 10 mol.% Sc2O3–1 mol.% CeO2–ZrO2 ceramics, Journal of Materials Science, **45**(2010) 6406-6410.

215. M. Mori and T. Itoh. Long Annealing Effect on Stabilities for Electrical Conductivity of (ZrO2)0.89(Sc2O3)0.1(CeO2)0.01 Electrolyte at IT-SOFC Operating Temperature, ECS Transactions, **57**(2013) 1107-1114.

216. A. S. Nowick. Kinetics of anelastic and dielectric relaxation due to reacting point defects, Journal of Physics and Chemistry of Solids, **31**(1970) 1819-1826.

217. T. Degen, M. Sadki, E. Bron, U. König, and G. Nénert. The HighScore suite, Powder Diffraction, **29**(2014) S13-S18.

218. D. Baither, M. Bartsch, B. Baufeld, A. Tikhonovsky, A. Foitzik, M. Ruhle, and U. Messerschmidt. Ferroelastic and Plastic deformation of t'-Zirconia Single Crystals, Journal of the American Ceramic Society, **84**(2001) 1755-1762.